DEVELOPMENT OF A NANOPORE-BASED BIOSENSOR EMBEDDED INTO A MICROFLUIDIC CHANNEL

by

Fatma Doğan

A thesis submitted in partial fulfilment of the requirement for the degree of

Doctor of Philosophy

November 2013

Department of Chemistry

Imperial College of Science, Technology and Medicine

The copyright of this thesis rests with the author and is made available under a Creative Commons Attribution Non-Commercial No Derivatives licence. Researchers are free to copy, distribute or transmit the thesis on the condition that they attribute it, that they do not use it for commercial purposes and that they do not alter, transform or build upon it. For any reuse or redistribution, researchers must make clear to others the licence terms of this work.

Declaration of originality:

I declare that the work presented here is original except where specific reference is made to the work of others, and has not been previously published either wholly or in part to satisfy any degree requirement at this or any other university.

Abstract

Single molecule sensing using solid-state nanopores has sparked tremendous interest within the last decade, whether it be electrical or optical detection of biomolecules, their complexes or binding kinetics. Therefore, the main focus of this thesis was on developing a nanopore biosensor integrated into a microfluidic channel for in-flow electrochemical detection of DNA at single molecule level. By constituting such a compact planar device, nanopores can potentially be turned into future lab-on-chip biosensors with a capability of in-flow single molecule detection.

Two different types of nanopore materials were initially fabricated; a novel ultra thin PI membrane and SiN, and characterized in terms of nanopore conductance and electric noise. An alternative approach to locally and gradually thin SiN nanopores using Reactive Ion Etch technique was also presented with detailed fabrication, optimization and characterization steps. DNA translocation using polymer and thinned SiN nanopores was shown at the end of each fabrication chapter.

On account of their compatibility with microfluidic integration, SiN nanopore chip was compacted into a PDMS microfluidic channel for the purpose of creating potential single molecule detection capabilities under continuous flow conditions. The introduction of flow to the nanopore system is important, because it would ideally bring the benefit of simultaneous electrochemical detection of biological entities in flow, where the idea of lab-on-chip biosensing devices is built upon. To characterize the rheological properties of DNA and flow characteristics, optical experiments were carried out using Confocal Microscopy and Fluorescence Correlation Spectroscopy. The effect of flow rate on the basics of nanopore detection (e.g. nanopore conductance and noise) was discussed, and investigated experimentally. Last, DNA translocation in the absence and the presence of flow was studied as a proof-of-principle. The investigation of detection capability of the integrated device using the chosen flow rates sets the basics for the future applications of nanopore-integrated microfluidic systems (e.g. on-nanopore chip capillary electrophoresis).

Acknowledgments

In the Name of Allah, the Beneficent, the Merciful ‘Who teacheth by the pen, teacheth man that which he knew not’. All praise be to Allah, Lord of the Worlds.

I would like to thank my supervisors Dr. Tim Albrecht and Dr. Joshua B. Edel for introducing me to the nanopore research, their encouragement, patience, and all the advice which they have provided me throughout my PhD. I will always remember their enthusiasm, inspiration, immense knowledge, and vision in science. It has been a great privilege to work with you.

I thank Turkish Ministry of Education for the financial support. I also thank Dr. Suguo Huo from London Centre for Nanotechnology for teaching me how to use FIB, Dr. Alexandar Ivanov for helping me with several FIB studies on the polymer membrane and his valuable comments, Dr. Kostis Michelakis and Tony Corless for helping us with RIE experiments at the University of Surrey. I also wish to thank William Pitchford for his dedication to membrane thinning project, help with the experiments, and genuine friendship; Dr. Agnieszka Rutkowska for her help with some of the AFM studies and Thomas Gibbs for several KOH etch experiments. I am indebted to many people who contributed to the proof-reading of my thesis. I would also like to thank other nanopore-group members for their friendship and the times we shared in the lab/office; Azadeh Bahrami and Philippa Nuttall, and all the other group members.

I have spent such an enjoyable time at Imperial for almost five years, and I believe that there are many people who contributed to that; many thanks to all the students in ISOC -such an amazing energy- mashAllah! I wish I could take you all with me to Turkey. Special thanks to all my friends whom I have met here and back in Turkey.

Lastly, and most importantly, I would like to thank my father and my mother for their love, understanding, believing in me, and continuous duas. A heartfelt ‘thanks’ to all my family members (Ilayda, this is for you!) for their endless support. To them I dedicate this thesis.

Table of Contents

Abstract.....iii

Acknowledgements.....iv

Table of Contents.....v

List of Figures.....ix

List of Tables.....xiv

Symbols and Abbreviations.....xv

CHAPTER 1 Introduction 1

1.1 Introduction 2

1.2 Nanopores as biosensors.....5

1.2.1 Background.....5

1.2.2 The fundamentals of nanopore translocation.....7

1.2.3 Basics of nanopore analytics 7

1.2.4 Nanopore capture phenomena 8

1.2.5 Nanopore detection concept.....11

1.3 Different types of nanopores 14

1.3.1 Biological nanopores 14

1.3.2 Solid-state nanopores.....15

1.4 Different applications of nanopores.....18

1.5 Nanopore integrated microfluidic systems 20

1.6 Motivation 22

1.7 Outline of the thesis 24

CHAPTER 2 Fabrication and Characterization 37

2.1 Nanopore fabrication 38

2.1.1 Nanopore fabrication techniques 38

2.1.2 Nanopore fabrication using Focused Ion Beam 40

2.1.3 Experimental procedure for nanopore fabrication 41

2.2 The choice of the membrane 42

2.2.1 Polyimide nanopores 42

2.2.2 Silicon nitride nanopores 47

2.3 Electrochemical characterization 50

2.3.1 Experimentation 50

2.3.2 Electrochemical characterization 55

2.3.3 Noise performance of the nanopore devices 57

2.3.4 Translocation of λ-DNA through PI nanopores 59

2.4 Conclusion 60

CHAPTER 3 Fabrication of Ultra Thin Nanopore Membranes 66

3.1 Fabrication strategy 68

3.2 Fabrication of locally thinned membranes 70

3.2.1 Design considerations 70

3.2.2 Device fabrication 72

3.3 Etch characterization 74

3.3.1 Determining the etching rate 74

3.3.2 Gradual etch of SiN 76

3.4 Nanopore fabrication 81

3.5 Electrochemical characterization 84

3.6 Translocation of λ-DNA using locally thinned SiN nanopores 85

3.7 Conclusion 87

CHAPTER 4 Integration of Nanopores into Microfluidic Channels 90

4.1 Fabrication of microfluidic chips 92

4.1.1 Design considerations 92

4.1.2 Device fabrication 93

4.2 Integration 95

4.3 Cell setup of the integrated nanopore chip 97

4.4 Apparatus setup 98

4.5 Conclusion 99

CHAPTER 5 Optical Investigation of DNA Behaviour in Flow 101

5.1 Principles of fluorescent imaging 102

5.1.1 Phenomena of Fluorescence 102

5.1.2 Fluorescence Microscopy 103

5.1.3 Components of a fluorescence microscope 104

5.2 Physical qualities of DNA 107

5.3 Experimental set-up 109

5.3.1 Instrumentation 109

5.3.2 Device preparation 109

5.3.3 DNA labelling with YOYO 110

5.4 Velocity measurements of flow-induced molecule migration 110

5.4.1 Velocity measurements by wide-field imaging 111

5.4.2 Velocity measurements by fluorescence correlation spectroscopy 112

5.4.3 Time trace analysis 115

5.5 Investigation of DNA behaviour under flow 123

5.6 Conclusion 127

CHAPTER 6 Electrochemical Detection of DNA in Flow 132

6.1 Electrochemical characterization 137

6.1.1 Investigating the effect of hydrodynamic flow on the nanopore conductance 137

6.1.2 Investigating the effect of hydrodynamic flow on the nanopore noise 140

6.2 Electrochemical detection of DNA translocation 140

6.2.1 Translocation of λ-DNA in the absence of flow 140

6.2.2 Translocation of λ-DNA in the presence of flow 145

6.3 Conclusion 148

CHAPTER 7 Conclusion and Future Directions 151

7.1 Conclusion 152

7.2 Future directions 154

7.3 Summary 156

Appendix 157

List of Figures

CHAPTER 1 Introduction

Figure 1.1 Examples of microfluidic based biosensors. 3

Figure 1.2 Schematic of a DNA stretching experiment across a nanochannel/microchannel interface. 4

Figure 1.3 Schematic of the study of single ion channels in cells carried out by Neher and Sakmann in 1976 (29). 6

Figure 1.4 (A) Schematic of the single molecule detection through a pore with nanometre dimensions and (B) Sketch of a typical current modulation over time. 7

Figure 1.5 (A). Schematic of DNA capture at the nanopore entrance upon the application of certain potential, modified from (32). (B). Simulated electric potential map of the trans side of a 10 nm nanopore during translocation at a potential of 1 V (33). 9

Figure 1.6 Illustrative example of the current trace showing individual DNA translocation events recorded over time. 13

Figure 1.7 α-hemolysin pore. 15

Figure 1.8 Several examples of solid-state nanopores. 17

Figure 1.9 Different applications of solid-state nanopores. 19

Figure 1.10 Several examples of nanopore arrays and nanopore integrated microfluidic biosensing devices. 21

Figure 1.11 Schematic of the single nanopore integrated microfluidic chip. 23

CHAPTER 2 Fabrication and Characterization

Figure 2.1 Schematic of nanopore fabrication using a focused electron or ion beam. 39

Figure 2.2 Picture of the specimen vacuum chamber of the CrossBeam® FIB/SEM system (Carl Zeiss XB1540). 41

Figure 2.3 Pictures of the capsule and its components (liquid dish and sealing stub). 43

Figure 2.4 Schematic of the membrane structure and an optical image. 44

Figure 2.5 SEM images of the membrane and an individual nanopore. 45

Figure 2.6 SEM images of individual pore openings. 46

Figure 2.7 Snapshot of the chip design. 47

Figure 2.8 Workflow of the membrane 48

Figure 2.9 SEM image of a free-standing SiN windows. 50

Figure 2.10 Sketch of commonly used nanopore cell assembly. 51

Figure 2.11 Schematic of the PI nanopore cell set-up. 52

Figure 2.12 Sequential order of the data recording. 53

Figure 2.13 Example of a current trace that the background threshold is determined by fitting the experimental data to the Poisson distribution. 54

Figure 2.14 Cyclic voltammograms recorded using PI membranes. 56

Figure 2.15 Dominant noise sources in PSD, modified from (32). 57

Figure 2.16 Power spectral densities of PI nanopore and SiN nanopore (red and blue, respectively) 59

Figure 2.17 Translocation events of λ-DNA through 17 nm PI nanopore. 60

CHAPTER 3 Fabrication of Ultra Thin Nanopore Membranes

Figure 3.1 Left: Scheme of the DNA translocation through locally thinned membranes, Right: Bright-field Scanning Transmission Electron Microscopy image of the membrane (dark gray; the membrane, light gray; the locally thinned region). 67

Figure 3.2 Schematic of the RIE process inside the vacuum chamber. 69

Figure 3.3 Sketch of the final shape of the locally thinned nanopore devices. 70

Figure 3.4 Snapshots of the marker designs. The scale bar is 95 μm. 71

Figure 3.5 Schematic of the fabrication workflow. 73

Figure 3.6 Dektak surface profiling results of the etch. 75

Figure 3.7 Etch results of the third generation thinned nanopore devices. 78

Figure 3.8 AFM characterization of the third generation thinned nanopore device. 79

Figure 3.9 Etch results of the fourth generation thinned nanopore devices. 80

Figure 3.10 AFM characterization of the fourth generation thinned nanopore devices. 81

Figure 3.11 SEM image of the fourth generation locally thinned free-standing SiN windows.... 82

Figure 3.12 SEM image of the thinned region on a fourth generation locally thinned membrane. 83

Figure 3.13 Cyclic voltammograms obtained using unprocessed and processed SiN chips. 84

Figure 3.14 Examples of 10 second current-time traces recorded at 250 mV. 85

Figure 3.15 t_d and ΔI histograms for λ-DNA translocation events through nanopore devices with different nanopore thickness. 86

CHAPTER 4 Integration of Nanopores into Microfluidic Channels

Figure 4.1 Snapshots of the proposed design of the PDMS and integrated chip (left and right images, respectively). 93

Figure 4.2 Fabrication workflow of the PDMS chip. 94

Figure 4.3 Far left: Schematic of the integrated chip. Left image in the middle: Photograph of the chip. Right image in the middle: Optical image of the microfluidic channel aligned to the free-standing SiN window. Far right: Example SEM image of a nanopore. 96

Figure 4.4 Schematic of the cell assembly and electrochemical set-up. 97

Figure 4.5 Photography image of the apparatus setup. 98

CHAPTER 5 Optical Investigation of DNA Behaviour in Flow

Figure 5.1 Schematic of a Jablonski diagram. 102

Figure 5.2 Basic components of Confocal Fluorescence Microscope; light source, filters, mirrors, objectives and a detector. 103

Figure 5.3 An example of normalized absorption and emission of spectra for a dye, fluorescein isothiocyanate, (FITC) and transmission spectra of excitation and emission filters (4). 105

Figure 5.4 Double helix structure of DNA (14). 107

Figure 5.5 Relaxed DNA, coiled up in solution. 108

Figure 5.6 Velocities obtained using wide-field FM imaging. 112

Figure 5.7 Diagram of the possible temporal changes of the process that affect the single molecule autocorrelation data. 113

Figure 5.8 Representative single-molecule fluorescence burst scans of 155 pM DNA-YOYO complex in 10 mM KCl. 116

Figure 5.9 Representative single-molecule fluorescence burst scans of 15.5 pM DNA-YOYO complex in 10 mM KCl. 117

Figure 5.10 Representative single-molecule fluorescence burst scans of 15.5 pM DNA-YOYO complex in 1 M KCl.. 118

Figure 5.11 Autocorrelation curves of 15.5 pM sample solution for different flow rates. 119

Figure 5.12 Autocorrelation curve and the fit for 0 μl/min flow rate (blue and red, respectively). 120

Figure 5.13 Autocorrelation curves of 15.5 pM sample solution for selected flow rates. 121

Figure 5.14 Flow rate versus τ. a. τ_{flow} versus flow rate. b. $\tau_{Diffusion}/\tau_{flow}$ versus flow rate. 122

Figure 5.15 Flow rate versus flow velocity. 122

Figure 5.16 Shear rate and Wi versus flow rate varying between 0.02 μl/min and 2 μl/min (a and b, respectively)..... 125

Figure 5.17 Fluorescence images of single λ-DNA molecules at different flow rates.. 126

Figure 5.18 Mean fractional extension versus flow rate and Wi for 2 different DNA concentration (e.g. 15.5 pM and 155 pM DNA)..... 127

CHAPTER 6 Electrochemical Detection of DNA in Flow

Figure 6.1 Schematic of the DNA capture through a nanopore embedded into a microfluidic channel in flow. 133

Figure 6.2 Flow velocity profile in a 75 μm x 75 μm x 6 mm microchannel, simulated using COMSOL Multiphysics®..... 136

Figure 6.3 Electrochemical characterization of the integrated chip..... 138

Figure 6.4 RMS noise plotted against different flow rates. 140

Figure 6.5 Examples of current-time traces at different voltages. 141

Figure 6.6 Top: Scatter plot of current blockades versus dwell time.. 142

Figure 6.7 Representative individual translocation events at 200 mV. 144

Figure 6.8 Example of 1.5 second current-time traces recorded at 250 mV at a flow rate of 2 µl/min. 145

Figure 6.9 a. Flow rate versus translocation frequency. b. Flow rate versus translocation statistics (i.e. td and ΔI). 146

Figure 6.10 a. Flow rate versus translocation frequency (Different colours represent the repeats). b. Flow rate versus translocation statistics (i.e. t_d and ΔI) 147

Appendix

Figure A Translocation of 5 kbp dsDNA. Translocation frequency is plotted against the flow rates..... 157

List of Tables

Table 3.1 Experimental readings of RF power and bias for the fabrication of the fourth generation thinned nanopore devices..... 79

Table 3.2 Summary of λ-DNA translocation events shown in Figure 3.15. 87

Table 6.1 G_{exp} and d_{exp}, extracted from the IV curves illustrated in Figure 6.3b. 139

Table 6.2 Summary of λ-DNA translocation events shown in Figure 6.6. 143

Symbols and Abbreviations

R_{access}	Access resistance
Al_2O_3	Aluminium oxide
A	Amplifier
$\delta I(t)$	Amplitude of current fluctuations
A/D	Analog-to-digital convertor
ARDE	Aspect ratio dependant etch
AFM	Atomic force microscope
$G(\tau)$	Autocorrelation function
APD	Avalanche photodiode
τ_{diff}	Average diffusion time
τ_{flow}	Average flow time
V_L	Average linear velocity
BioMEMS	Biological microelectromechanical systems
G_b	Blocked pore conductance
I_b	Blocked pore current
CE	Capillary electrophoresis
CCD	Charged coupled device
C	Coulomb
G	Conductance
κ	Conductivity
CD	Critical dimension

A_{DNA}	Cross-section of DNA
A_c	Cross-sectional area of the channel
I	Current
DNA	Deoxyribonucleic acid
Z	Depth of field
d	Diameter
d_{pore}	Diameter of the nanopore
D	Diffusion coefficient
t_{diff}	Diffusion time
V_{diff}	Diffusional speed
a	Distance between each nucleotide
C_{DNA}	DNA concentration
L_c	DNA contour length
L_p	DNA persistence length
ds	Double strand
t_d	Dwell time
E	Electric field
EDL	Electrical double layer
EBL	Electron beam lithography
μ_{ep}	Electrophoretic mobility
EMCCD	Electron multiplying charged coupled device
F	Farad
V_{ep}	Electrophoretic speed

e	Elementary charge
EDTA	Ethylenediaminetetraacetic acid
FESEM	Field emission scanning electron microscopy
V_{flow}	Flow velocity
FCS	Fluorescence correlation spectroscopy
FM	Fluorescence microscope
FIB	Focused ion beam
f	Frequency
h_c	Height of the microfluidic channel
HDMS	Hexamethyldisilazane
HPLC	High performance liquid chromatography
IR	Infrared
IPA	Isopropyl alcohol
kbp	Kilo base-pair
kHz	Kilohertz
λ-DNA	Lambda DNA, 48.5 kbp
w_0	Laser beam waist
L_c	Length of the microfluidic channel
L_{pore}	Length of the nanopore
LPCVD	Low pressure chemical vapor deposition
MFE	Mean fractional extension
μ-TAS	Micro-total analysis systems
n	Number of ions

NA	Numerical aperture
G_o	Open pore conductance
I_o	Open pore current
PIV	Particle image velocimetry
PD	Photodiode
PMT	Photomultiplier
PCH	Photon counting histograms
POC	Point of care
PPP-NCHR	Point probe plus non-contact high resonance frequency
ΔV	Potential drop
PDMS	Poly(dimethysiloxane)
PMMA	Poly(methyl methacrylate)
PC	Polycarbonate
PEEK	Polyether ether ketone
PET	Polyethylene terephthalate
PI	Polyimide
PCR	Polymerase chain reaction
PTFE	Polytetrafluoroethylene
R_{pore}	Pore resistance
KCl	Potassium chloride
KOH	Potassium hydroxide
PSD	Power spectral density
z_0	Probe depth

QE	Quantum efficiency
r*	Radial distance
RF	Radio frequency
RIE	Reactive ion etch
n	Refractive index
ξ	Relaxation time
R	Resolution
RNA	Ribonucleic acid
RMS	Root-mean-square
SEM	Scanning electron microscope
$\dot{\gamma}$	Shear rate
SNR	Signal-to-noise ratio
SiO_2	Silicon dioxide
SiN	Silicon nitride
SMD	Single molecule detection
ss	Single strand
SCCM	Standard cubic centimeters per minute
V_g	Structure factor
SF_6	Sulfur hexafluoride
σ	Surface charge density
γ	Surface tension
SERRS	Surface-enhanced resonance Raman spectroscopy
T	Temperature

CF_4	Tetrafluoromethane
L	Thickness
τ	Time delay
δt	Time interval between two events
R_{total}	Total cell resistance
TIRF	Total internal reflection spectroscopy
L_{DNA}	Total length of DNA
TEM	Transmission electron microscope
Tris.HCl	Tris(hydroxymethyl)aminomethane hydrochloride
UV	Ultra violet
V	Voltage
Q	Volumetric flow rate
λ	Wavelength
Wi	Weissenberg number
w_c	Width of the microfluidic channel
α-HL	α-hemolysin
YOYO-1	1,1'-(4,4,7,7-tetramethyl-4,7-diazaundecamethylene)-bis-4-[3-methyl-2,3-dihydro-(benzo-1,3-oxazole)-2-methylidene]-quinolinium tetraiodide

CHAPTER 1 Introduction

Nanopores as an emerging class of biosensors are presented in this chapter. The principles of nanopore detection, concept and the applications of nanopores are also discussed. The chapter ends with the motivation behind the project and an outline of the thesis.

1.1 Introduction

A biosensor is a compact analytical device combined with a signal conversion unit that transforms analytical information of biochemical mechanisms into a chemical or physical output **(1)**. The idea of developing biosensors was first conceptualized by Leland C. Clark in 1962 at a symposium in which he pointed out '*how to make electrochemical sensors (pH, polarographic, potentiometric or conductometric) more intelligent*' **(2)**, and shown later in a study in which he measured oxygen in blood by an oxygen electrode **(3)**. Although the field has seen many different applications since then, the key developments in biosensing have been the miniaturization and integration into small compartments that can perform multiple tasks (i.e. biological assays, sample purification, mixing, processing and characterization) with high throughput and less sample consumption at low cost and shorter time. One such monolithic biosensing device (Biological Microelectromechanical Systems, BioMEMS, or Lab-on-a-chip/μ-Total Analysis Systems, μ-TAS[1] **(4)**) offers an elegant and simple way of extracting detailed information about the analyte in the field of genomics, proteomics or metabolomics.

The interest in miniaturized biosensors has continued to increase as the performance of BioMEMS and μ-TAS (couple of mm in size or even in micron scale[2]) has became increasingly powerful. The power of such systems stems from the capability to downsize any analytical components such as electrodes, optical detectors, pumps, valves. To date, the realization of combining a network of microfluidic channels into MEMS and μ-TAS technology, which has started in the 1990's, has driven the development of numerous chip-based intelligent designs of biosensors. Microfluidic systems bring the advantage of using small fluid compartments, and thus the ability to process minute amounts of sample, safety and ease in handling of biological samples between different processes. They are also ideal platforms for building up portable devices that can be used in on-the-field applications. For example, commercially available glucometers are based on paper-based microfluidic channels, illustrated in the right image of

[1] The term 'lab-on-a-chip' is regarded as synonymous to 'μ-TAS'.
[2] The size can be larger than mm in particular applications.

Figure 1.1, and use 50 µl of blood to measure blood glucose levels **(5)**. The chip also offers ease of handling.

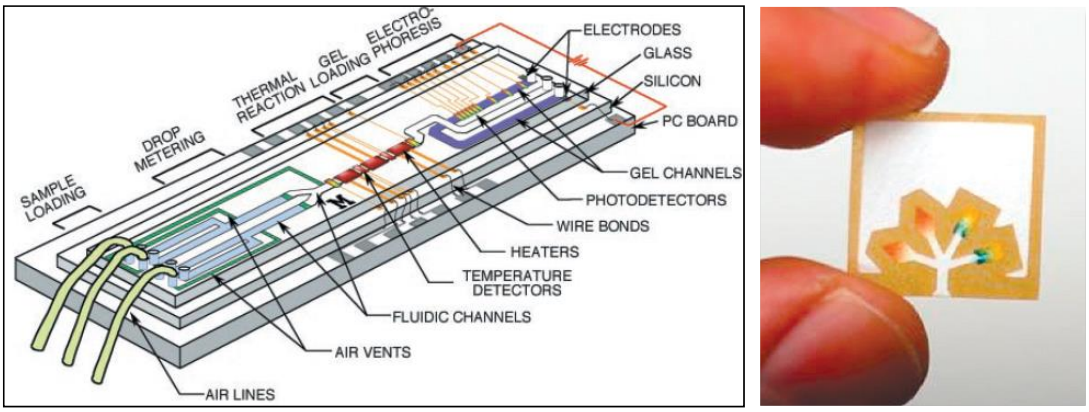

Figure 1.1 Examples of microfluidic based biosensors. Left: Schematic of a device with integrated sample preparation, PCR and gel electrophoresis (6). Right: Photograph of a commercially available paper-based microfluidic biosensor; a glucometer (5).

There are many other examples that have succeeded in combining multiple functionalities (e.g. injection, mixing, heating/cooling, chemical processing, amplification, separation, detection) in a single chip **(7)**. Capillary electrophoresis on a chip, '*on-chip CE'*, is arguably one of the foremost applications. Jacobson *et al* were the first to introduce the concept of an integrated CE on chip with different functions that enabled mixing, enzymatic reactions, and separation **(8)**. Another well-known example is the implementation of the polymerase chain reaction on a chip, '*on-chip PCR*', which copies and amplifies certain sequence of a DNA strand by several cycles of heating and cooling so that the analysis efficiency is enhanced by amplification. Further improvements in chip fabrication include the involvement of cell isolation, subsequently followed by PCR, and CE for the separation **(6)**. On protein sensing, capillary electrochromatography (CEC) or high-performance liquid chromatography (HPLC) coupled with a mass spectrometer have been developed **(9)**. Immunoassays, flow cytometry, tissue engineering, and cell trapping are other applications that have been integrated into microfluidic systems.

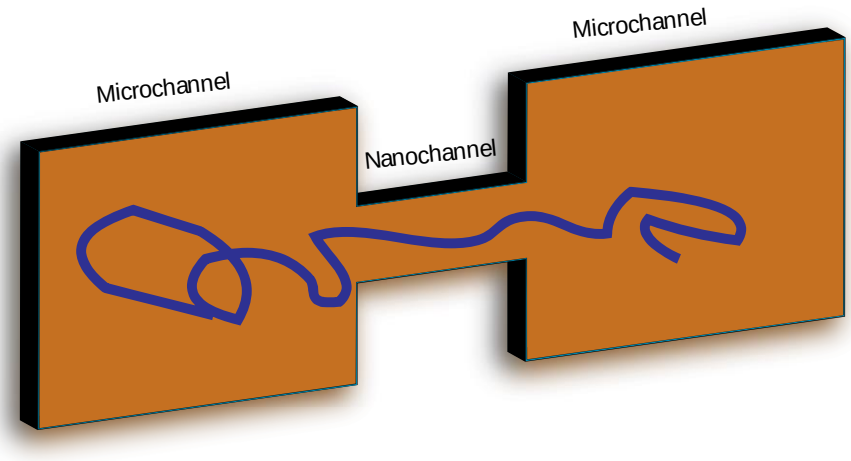

Figure 1.2 Schematic of a DNA stretching experiment across a nanochannel/microchannel interface.

Using a different approach, the capability of integrated microfluidic systems can be enhanced to the single molecule level '*single molecule detection* (SMD)', by constituting a single nanofluidic channel, nanofluidic channel arrays, nanoslits or a nanopore in between two microfluidic channels[3]. Nanofluidic systems are composed of approximately 100 nm structures, or even smaller, in comparison with micron scale dimensions of microchannels (typically in the range of 1–500 μm). The use of nanofluidic systems can facilitate the study of individual molecules at molecular-length scales, the physical phenomena and forces in biological mechanisms in confinement[4], which would otherwise not be observable using microchannels **(10)**. For example, nanofluidics/microfluidics interfaces would provide sorting, trapping and stretching single DNA molecules at dimensions smaller than its gyration radius[5] as sketched in Figure 1.2. In general, the utility of these systems can be extended to sample preparation, injection, transport, mixing, gel-free molecular separation, and detection. For example, Han *et al* have shown the entropic trapping of long DNA molecules in nano/microfabricated structures **(11)**. Similarly, the design of a nanofilter array consisting of alternating nano and microstructures has been reported by Fu *et al* **(12)**. DNA tracking **(13)** and the denaturation mapping of DNA **(14)** have also been achieved in more sophisticated ways. Interestingly, most of these techniques

[3] Integrating them into microfluidic channels reduces the entropic cost of fluid flow in constrained geometries.
[4] Examples include ion permselectivity, double-layer overlap, increase in diffusive forces and localized electric field.
[5] DNA in confined spaces is studied in detail in CHAPTER 5.

are based on fluorescence detection, which requires labelling of the molecule and is diffraction-limited. Some of the fluorescence detection techniques also requires high-tech instrumentation and therefore limits the detection to laboratory benches. A practical solution to this can be to utilize nanofluidic channels as an electrochemical sensing tool **(15-17)**.

Microfluidic systems with integrated nanopores are notably one of the best examples of label-free, single molecule electrochemical sensors. Such systems are still at an early stage of research and development. Perhaps the reason for the slow progress is the ongoing process to establish a prospect of well-defined nanopore detection concept. To date, nanopores as biosensors have proven to be capable of identifying many different biomolecules at the single molecule level and of studying the dynamics of biological processes such as binding kinetics. If embedded into microfluidic systems, nanopores would provide tremendous advantages for miniaturized biosensing technology; some of the advantages include label-free SMD capability, time- and cost- efficiency. The integration would also enable in-flow electrochemical detection at single molecule level. It is, therefore, not farfetched to imagine that life science applications of nanopore sensors outside the laboratory will soon be realized.

In summary, in the last half century, the field of integrated microfluidic systems has seen many improvements with respect to design, fabrication, method, materials and concept. Interested readers are referred to related review articles **(9, 18-20)**. However as for the scope of this thesis, we will concentrate on nanopores and nanopore integrated microfluidic systems that have been demonstrated as a potential candidate in the field.

1.2 Nanopores as biosensors

1.2.1 Background

The birth of nanopore research dates back to an idea proposed by A. Moldovan in 1934 **(21)**, however, it was Wallace H. Coulter who made it a reality in the late 1940's with the invention of an automated cell counting and sizing apparatus, the Coulter counter. Patented in 1953 **(22)**,

blood cells were counted and sized when they were coaxed in the lumen of a micron size orifice by an electric field. Applications of the Coulter counter for sub-micrometer measurements (i.e. down to 0.2 μm) were achieved several years later **(23)**, followed by its further modification enabling the measurements of almost 0.09 μm sized particles in 1970's **(24)**. Although many researchers have contributed to the expansion of the field in many different ways **(25-28)**, it was Neher and Sakmann who developed a more sophisticated method based on the same principle; an electrophysiological technique called '*Patch clamping*[6]' winning them a Nobel Prize in 1991.

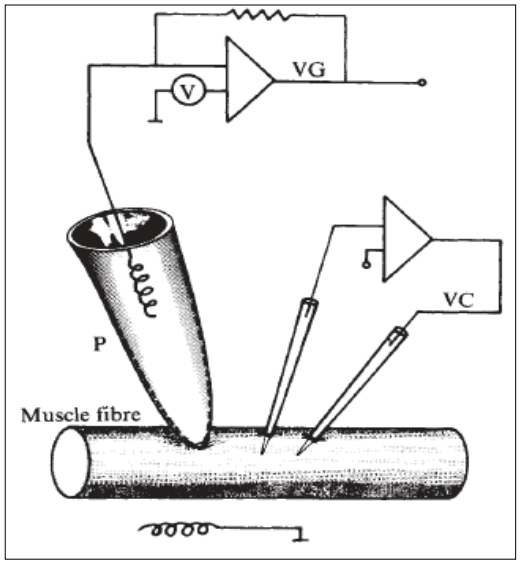

Figure 1.3 Schematic of the study of single ion channels in cells carried out by Neher and Sakmann in 1976 (29).

Patch clamping technique allowed them to study and manipulate the ionic movement in biological cell membranes connected to an electronic circuit by a glass micropipette tip **(29)**. Recently, inspired by the basic principles of the Coulter counter, Bezrukov *et al* have reported the translocation of polyethylene glycol through a channel-forming peptide inserted into a lipid bilayer (channel opening was in the order of several nanometers) **(30)**. Although the first attempt to thread DNA through bio-nanopores was carried out independently by David Deamer and George Church in the early 90's, successful translocation was not achieved until 1996. This work was reported by Kasianowicz *et al* in a landmark study **(31)** showing the study and manipulation

[6]It is also widely known as '*single channel recording*'.

of single biomolecules, as such the idea of single molecule sensing and most importantly sequencing becomes feasible in a very simplistic manner.

1.2.2 The fundamentals of nanopore translocation

This section explores the basics of nanopore detection, the physics of DNA capture by the nanopores and the key physical parameters that are used in the characterization of nanopores and the output electrochemical signal. Types of nanopores and their applications will be discussed in the following sections.

1.2.3 Basics of nanopore analytics

Nanopores are conceptually the newest members of the Coulter counter family with a nano-scale pore size as opposed to a micron scale hole, as in early generations of the Coulter counter. A nanopore is either formed biologically on a lipid bilayer or engineered on an insulating

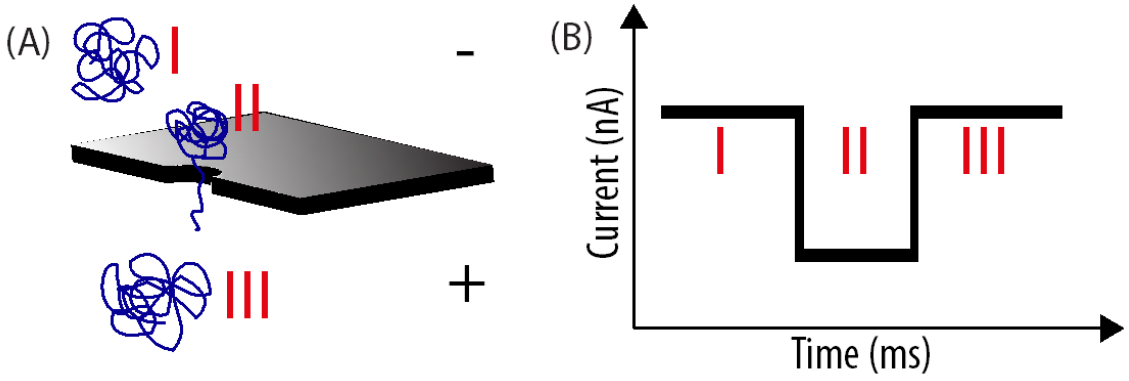

Figure 1.4 (A) Schematic of the single molecule detection through a pore with nanometre dimensions and (B) Sketch of a typical current modulation over time. (I) Free DNA in cis chamber before translocation where the open pore current shows a stable current value. (II) Current is blocked during the translocation, thus resulting in a current reduction. (III) After the translocation, DNA enters the trans chamber and current returns to original level.

nanoscale material using semiconductor technology. The layer that the nanopore is constituted on is called '*membrane*' in either case. The membrane separates two chambers in an ionic solution[7] and the pore provides an ionic pathway between each chamber. In general, the chambers are

[7] In case there is no pore, membrane provides gigaohm sealing.

named as '*cis*' and '*trans*'[8]. The chambers are connected to a patch clamp amplifier via two electrodes. Application of a particular voltage (e.g. 50-250 mV) generates an electric field across the nanopore and a constant current through the pore is recorded over time. The magnitude of the electric field is typically on the order of 10^6 V/cm whereas the ionic current is around 1–100 nA. The values vary depending on the membrane thickness, nanopore diameter, salt concentration and the voltage applied.

The simplest nanopore theory '*excluded volume theory'* describes that when any molecule larger than the electrolyte ions in size is introduced to the one of the chambers; the molecule is forced to transverse to the other chamber through the pore by excluding electrolyte ions from the pore. The consequence of this passage is the temporal partial blockage of the ionic current. These discrete current modulations can be correlated to the size, charge and conformation of the molecules translocating while the frequency of the events refers to the number of molecules. In spite of its simple concept, nanopore detection process is rather complex when investigated exclusively on the molecular level. The following sub-sections are therefore dedicated to elaborate on the principles of the detection concept based on DNA translocation.

1.2.4 Nanopore capture phenomena

Capture of the molecule (e.g. DNA) by the nanopore is governed by two physical regimes; *diffusion-limited regime* where the molecule is far away from the pore mouth ($r^* < r$[9]), and *energy barrier-limited regime* at a distance of $r^* \sim r$ **(32)**. Representative image of the capture can be found in Figure 1.5A. In the diffusion-limited regime, the molecule diffuses randomly in the solution owing to the Brownian motion and its capture is limited by the time that the molecule travels to the pore mouth. When the molecule approaches to the pore, the effect of the electric field becomes more dominant compared to the diffusive forces, where the molecule entry to the pore is limited by an activation energy created by the electric field. Referring to an energy-barrier

[8] In our experiments, cis is the negatively biased chamber and trans is the opposite.
[9] The radial distance between the pore entrance and the position of the molecule in the cis chamber is represented by 'r'.

limited regime, molecule no longer freely diffuses in this regime, rather is driven towards the nanopore by a space dependant drift velocity;

$$v(h) = \mu_{ep} \nabla V(r)$$ Equation 1.1

where μ_{ep} is the electrophoretic mobility of molecule, and V(r) is the potential at a distance of r from the pore, represented by Equation 1.2;

$$V(r) = \left(\frac{d_{pore}^2}{8 L_{pore} r}\right) \Delta V$$ Equation 1.2

where ΔV is the potential drop across the pore, d_{pore} is the nanopore diameter, and L_{pore} is the nanopore thickness. V(r) defines the electric field profile in the system and is highly dependent on the nanopore geometry.

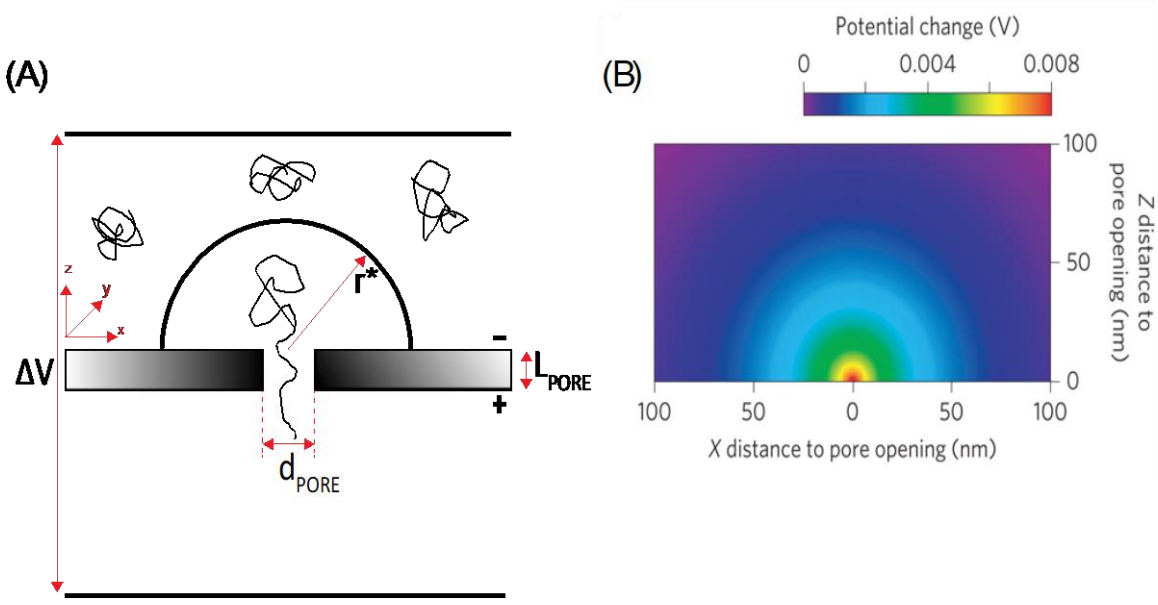

Figure 1.5 (A). Schematic of DNA capture at the nanopore entrance upon the application of certain potential, modified from (32). (B). Simulated electric potential map of the trans side of a 10 nm nanopore during translocation at a potential of 1 V (33).

Clearly, at close distance to the pore mouth (r*~r), the electric field is relatively stronger (an example of the electric potential map on the trans side of the nanopore can be seen in Figure 1.5B) and creates an electrophoretic trap for the negatively charged molecule. The electrophoretic

trap is defined by a free energy barrier which includes entropic trapping effects and an enthalpy term covering specific and non-specific DNA-nanopore interactions as well as ions depletion from the pore due to DNA entry **(34, 35)**.

The distance r* can be estimated from the relationship between the electrophoretic speed (V_{ep}) and the diffusional speed of the molecule (V_{diff}) **(32)**. In particular, once the molecule approaches to the pore, where the cross-over between r*<r and r*>r occurs, V_{diff} becomes comparable to V_{ep}. V_{diff} can be approximated from the diffusion time (t_{diff}) required for the molecule to travel from the distance r to the pore entrance;

$$V_{diff} \sim \frac{r}{t_{diff}} \sim \frac{r}{\frac{r^2}{D}} \sim \frac{D}{r} \qquad \text{Equation 1.3}$$

where D is the diffusion coefficient and t_{diff} is expressed by the Brownian motion. V_{ep} is defined by Equation 1.4[10];

$$V_{ep} = -\mu_{ep} E(r) \qquad \text{Equation 1.4}$$

where E(r) is expressed by Equation 1.5 ;

$$E(r) \cong \frac{V(r)}{r} \qquad \text{Equation 1.5}$$

The relationship between V_{diff} and V_{ep}, based on the fact that V_{ep} is more pronounced than V_{diff} at a distance of r*>r, leads to the expression of r* by Equation 1.6;

$$r^* \cong \frac{d_{pore}^2 \mu_{EP}}{8 L_{pore} D} \Delta V \qquad \text{Equation 1.6}$$

where q is the charge of the molecule.

To summarize, without any external force, the necessary energy to overcome the energy barrier would not be reachable, because the deformation of DNA from its relaxed state to a linear form and its capture is not sterically and entropically favourable. The driving force is generated

[10] The minus sign is used to represent the negative charge of DNA.

by the application of voltage, and the creation of an electric field across the pore. As a result, DNA translocation is strongly governed by the voltage applied as well as nanopore dimensions.

1.2.5 Nanopore detection concept

The detection concept includes acquiring a current trace at a certain voltage over time and analysing the current modulations which occur upon the translocation of the molecule. In other words, the addition of DNA leads to the partial blockage of the nanopore, resulting in an detectable modulation in current (I) -or nanopore conductance (G)- as opposed to a stable current trace when DNA is absent from solution. Therefore, the signal can be identified by the blockage amplitude of I or G (ΔI or ΔG, respectively).

G is the reciprocal of the pore resistance and important in determining nanopore activity. The pore resistance is simply expressed by the total cell resistance, if the pore thickness is relatively larger than the pore opening ($L_{pore}>d_{pore}$). However, if the pore is thin ($L_{pore}<d_{pore}$), the so-called '*access resistance*' dominates the total pore resistance, where the electric field lines converging from the bulk electrolyte to the mouth of the pore becomes considerably important **(36)**. This effect yields Equation 1.7 **(37)**;

$$R_{total} = R_{pore} + 2R_{access} \qquad \text{Equation 1.7}$$

where R_{pore} is the pore resistance and R_{access} is the access resistance. R_{pore} is calculated from the relationship between the conductivity of the bulk solution and the geometrical terms of the nanopore;

$$R_{pore} = \frac{4L_{pore}}{\kappa A_{pore}} \qquad \text{Equation 1.8}$$

where A_{pore} is the cross section of the nanopore, L_{pore} is the thickness of the nanopore, and κ is the conductivity;

$$\kappa = \left(\mu_{K^+} + \mu_{Cl^-}\right) n_{KCl} e \qquad \text{Equation 1.9}$$

where μ_{K^+} and μ_{Cl^-} are the electrophoretic mobility of K^+ and Cl^- ions, respectively, n_{KCl} is the number density of counterions, and e is the elementary charge. An explicit expression of R_{access} is derived from the treatment of the resistance at the boundary between the pore entrance and the bulk electrolyte **(38, 39)**, yielding Equation 1.10 **(39)**;

$$R_{access} = \frac{1}{\kappa d_{pore}} \quad \text{Equation 1.10}$$

Hence, the summation of R_{total} and R_{access} yields Equation 1.11 **(36)**;

$$R_{total} = \frac{1}{\kappa}\left(\frac{4L_{pore}}{\pi d_{pore}^2} + \frac{1}{d_{pore}}\right) \quad \text{Equation 1.11}$$

and Equation 1.12 for G;

$$G = \left(\frac{1}{\kappa}\left(\frac{4L_{pore}}{\pi d_{pore}^2} + \frac{1}{d_{pore}}\right)\right)^{-1} \quad \text{Equation 1.12}$$

However, for a full description of G, the surface charge of the pore should also be included; because the surface charge effects becomes non-negligible at the nanometer scale down to 5-10 nm. G can therefore be described thoroughly as the sum of the bulk conductance and surface conductance **(40)**. For a cylindrical pore, G is simply expressed by Equation 1.13;

$$G = \pi \frac{d_{pore}^2}{4L_{pore}}(\mu_{K^+} + \mu_{Cl^-})n_{KCl}e + \pi \frac{d_{pore}}{L_{pore}}\sigma\mu_{KCl} \quad \text{Equation 1.13}$$

where σ is the surface charge density. The first term refers to the bulk conductance and the second term represents the surface conductance[11].

Regarding ΔG and ΔI, these are the means to express the change in the magnitude of the ionic transport caused by the excluded ions due to the presence of DNA. So, they can be expressed as a function of κ and geometry of the nanopore for larger pores and/or under high salt concentration, where the surface contribution is neglected, as shown by Equation 1.14 and Equation 1.15 **(41)**;

[11] However, if the nanopore is conical rather than a cyclindirical shape, the conductance needs to be calculated using a slightly different formula, which also takes into account the opening angle of the pore.

$$\Delta G = (G_o - G_b) \approx \frac{\kappa A_{DNA}}{L_{pore}}$$ Equation 1.14

$$\Delta I = (I_o - I_b) \approx \Delta V \frac{\kappa A_{DNA}}{L_{pore}}$$ Equation 1.15

where G_o and I_o are the open pore conductance and current, respectively, and G_b and I_b are the blocked pore conductance and current, respectively, and A_{DNA} is the cross-section of DNA.

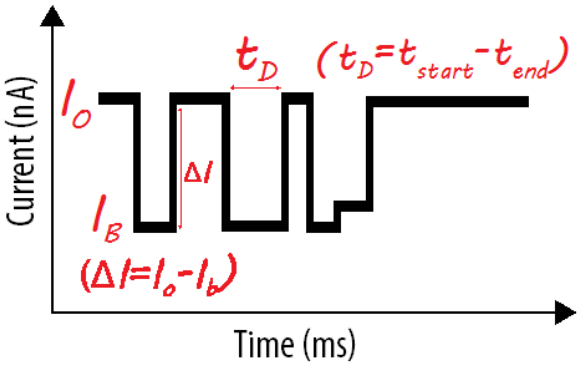

Figure 1.6 Illustrative example of the current trace showing individual DNA translocation events recorded over time. I_o; open pore current, I_b; blocked pore current, ΔI; current blockade amplitude, and t_d; dwell time.

G_b and I_b are the characteristic features corresponding to the depletion of the counter ions from the channel due to DNA presence, and indicate at which conformation the DNA passes through the pore. If the pore is not small enough for only a single linear DNA strand to occupy in, there is a high possibility that either the DNA translocates in a folded position or more than one DNA might be in the pore at the same time. As a result, this will produce a higher value of ΔG and ΔI than expected. Although Equation 1.14 and Equation 1.15 are the simplistic models which do not include the contribution of any electrostatic interactions between the pore wall and the biomolecule or other physical factors, they still represent the key features of the translocating molecule such as conformation as well as charge when coupled with translocation time, t_d.

t_d provides information about the length of the molecule translocating and should scale linearly with respect to the length of DNA in an ideal case scenario, presuming that the DNA with a longer chain stays in the pore longer than that with a shorter chain. Although this

presumption was found to be true for ssDNA translocation through biological pores, t_d does not necessarily follow a linear scaling with DNA length in solid-state nanopores **(42)**. In fact, it was found that t_d obeys a power law of $t_d \sim L^{1.27}$ in large solid-state nanopores, while the scaling factor varies for short and long DNA fragments in small solid-state nanopores **(42-45)**. Non-linear scaling is attributed to several reasons including DNA coil shrinking outside the pore, interactions of DNA with the nanopores and with itself.

In addition, translocation velocity, V_t, another form of expressing t_d, and the time between two successive events, δt are also crucial. t_d, V_t and ΔI are sensitive to the properties of the biomolecule (length, chemical composition, sequence etc.) while δt, is mostly affected by concentration. In general, translocation statistics are dependent variables to temperature, concentration, viscosity, nanopore shape and the voltage applied, which is also proven experimentally.

1.3 Different types of nanopores

1.3.1 Biological nanopores

Biological nanopores incorporated into a lipid bilayer can be formed with atomic precision. For instance, a bacterial protein pore α-hemolysin (α-HL) which is the most common choice for nanopore-based biomolecule sensing, consists of two structural units with a mushroom-shaped scaffold (the dimensions of the protein are 10 x 10 nm) **(46)**. The point at which the two units meet is the constriction site with a diameter of 2.6 nm. Because of this small feature, α-HL only allows the study of single stranded DNA and RNA (ssDNA and ssRNA, respectively), which was demonstrated by Kasianowicz *et al* **(31)**. Another protein pore that has been used in the field is MspA secreted from Mycobacterium smegmatis **(47)**, which has a smaller pore diameter (1.2 nm) and shorter length (0.5 nm). A third option as a biological pore was recently proposed by Wendell *et al* who showed the translocation of double stranded DNA (dsDNA) through a phi29 viral packaging motor **(48)**. Its nanopore entrance is slightly larger than the previously used biopores; 3.6 nm.

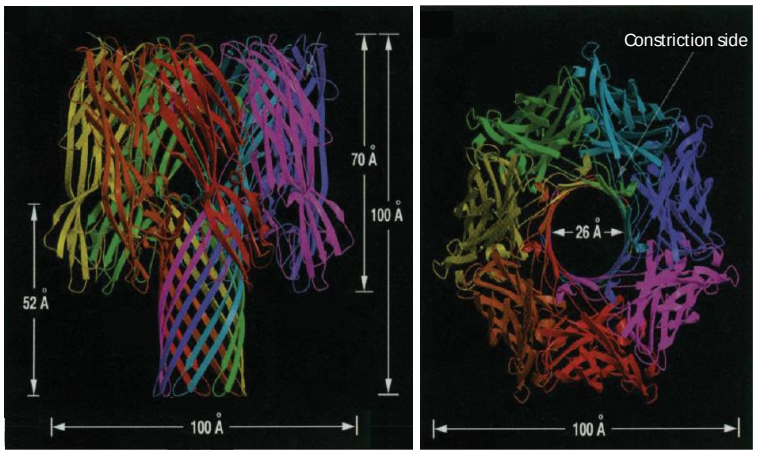

Figure 1.7 α-hemolysin pore. Cis entrance is 4.1 nm, trans entrance (red) is 2.6 nm, length is 10 nm (46).

Proteinaceous pores can be tailored by bioengineering techniques to increase their selectivity and specificity, and offer high reproducibility on account of their fixed geometry. Furthermore, they are potential candidates for next-generation DNA sequencing tools. However, they can only function in a lipid bilayer, which is in fact unstable and tends to rupture **(49)**. Moreover, the life time of a biological membrane (on the order of minutes to hours) is limited due to the lipid membrane's fragility **(49, 50)**. Other drawbacks include the limitations on the study of a range of temperature, pH and salt concentration. Although it is arguable, these drawbacks would eventually limit the integration of the biological pores into other sensing devices for the applications of point-of-care devices.

1.3.2 Solid-state nanopores

With advances in nanotechnology, the Coulter counter could also be replicated on the nano-scale size on an electrically insulating membrane using semiconductor technologies and the state-of-the-art electron and ion beam techniques. Li *et al* were the first to demonstrate the fabrication of a solid-state nanopores by sculpting a single nanopore with a diameter of 60 nm on a 500 nm free-standing silicon nitride (Si_3N_4) membrane using a focused Ar^+ ion beam **(51)**. The pore size was then shrunk to 1.8 nm by further ion beam exposure, where the reduction is monitored in real-time with a feedback mechanism. Soon after, Storm *et al* reported a new approach that is based on high energy electron beam (using a transmission electron microscope, TEM) to fine-

tune the size of a silicon oxide (SiO_2) nanopore, initially processed with electron beam lithography and anisotropic etching to produce 20 nm size nanopores in diameter **(52)**. Since then, manufacturing solid-state nanopores has been of interest to many researchers due to their robustness in extreme conditions (e.g. high temperatures, a wide pH window, and concentration) and the flexibility in controlling the stoichiometry of the pore and manipulating membrane properties. For example, nanopores with angstrom level precision can be fabricated by atomic layer deposition where free standing high dielectric materials such as Al_2O_3 can be produced and used as nanopore membrane material **(53)**.

Other types of engineered nanopores include polymer membranes, glass/quartz capillaries, nanotubes and graphene **(54-56)**. The most commonly used polymer membranes are Polyethylene terephthalate and Polyimide[12]. Briefly, they are etched by feedback controlled track-etching technique based on the employment of highly energetic heavy ions followed by chemical etching **(57, 58)**. In contrast, glass capillaries with nanotip openings are simpler to fabricate; the material is heated up by a simple laser source and the capillary is split apart from the point the laser interacts with the capillary by a precision puller **(59, 60)**. For nanotubes, different ways of integrating a nanotube, synthesised chemically, into a Coulter counter setup have been proposed **(61-64)**. The earliest attempts are based on a multiwall carbon nanotube embedded in an epoxy matrix and subsequently sectioned into smaller pieces by a microtome **(62)**. An alternative is to span a nanotube, either single walled carbon nanotube **(64)** or inorganic nanotubes **(63)**, between two fluid chambers. A semi-conducting graphene-based membrane with atomic scale thickness (just 0.6 nm) is another alternative material, which is in fact the most intriguing one because of its excellent mechanical properties and high electrical conductivity **(65)**. In order to utilize graphene for nanopore sensing, a multilayer graphene sheet (or potentially a single layer sheet) is mounted onto a support layer such as a typical nanopore membrane with a micron scale hole, and a single nanopore can be milled through using conventional ion/electron beam techniques.

[12] Polymer membranes are discussed in more detail in CHAPTER 2.

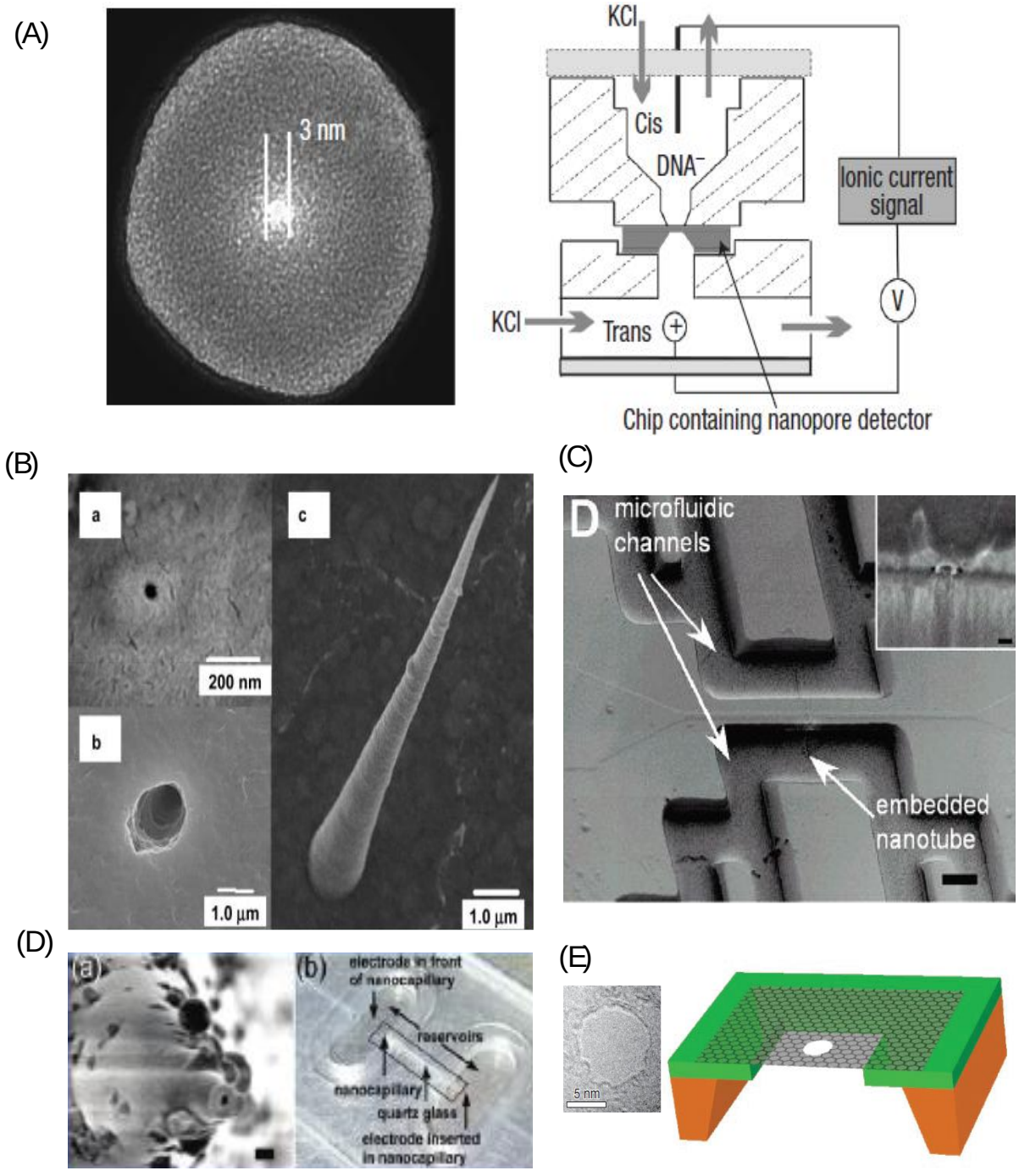

Figure 1.8 Several examples of solid-state nanopores. (A). Left: TEM image of SiN nanopore that was shrunk from an initial pore size of 60 nm pore to 3 nm diameter pore after continuous ion beam exposure. Right: Electrochemical set-up (66). (B). SEM images of a track etched polymeric nanopore (58). (C). SEM image of an inorganic nanotube embedded between two microfluidic channels (63). (D). SEM image of a glass capillary pipette tip positioned between two PDMS made chambers (59). (E). Left: Graphene nanopore drilled by TEM. Right: Cross-section of graphene devices mounted onto a SiN aperture supported on a Si subsrate (54).

The list for the choice of membrane material can be extended to Si, SiN doped with Si, SiC, PMMA, apiezon W wax, TiN, and thermoplastic polyurethane **(67, 68)**.

In addition, the surface and the geometry of solid-state nanopores can be modified either physically or biochemically by several deposition and functionalization techniques in order to enhance the efficiency of the device for higher specificity and selectivity towards the analyte. An overview of the subject can be found in a tutorial review by Miles *et al* **(69)** while comprehensive review articles on stimuli-responsive nanopores **(70)** and biomimetic nanopores **(71)** are also worth reading.

1.4 Different applications of nanopores

A substantial amount of research into proving the capability of solid-state nanopores for biosensing has been put forward within the last decade. These include different applications such as the length differentiation of ssDNA **(72)** and dsDNA, and the discrimination of different nucleic acid polymers **(73)**. Nanopores can also excel at RNA profiling **(74)**, detection of proteins and protein/antibody complexes **(75-78)**, and studying DNA-binding complexes **(79-81)**, DNA-protein complexes **(82, 83)**, RNA-antibiotic complexes **(84)**, protein-protein interactions, virus–antibody interactions **(85)**, epigenetic analysis **(86, 87)**.

Probably one of the most exciting aspects of the nanopore detection is its potential ability to sequence DNA at lower cost than the conventional techniques. The prerequisite of nanopore sequencing is the design and fabrication of novel device architectures with nano scale electrodes positioned at the nanopore entrance; since every single base possesses fingerprint electronic characteristics, one might map out the whole sequence of a genome by measuring the tunnelling current through electrode-base-electrode within minutes **(88)**. Several attempts have been shown to be successful **(89, 90)**, yet the spatial resolution required for single nucleotide identification remains to be achieved. Alternative ways exist; using nanotubes as internal electrode **(91, 92)** or graphene without the requirement for an internal electrode **(54, 55, 93)**. However, seemingly there is a long way to achieve the sequencing due to the current technological difficulties.

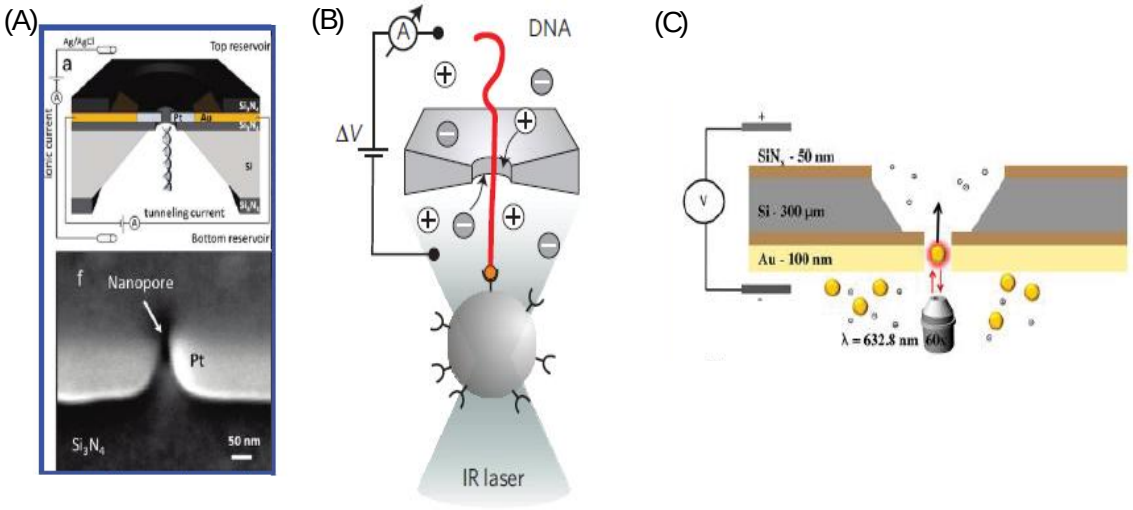

Figure 1.9 Different applications of solid-state nanopores. (A). Top image: Sketch of the experimental setup for a nanopore-based tunnelling current detection for DNA sequencing. Bottom image: SEM image of the nanopore with Pt electrode at the nanopore entrance, fabricated by electron-beam induced deposition. Modified from (89). (B). Schematic of force measurements inside the nanopore, triggered by optical tweezing (94). (C). Schematic of SERRS based nanopore detection used for Au nanoparticle detection (95).

The incorporation of electrochemical detection with other techniques such as optical methods **(96-102)**, magnetic tweezers **(103)** and Atomic Force Microscopy (AFM) **(104)** has also received much attention. The combination offers many possibilities including the direct force measurements on the translocating molecule, real-time monitoring of the capture process, and the measurement of biophysical properties of the molecule in solution. The optical techniques can either be based on optical tweezers **(96)** or highly sensitive fluorescence measurements using a Confocal Microscope in combination with wide-field fluorescence imaging **(97, 101)**, Total Internal Reflection Spectroscopy (TIRF) **(99, 105)** or Surface-Enhanced Resonance Raman Spectroscopy, SERRS **(106)**. Magnetic tweezers and AFM also work in a similar manner to the optical tweezers by trapping a single molecule inside the nanopore and controlling the translocation process while measuring the relevant qualities of the translocation process such as driving force, drag force, and the properties of the analyte (e.g. effective charge). Fluorescence microscopy and TIRF studies are also impressive, because, the techniques allow the real-time monitoring of the capture process without any external interference to the molecule. Moreover,

an attractive application, the optical sequencing of a specific code in a DNA strand, is possible too, as reported by McNally *et al* **(105)**. The only drawback of optical techniques is that they require the labelling of molecules and high-tech instrumentation and are also difficult to miniaturize.

1.5 Nanopore integrated microfluidic systems

Nanopore detection holds great promise in the field of biosensing as shown above; whether naked or functionalized, electrochemical or optical. However the future of nanopores arguably lies in their integration with microfluidic networks since the power of microfluidic systems is compelling. There are a few examples published recently, which illustrate the combination of several different types of solid-state nanopore chips with microfluidic channels **(107-114)**. Interestingly, the integration of nanopore arrays into microfluidic channel networks is not new and the origin of their integration goes back to the late 1990's, even before the realization of single solid-state nanopores. Jong *et al* points out that nanopore arrays are mostly called 'membranes' in literature and are not even recognized for their functionalities once integrated into microfluidic channels **(115)**. As a matter of scientific terminology, their integration is either named by their functionalities such as sample pre- treatment, purification and separation or by an alternative term like filter, sieve, and film. Nevertheless, given the importance to the nanopore sensing technology, recent works have been published as nanopore/nanopore arrays[13] integrated microfluidic systems.

For example, Kovarik and Jacobson sandwiched a tracked etched nanoporous polymer membrane between two poly(dimethysiloxane) (PDMS[14]) microfluidic channels to trap bacterial cells, as well as nonbiological particles, using electrophoresis and dielectrophoresis, as shown in Figure 1.10A **(107)**. Likewise, Guo *et al* demonstrated the capture and release of cyanobacteria in an array of polymeric nanopores embedded between two microfluidic compartments **(111)**. In

[13] Or nanoporous membrane.
[14] PDMS is one of the most popular materials that have been utilized to fabricate microfluidic systems, as discussed in more detail in CHAPTER 4.

addition, the group also showed the selective capture of the bacteria from a suspension of two different kinds. Another application of nanoporous integrated circuits has been shown for size selective DNA transport based on monitoring the capture optically **(108)**. Relevant figures of the device schematics can be seen in Figure 1.10E and Figure 1.10B, respectively.

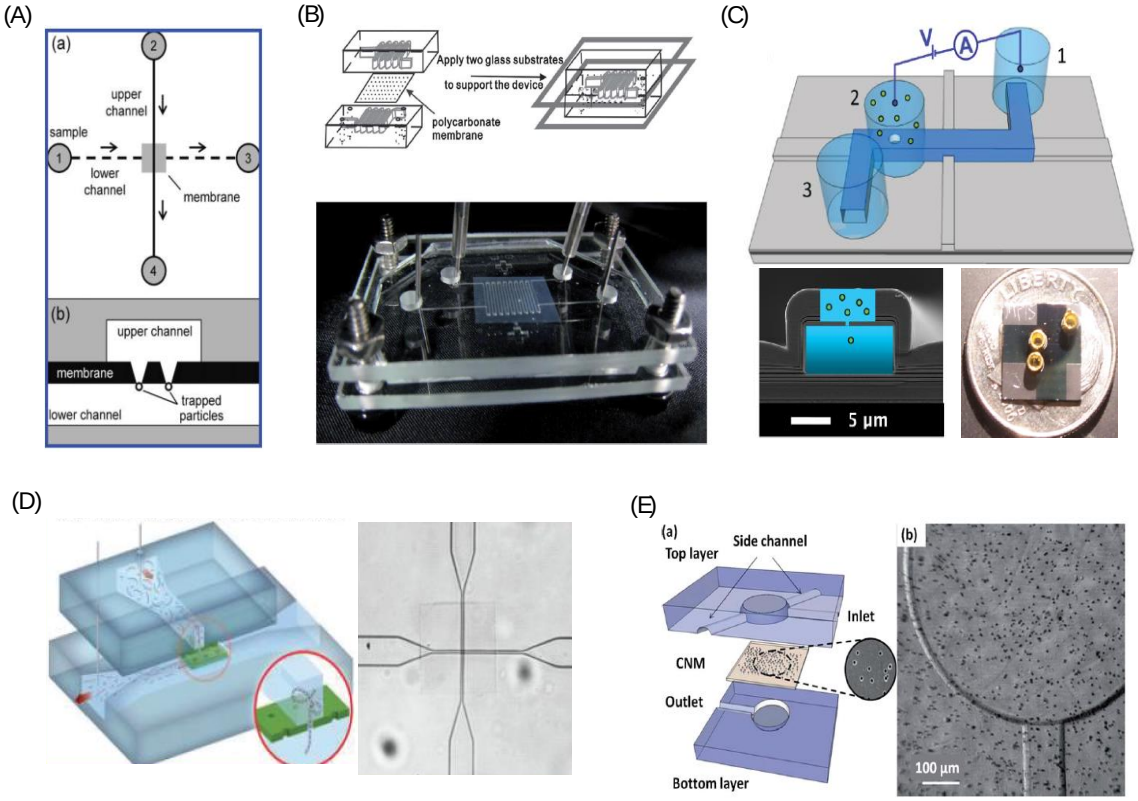

Figure 1.10 Several examples of nanopore arrays and nanopore integrated microfluidic biosensing devices. (A). Track etched nanoporous polymeric membrane integrated into two microfluidic channels which is positioned perpendicular to each other. (107). (B). Schematic of a polycarbonate nanopore arrays stack between two microfluidic channels for optical detection of different DNA fragments in length. (116). (C). Example of a nanopore/micropore system consisting of several SiN and SiO_2 layers supported on a Si subsrate. (117). (D). Nanopore array, made of SiN, integrated microfluidic device for improved nanopore performance and electrochemical detection of DNA (118). (E). Example of a track etched nanoporour polymeric membrane integrated into microfluidic system for the study of bacterial cells (111).

For single solid-state nanopore integrated systems, Rudenko *et al* have illustrated the fabrication of microfluidic/nanopore on a hybrid device, as shown in Figure 1.10C **(119)**, followed by the translocation of ribosomal subunits **(117)**. The device composes of several layers of SiN and SiO_2 and is initially designed to serve as liquid-core optical waveguides due to its

multi layer dielectric structure. It is, therefore, suggested that the electrochemical measurements can be synchronized with optical measurements, which might be of great advantage. However, its demanding etching and photolithography steps are arguably disadvantages for its usage in nanopore sensing. An alternative way is to fabricate single nanopores using traditional methods and to pack the membrane between two PDMS microfluidic chips or into a single microfluidic chip. In a recent publication, Jain *et al* showed the integration of a traditional SiN nanopore membrane between two microfluidic channels and DNA translocation through the nanopore **(118)**. Additionally, the team has also highlighted that the integration resulted in low noise[15], thus enhanced signal quality. In another study, King *et al* fabricated a single nanopore[16] drilled on a micron thick PDMS and PMMA membrane by FIB, and packed the membrane between two microfluidic channels for optical and electrical detection of DNA translocation in separate platforms **(112)**.

Another interesting application of nanopore integrated microfluidic systems has recently been shown by G. Timp and his colleagues, where they integrated a PDMS microfluidic chip on a traditional SiN nanopore membrane and identified single proteins as well as trapping them at the nanopore entrance **(113)**. Moreover, the group positioned a breast cancer cell onto the nanopore by an optical tweezer and monitored the cell transfection via electroporation optically. Trapping using a microfluidic channel is appealing, because the microfluidic channel offers minimal sample consumption and the ease in positioning the cell. The experiment can potentially be extended to study the folding and unfolding characteristics of the molecules in cells.

1.6 Motivation

Clearly the applications of nanopores in biological science are vast and promising. However, the versatility of nanopore sensing is still limited to traditional ways such as bulky electrochemical setups. Since the miniaturized integrated biosensors hold the future, the way

[15] Noise in nanopore membranes is explained in CHAPTER 2.
[16] It can rather be regarded as a nanochannel.

forward for nanopore sensing should be to increase its utility by integrating them into microfluidic channels and thereby to produce portable hybrid nanopore devices.

Recalling the advantages of microfluidic systems, they offer a range of flexibility such as compactness, less sample consumption, quicker response time and above all cheaper production. It is also possible to design highly complex and sophisticated channel networks, despite the fact that the entire chip stays as small as possible. Although microfluidic networks have been used intensively for different biosensing applications, there are only a few that can potentially probe single molecules with high accuracy within seconds and they are mostly based on fluorescence detection **(120)**.

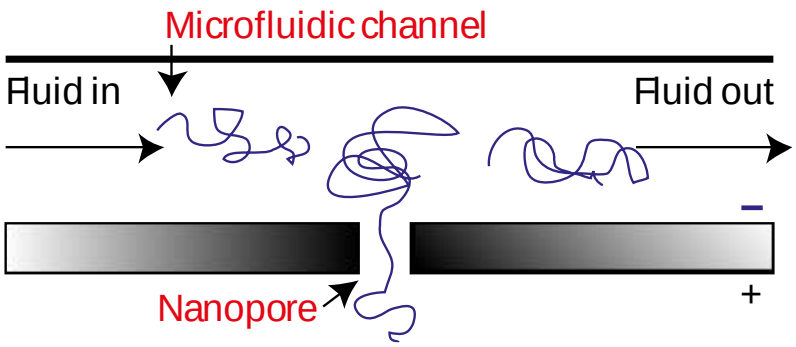

Figure 1.11 Schematic of the single nanopore integrated microfluidic chip.

The main objective of this thesis was, therefore, to develop a methodology that allows the integration of single solid-state nanopores into microfluidic channel networks and the study of single molecule detection, especially under continuous flow conditions. The employment of continuous flow is rather interesting, as it is a prerequisite for the functionality of microfluidic channels in a lab-on-chip device. By achieving this, one can construct a monolithic device that enables the detection of single species while being simultaneously processed (e.g. sample purification, separation, and amplification if necessary). A further advantage of the integrated chip is the requirement of a lower amount of sample compared to traditional nanopore platforms[17].

[17] Typical volume of a traditional nanopore cell compartment is 1 ml.

The working principle of the planned device is as follows; DNA sample prepared in an electrolyte solution is infused through the microfluidic channel, as illustrated in Figure 1.11. Electrodes are inserted to corresponding electrolyte chambers; one is at the outlet of microfluidic channel (cis), the other is at the back side of the chip (trans). Once a certain voltage is applied across the membrane, the electric field generated across the pore forces DNA to transverse to the other side of the nanopore from the inset of the microfluidic channel, whether it be in the absence or in the presence of flow.

1.7 Outline of the thesis

CHAPTER 2 describes the fabrication and the electrochemical characterization of nanopore devices. Two different types of nanopore membranes were chosen; one is a novel polymeric membrane (Polyimide), and the other one is commonly used SiN. The chapter starts with the description of the milling methods and the fabrication procedure for each membrane. It continues with an introduction to the instrumentation and the experimental setup that has been used in the electrochemical measurements. The last part of the chapter is mainly devoted to the studies carried out to characterize the polyimide nanopores, which also illustrates the reason for studying SiN nanopore devices in the following sections.

CHAPTER 3 deals with the fabrication of ultra-thin SiN membranes using reactive ion etch technique, the optimization of the fabrication conditions, SEM and AFM characterization of the thinned membranes. In addition, nanopore fabrication procedure and DNA detection using thinned nanopore devices are shown.

CHAPTER 4 presents a detailed overview of the design considerations of the PDMS microfluidic chip and the integration process of the SiN nanopore chip into the microfluidic channel. The section ends with the description of the electrochemical set-up of the integrated chip used in electrochemistry experiments.

Optical studies to determine the flow rates used in electrochemical experiments are tackled in CHAPTER 5, where the main objective was to define the transition between diffusion- and flow-

limited regimes, and to monitor DNA behaviour in flow. The chapter therefore starts with an introduction to the fundamentals of fluorescence detection and the requirements for the optical instrumentation. In addition, physical qualities of DNA are introduced briefly. In the experimental section, we first show the velocity measurements calculated using the results obtained from both wide-field and confocal microscopy. It is followed by the analysis of conformational changes of the DNA strand in flow. Confocal measurements involving the principles of fluorescence correlation spectroscopy provide an understanding of the transition from diffusion-limited regime to flow-limited regime at the chosen flow rates whereas the velocity measurements using wide-field imaging elaborate not only on the speed but also the conformation of DNA in flow.

CHAPTER 6 is dedicated to the electrochemical characterization of the integrated chip at the chosen flow rates and electrochemical detection of DNA in the absence and presence of hydrodynamic pressure-driven flow. First, possible scenarios for the capture of the molecule by the nanopore in flow are discussed. Moving on to the experimental results, we show the effect of flow rate in nanopore conductance and noise. In the final part of the chapter, DNA translocation in the absence and presence of flow is shown and discussed.

CHAPTER 7 summarizes the scope of this thesis and the work that has been shown. The chapter ends with the future directions.

References

1. Thevenot DR, Toth K, Durst RA, Wilson GS. Electrochemical Biosensors: Recommended Definitions and Classification. Anal Lett. 2001;34(5):635-59.

2. Setford SJ, Newman JD. Enzyme Biosensors. Microbial Enzymes and Biotransformations. 2005;17:29-60.

3. **Clark LC, Lyons C**. Electrode Systems for Continous Monitoring in Cardiovascular Surgery. Annals of the New York Academy of Sciences. 1962;102(1):29-45.

4. Manz A, Graber N, Widmer HM. Miniaturized Total Chemical Analysis Systems: A Novel Concept for Chemical Sensing. Sensors and Actuators B: Chemical. 1990;1(1–6):244-8.

5. Martinez AW, Phillips ST, Whitesides GM, Carrilho E. Diagnostics for the Developing World: Microfluidic Paper-Based Analytical Devices. Analytical Chemistry. 2009;82(1):3-10.

6. Burns MA, Johnson BN, Brahmasandra SN, Handique K, Webster JR, Krishnan M, et al. An Integrated Nanoliter DNA Analysis Device. Science. 1998;282(5388):484-7.

7. **Tabelling P**. Introduction to Microfluidics. New York: Oxford University Press Inc.; 2005.

8. Jacobson SC, Hergenroder R, Moore AW, Jr., Ramsey JM. Precolumn Reactions with Electrophoretic Analysis Integrated on a Microchip. Analytical Chemistry. 1994;66(23):4127-32.

9. Abgrall P. Lab-on-Chip Technologies: Making a Microfluidic Network and Coupling It into a Complete Microsystem—a Review. Journal of micromechanics and microengineering. 2007;17(5):R15.

10. Kovarik ML, Jacobson SC. Nanofluidics in Lab-on-a-Chip Devices. Analytical Chemistry. 2009;81(17):7133-40.

11. Han J, Turner SW, Craighead HG. Entropic Trapping and Escape of Long DNA Molecules at Submicron Size Constriction. Physical Review Letters. 1999;83(8):1688-91.

12. Fu J, Schoch RB, Stevens AL, Tannenbaum SR, Han J. A Patterned Anisotropic Nanofluidic Sieving Structure for Continuous-Flow Separation of DNA and Proteins. Nat Nano. 2007;2(2):121-8.

13. **Mokkapati VRSS, Di Virgilio V, Shen C, Mollinger J, Bastemeijer J, Bossche A**. DNA Tracking within a Nanochannel: Device Fabrication and Experiments. Lab on a Chip. 2011;11(16):2711-9.

14. Reisner W, Larsen NB, Silahtaroglu A, Kristensen A, Tommerup N, Tegenfeldt JO, et al. Single-Molecule Denaturation Mapping of DNA in Nanofluidic Channels. Proceedings of the National Academy of Sciences of the United States of America. 2010;107(30):13294-9.

15. **Fanzio P, Mussi V, Manneschi C, Angeli E, Firpo G, Repetto L, et al.** DNA Detection with a Polymeric Nanochannel Device. Lab on a Chip. 2011;11(17):2961-6.

16. Sen Y-H, Jain T, Aguilar CA, Karnik R. Enhanced Discrimination of DNA Molecules in Nanofluidic Channels through Multiple Measurements. Lab on a Chip. 2012;12(6):1094-101.

17. Zevenbergen MAG, Singh PS, Goluch ED, Wolfrum BL, Lemay SG. Stochastic Sensing of Single Molecules in a Nanofluidic Electrochemical Device. Nano Letters. 2011;11(7):2881-6.

18. **Hong J, Edel JB, deMello AJ**. Micro- and Nanofluidic Systems for High-Throughput Biological Screening. Drug Discovery Today. 2009;14(3–4):134-46.

19. Mastrangelo CH, Burns MA, Burke DT. Microfabricated Devices for Genetic Diagnostics. Proceedings of the IEEE. 1998;86(8):1769-87.

20. **Whitesides GM**. The Origins and the Future of Microfluidics. Nature. 2006;442(7101):368-73.

21. Moldavan A. Photo-Electric Technique for the Counting of Microscopial Cells. Science. 1934;80(2069):188-9.

22. Coulter WH, inventor; Coulter, Wallace H., assignee. Means for Counting Particles Suspended in a Fluid. United States1953.

23. Kubitschek HE. Electronic Counting and Sizing of Bacteria. Nature. 1958;182(4630):234-5.

24. DeBlois R. Counting and Sizing of Submicron Particles by the Resistive Pulse Technique. Review of Scientific Instruments. 1970;41(7):909.

25. Brecher G, Schneiderman M, Williams GZ. Evaluation of Electronic Red Blood Cell Counter. American journal of clinical pathology. 1956;26(12):1439-49.

26. Mattern CF, Brackett FS, Olson BJ. Determination of Number and Size of Particles by Electrical Gating: Blood Cells. Journal of applied physiology. 1957;10(1):56-70.

27. Epstein SS, Weiss JB. Measuring the Size of Isolated Cells. Nature. 1960;187(4736):461-3.

28. Haydon DA, Hladky SB. Ion Transport across Thin Lipid Membranes: A Critical Discussion of Mechanisms in Selected Systems. Quarterly Reviews of Biophysics. 1972;5(02):187-282.

29. Neher E, Sakmann B. Single-Channel Currents Recorded from Membrane of Denervated Frog Muscle Fibres. Nature. 1976;260(5554):799-802.

30. **Bezrukov SM, Vodyanoy I, Parsegian VA**. Counting Polymers Moving through a Single Ion Channel. Nature. 1994;370(6487):279-81.

31. Kasianowicz JJ, Brandin E, Branton D, Deamer DW. Characterization of Individual Polynucleotide Molecules Using a Membrane Channel. Proceedings of the National Academy of Sciences of the United States of America. 1996;93(24):13770-3.

32. Wanunu M, Morrison W, Rabin Y, Grosberg AY, Meller A. Electrostatic Focusing of Unlabelled DNA into Nanoscale Pores Using a Salt Gradient. Nat Nano. 2010;5(2):160-5.

33. Xie P, Xiong Q, Fang Y, Qing Q, Lieber CM. Local Electrical Potential Detection of DNA by Nanowire-Nanopore Sensors. Nat Nano. 2012;7(2):119-25.

34. Meller A, Branton D. Single Molecule Measurements of DNA Transport through a Nanopore. ELECTROPHORESIS. 2002;23(16):2583-91.

35. **Han J, Craighead HG**. Separation of Long DNA Molecules in a Microfabricated Entropic Trap Array. Science. 2000;288(5468):1026-9.

36. Albrecht T, Gibb T, Nuttall P. Ion Transport in Nanopores. In: Edel JB, Albrecht T, editors. Engineered Nanopores for Bioanalytical Applications. Oxford: William Andrew Publishing; 2013. p. 1-30.

37. Vodyanoy I, Bezrukov SM. Sizing of an Ion Pore by Access Resistance Measurements. Biophysical Journal. 1992;62(1):10-1.

38. **Hille B**. Pharmacological Modifications of the Sodium Channels of Frog Nerve. The Journal of general physiology. 1968;51(2):199-219.

39. **Hall JE**. Access Resistance of a Small Circular Pore. The Journal of general physiology. 1975;66(4):531-2.

40. **Ayub M, Ivanov A, Instuli E, Cecchini M, Chansin G, McGilvery C, et al.** Nanopore/Electrode Structures for Single-Molecule Biosensing. Electrochimica Acta. 2010;55(27):8237-43.

41. **Chen P, Gu J, Brandin E, Kim Y, Wang Q, Branton D**. Probing Single DNA Molecule Transport Using Fabricated Nanopores. Nano Letters. 2004;4(11):2293-8.

42. Wanunu M. Nanopores: A Journey Towards DNA Sequencing. Physics of Life Reviews. 2012;9(2):125-58.

43. **Storm AJ, Chen JH, Zandbergen HW, Dekker C**. Translocation of Double-Strand DNA through a Silicon Oxide Nanopore. Phys Rev E. 2005;71(Copyright (C) 2010 The American Physical Society):051903.

44. Storm AJ, Storm C, Chen J, Zandbergen H, Joanny J-F, Dekker C. Fast DNA Translocation through a Solid-State Nanopore. Nano Letters. 2005;5(7):1193-7.

45. **Wanunu M, Sutin J, McNally B, Chow A, Meller A**. DNA Translocation Governed by Interactions with Solid-State Nanopores. Biophysical Journal. 2008;95(10):4716-25.

46. Song LZ, Hobaugh MR, Shustak C, Cheley S, Bayley H, Gouaux JE. Structure of Staphylococcal Alpha-Hemolysin, a Heptameric Transmembrane Pore. Science. 1996;274(5294):1859-66.

47. **Butler TZ, Pavlenok M, Derrington IM, Niederweis M, Gundlach JH**. Single-Molecule DNA Detection with an Engineered Mspa Protein Nanopore. Proceedings of the National Academy of Sciences. 2008;105(52):20647-52.

48. Wendell D, Jing P, Geng J, Subramaniam V, Lee TJ, Montemagno C, et al. Translocation of Double-Stranded DNA through Membrane-Adapted Phi29 Motor Protein Nanopores. Nat Nano. 2009;4(11):765-72.

49. Howorka S, Siwy Z. Nanopore Analytics: Sensing of Single Molecules. Chemical Society Reviews. 2009;38(8):2360-84.

50. Wanunu M, Meller A. Single-Molecule Analysis of Nucleic Acids and DNA-Protein Interactions Using Nanopores. In: Ha PSaTJ, editor. Single-Molecule Techniques: A Laboratory Manual. . Cold Spring Harbor, New York: Cold Spring Harbor Laboratory Press; 2008. p. 395-420.

51. **Li J, Stein D, McMullan C, Branton D, Aziz MJ, Golovchenko JA**. Ion-Beam Sculpting at Nanometre Length Scales. Nature. 2001;412(6843):166-9.

52. Storm AJ, Chen JH, Ling XS, Zandbergen HW, Dekker C. Fabrication of Solid-State Nanopores with Single-Nanometre Precision. Nat Mater. 2003;2(8):537-40.

53. Venkatesan BM, Dorvel B, Yemenicioglu S, Watkins N, Petrov I, Bashir R. Highly Sensitive, Mechanically Stable Nanopore Sensors for DNA Analysis. Adv Mater. 2009;21(27):2771-+.

54. **Garaj S, Hubbard W, Reina A, Kong J, Branton D, Golovchenko JA**. Graphene as a Subnanometre Trans-Electrode Membrane. Nature. 2010;467(7312):190-3.

55. Merchant CA, Healy K, Wanunu M, Ray V, Peterman N, Bartel J, et al. DNA Translocation through Graphene Nanopores. Nano Letters. 2010;10(8):2915-21.

56. Postma HWC. Rapid Sequencing of Individual DNA Molecules in Graphene Nanogaps. Nano Letters. 2010;10(2):420-5.

57. Mara A, Siwy Z, Trautmann C, Wan J, Kamme F. An Asymmetric Polymer Nanopore for Sing**le** Molecule Detection. Nano Letters. 2004;4(3):497-501.

58. Harrell CC, Choi Y, Horne LP, Baker LA, Siwy ZS, Martin CR. Resistive-Pulse DNA Detection with a Conical Nanopore Sensor. Langmuir. 2006;22(25):10837-43.

59. **Steinbock LJ, Otto O, Chimerel C, Gornall J, Keyser UF**. Detecting DNA Folding with Nanocapillaries. Nano Letters. 2010.

60. Bell NAW, Thacker VV, Hernandez-Ainsa S, Fuentes-Perez ME, Moreno-Herrero F, Liedl T, et al. Multiplexed Ionic Current Sensing with Glass Nanopores. Lab on a Chip. 2013;13(10):1859-62.

61. Sun L, Crooks RM. Fabrication and Characterization of Single Pores for Modeling Mass Transport across Porous Membranes. Langmuir. 1999;15(3):738-41.

62. Ito T, Sun L, Henriquez RR, Crooks RM. A Carbon Nanotube-Based Coulter Nanoparticle Counter. Accounts of Chemical Research. 2004;37(12):937-45.

63. **Fan R, Karnik R, Yue M, Li D, Majumdar A, Yang P**. DNA Translocation in Inorganic Nanotubes. Nano Letters. 2005;5(9):1633-7.

64. Liu H, He J, Tang J, Liu H, Pang P, Cao D, et al. Translocation of Single-Stranded DNA through Single-Walled Carbon Nanotubes. Science. 2010;327(5961):64-7.

65. Bahrami A, Dogan F, Japrung D, Albrecht T. Solid-State Nanopores for Biosensing with Submolecular Resolution. Biochem Soc Trans. 2012;40(4):624-8.

66. **Li J, Gershow M, Stein D, Brandin E, Golovchenko JA**. DNA Molecules and Configurations in a Solid-State Nanopore Microscope. Nat Mater. 2003;2(9):611-5.

67. **Healy K, Schiedt B, Morrison AP**. Solid-State Nanopore Technologies for Nanopore-Based DNA Analysis. Nanomedicine-Uk. 2007;2(6):875-97.

68. Harrer S. Electrochemical Protection of Thin Film Electrodes in Solid State Nanopores. Nanotechnology. 2011;22(27):275304.

69. **Miles BN, Ivanov AP, Wilson KA, Dogan F, Japrung D, Edel JB**. Single Molecule Sensing with Solid-State Nanopores: Novel Materials, Methods, and Applications. Chemical Society Reviews. 2013;42(1):15-28.

70. Hou X, Guo W, Jiang L. Biomimetic Smart Nanopores and Nanochannels. Chemical Society Reviews. 2011;40(5):2385-401.

71. Kowalczyk SW, Blosser TR, Dekker C. Biomimetic Nanopores: Learning from and About Nature. Trends Biotechnol. 2011;29(12):607-14.

72. Kowalczyk SW, Tuijtel MW, Donkers SP, Dekker C. Unraveling Single-Stranded DNA in a Solid-State Nanopore. Nano Letters. 2010;10(4):1414-20.

73. **Skinner GM, van den Hout M, Broekmans O, Dekker C, Dekker NH**. Distinguishing Single- and Double-Stranded Nucleic Acid Molecules Using Solid-State Nanopores. Nano Letters. 2009;9(8):2953-60.

74. Wanunu M, Dadosh T, Ray V, Jin J, McReynolds L, Drndic M. Rapid Electronic Detection of Probe-Specific Micrornas Using Thin Nanopore Sensors. Nat Nano. 2010;5(11):807-14.

75. Fologea D, Ledden B, McNabb DS, Li J. Electrical Characterization of Protein Molecules by a Solid-State Nanopore. Applied Physics Letters. 2007;91(5):053901.

76. **Sexton LT, Horne LP, Sherrill SA, Bishop GW, Baker LA, Martin CR**. Resistive-Pulse Studies of Proteins and Protein/Antibody Complexes Using a Conical Nanotube Sensor. Journal of the American Chemical Society. 2007;129(43):13144-52.

77. Sexton LT, Mukaibo H, Katira P, Hess H, Sherrill SA, Horne LP, et al. An Adsorption-Based Model for Pulse Duration in Resistive-Pulse Protein Sensing. Journal of the American Chemical Society. 2010;132(19):6755-63.

78. Wei R, Gatterdam V, Wieneke R, Tampe R, Rant U. Stochastic Sensing of Proteins with Receptor-Modified Solid-State Nanopores. Nat Nano. 2012;7(4):257-63.

79. Singer A, Rapireddy S, Ly DH, Meller A. Electronic Barcoding of a Viral Gene at the Single-Molecule Level. Nano Letters. 2012;12(3):1722-8.

80. **Singer A, Wanunu M, Morrison W, Kuhn H, Frank-Kamenetskii M, Meller A**. Nanopore Based Sequence Specific Detection of Duplex DNA for Genomic Profiling. Nano Letters. 2010;10(2):738-42.

81. **Wanunu M, Sutin J, Meller A**. DNA Profiling Using Solid-State Nanopores: Detection of DNA-Binding Molecules. Nano Letters. 2009;9(10):3498-502.

82. **Kowalczyk SW, Hall AR, Dekker C**. Detection of Local Protein Structures Along DNA Using Solid-State Nanopores. Nano Letters. 2009;10(1):324-8.

83. Raillon C, Cousin P, Traversi F, Garcia-Cordero E, Hernandez N, Radenovic A. Nanopore Detection of Single Molecule Rnap–DNA Transcription Complex. Nano Letters. 2012;12(3):1157-64.

84. **Wanunu M, Bhattacharya S, Xie Y, Tor Y, Aksimentiev A, Drndic M**. Nanopore Analysis of Individual Rna/Antibiotic Complexes. ACS Nano. 2011;5(12):9345-53.

85. Uram JD, Ke K, Hunt AJ, Mayer M. Submicrometer Pore-Based Characterization and Quantification of Antibody–Virus Interactions. Small. 2006;2(8-9):967-72.

86. Mirsaidov U, Timp W, Zou X, Dimitrov V, Schulten K, Feinberg AP, et al. Nanoelectromechanics of Methylated DNA in a Synthetic Nanopore. Biophysical Journal. 2009;96(4):L32-L4.

87. Wanunu M, Cohen-Karni D, Johnson RR, Fields L, Benner J, Peterman N, et al. Discrimination of Methylcytosine from Hydroxymethylcytosine in DNA Molecules. Journal of the American Chemical Society. 2011;133(3):486-92.

88. **Zwolak M, Di Ventra M**. Electronic Signature of DNA Nucleotides Via Transverse Transport. Nano Letters. 2005;5(3):421-4.

89. Ivanov AP, Instuli E, McGilvery CM, Baldwin G, McComb DW, Albrecht T, et al. DNA Tunneling Detector Embedded in a Nanopore. Nano Letters. 2011;11(1):279-85.

90. Tsutsui M, Rahong S, Iizumi Y, Okazaki T, Taniguchi M, Kawai T. Single-Molecule Sensing Electrode Embedded in-Plane Nanopore. Sci Rep. 2011;1.

91. He J. Translocation Events in a Single-Walled Carbon Nanotube. Journal of physics Condensed matter. 2010;22(45):454112.

92. **Sadki ES, Garaj S, Vlassarev D, Golovchenko JA, Branton D**. Embedding a Carbon Nanotube across the Diameter of a Solid State Nanopore. Journal of Vacuum Science & Technology B: Microelectronics and Nanometer Structures. 2011;29(5):053001--4.

93. Schneider GgF, Kowalczyk SW, Calado VE, Pandraud Gg, Zandbergen HW, Vandersypen LMK, et al. DNA Translocation through Graphene Nanopores. Nano Letters. 2010;10(8):3163-7.

94. **van Dorp S, Keyser UF, Dekker NH, Dekker C, Lemay SG**. Origin of the Electrophoretic Force on DNA in Solid-State Nanopores. Nat Phys. 2009;5(5):347-51.

95. **Cecchini MP, Wiener A, Turek VA, Chon H, Lee S, Ivanov AP, et al.** Rapid Ultrasensitive Single Particle Surface-Enhanced Raman Spectroscopy Using Metallic Nanopores. Nano Letters. 2013;13(10):4602-9.

96. **Keyser UF, Koeleman BN, van Dorp S, Krapf D, Smeets RMM, Lemay SG, et al.** Direct Force Measurements on DNA in a Solid-State Nanopore. Nat Phys. 2006;2(7):473-7.

97. Chansin GAT, Mulero R, Hong J, Kim MJ, Demello AJ, Edel JB. Single-Molecule Spectroscopy Using Nanoporous Membranes. Nano Letters. 2007;7:2901-6.

98. **McNally B, Singer A, Yu Z, Sun Y, Weng Z, Meller A**. Optical Recognition of Converted DNA Nucleotides for Single-Molecule DNA Sequencing Using Nanopore Arrays. Nano Letters. 2010.

99. Soni GV, Singer A, Yu ZL, Sun YJ, McNally B, Meller A. Synchronous Optical and Electrical Detection of Biomolecules Traversing through Solid-State Nanopores. Review of Scientific Instruments. 2010;81(1):-.

100. van den Hout M, Vilfan ID, Hage S, Dekker NH. Direct Force Measurements on Double-Stranded Rna in Solid-State Nanopores. Nano Letters. 2010;10(2):701-7.

101. Hong J, Lee Y, Chansin GAT, Edel JB, Demello AJ. Design of a Solid-State Nanopore-Based Platform for Single-Molecule Spectroscopy. Nanotechnology. 2008;19(16).

102. Ando G, Hyun C, Li J, Mitsui T. Directly Observing the Motion of DNA Molecules near Solid-State Nanopores. ACS Nano. 2012;6(11):10090-7.

103. Peng H, Ling XS. Reverse DNA Translocation through a Solid-State Nanopore by Magnetic Tweezers. Nanotechnology. 2009;20(18).

104. King GM, Golovchenko JA. Probing Nanotube-Nanopore Interactions. Physical Review Letters. 2005;95(21).

105. McNally B, Singer A, Yu ZL, Sun YJ, Weng ZP, Meller A. Optical Recognition of Converted DNA Nucleotides for Single-Molecule DNA Sequencing Using Nanopore Arrays. Nano Letters. 2010;10(6):2237-44.

106. Cecchini MP, Wiener A, Turek VA, Chon H, Lee S, Ivanov AP, et al. Rapid Ultrasensitive Single Particle Surface-Enhanced Raman Spectroscopy Using Metallic Nanopores. Nano Letters. 2013.

107. Kovarik ML, Jacobson SC. Integrated Nanopore/Microchannel Devices for Ac Electrokinetic Trapping of Particles. Analytical Chemistry. 2008;80(3):657-64.

108. Sheng Y, Bowser MT. Size Selective DNA Transport through a Nanoporous Membrane in a Pdms Microfluidic Device. Analyst. 2012.

109. Rudenko MI, Yin D, Holmes M, Hawkins AR, Schmidt H, editors. Integration and Characterization of Sin Nanopores for Single-Molecule Detection in Liquid-Core Arrow Waveguides2007: SPIE.

110. Jain T, Guerrero RJS, Aguilar CA, Karnik R. Integration of Solid-State Nanopores in Microfluidic Networks Via Transfer Printing of Suspended Membranes. Analytical Chemistry. 2013;85(8):3871-8.

111. Guo P, Hall EW, Schirhagl R, Mukaibo H, Martin CR, Zare RN. Microfluidic Capture and Release of Bacteria in a Conical Nanopore Array. Lab on a Chip. 2012;12(3):558-61.

112. King TL, Gatimu EN, Bohn PW. Single Nanopore Transport of Synthetic and Biological Polyelectrolytes in Three-Dimensional Hybrid Microfluidic/Nanofluidic Devices. Biomicrofluidics. 2009;3(1).

113. Nelson EM, Kurz V, Shim J, Timp W, Timp G. Using a Nanopore for Single Molecule Detection and Single Cell Transfection. Analyst. 2012;137(13):3020-7.

114. Zhe J, Jagtiani A, Dutta P, Hu J, Carletta J. A Micromachined High Throughput Coulter Counter for Bioparticle Detection and Counting. Journal of micromechanics and microengineering. 2007;17(2):304-13.

115. de Jong J, Lammertink RGH, Wessling M. Membranes and Microfluidics: A Review. Lab on a Chip. 2006;6(9):1125-39.

116. Sheng Y, Bowser MT. Size Selective DNA Transport through a Nanoporous Membrane in a Pdms Microfluidic Device. Analyst. 2012;137(5):1144-51.

117. **Rudenko MI, Holmes MR, Ermolenko DN, Lunt EJ, Gerhardt S, Noller HF, et al.** Controlled Gating and Electrical Detection of Single 50s Ribosomal Subunits through a Solid-State Nanopore in a Microfluidic Chip. Biosens Bioelectron. 2011;29(1):34-9.

118. Jain T, Guerrero RJS, Aguilar CA, Karnik R. Integration of Solid-State Nanopores in Microfluidic Networks Via Transfer Printing of Suspended Membranes. Analytical Chemistry. 2013.

119. Holmes MR, Shang T, Hawkins AR, Rudenko M, Measor P, Schmidt H. Micropore and Nanopore Fabrication in Hollow Antiresonant Reflecting Optical Waveguides. J Micro Nanolithogr MEMS MOEMS. 2010;9(2):23004.

120. Streets AM, Huang Y. Microfluidics for Biological Measurements with Single-Molecule Resolution. Curr Opin Biotechnol. 2014;25(0):69-77.

CHAPTER 2
Fabrication and Characterization

Chapter 2 is divided into two main sections; fabrication of single nanopores using two different membrane materials, polyimide and SiN, and electrochemical characterization of the nanopores. First we shall briefly introduce the methods that have been utilized for nanopore fabrication in the field and the technique that was chosen in this work, milling with a Focused Ion Beam, followed by the experimental procedure from a general perspective. Membrane materials, their fabrication, and nanopore fabrication using the aforementioned membranes are discussed in detail later in the text, respectively. The last section is dedicated to electrochemical studies which include a short introduction to instrumentation, electrochemical set-up and preparations, and electrochemical characterization of nanopores in terms of nanopore conductance and noise.

A solid-state nanopore can be fabricated on any insulating or semiconducting material provided that the material is compatible with easily accessible microfabrication techniques and that it provides a sufficient electrical insulation once engineered as a free-standing membrane, typically 30–100 nm thick. Namely, the prerequisite for the membrane is its nonporous robust structure so that the only connection between electrolyte compartments during electrical current recordings is the nanopore. A selection of membrane materials has been given already in CHAPTER 1. The key point is that each membrane material has its own advantages and disadvantages in terms of fabrication, electric noise, geometrical constraints, surface properties, and compatibility with chemical and mechanical modifications for a particular application and so on. As a result, the most suitable membrane material is decided by the nanopore user with respect to the overall project aims.

2.1 Nanopore fabrication

2.1.1 Nanopore fabrication techniques

Using a focused electron beam is a common method to fabricate or resize large pores and provides very precise pore dimensions (e.g. <20 nm in diameter). Ion beam technologies are also preferably the choice of nanopore users thanks to their flexibility in terms of the achievable pore dimensions and the materials used. Different ion beam sources are available including Ga^+, He^+, Ne^+, Ar^+, Xe^+, and Kr^+**(1-3)**. Ga^+ ion beams have been the most frequently used technique, generally producing 20 nm or larger diameter pores. Although smaller pores are also reported by Giearak *et al* the ion implantation of the Ga^+ ion beam into the nanopore surface remains an issue **(4)**. Alternatively, He^+ ion beam can be used as the tip of the beam source is atomically small and thus capable of producing sub-4 nm pores **(5)**. It offers higher imaging resolution without damaging the surface after being processed, higher reproducibility[18], and the elimination of ion implantation. As the field grows, new techniques have recently emerged to create more convenient and versatile ways to fabricate nanopores in a variety of geometries. For instance,

[18] It is another challenge when Ga^+ ion beam is used.

Kuan *et al* reported a new technique based on cold-ion beam (Ar^+) sculpting to fabricate nanopores as small as 6 nm in diameter and about 1 nm in thickness as opposed to the very initial experiments carried out with focused Ar^+ ion beam **(6)**. Another example is metal nanoparticle-assisted plasma etching, which does not require ion- and electron-beam instrumentation due to its lithography-free process **(7)**.

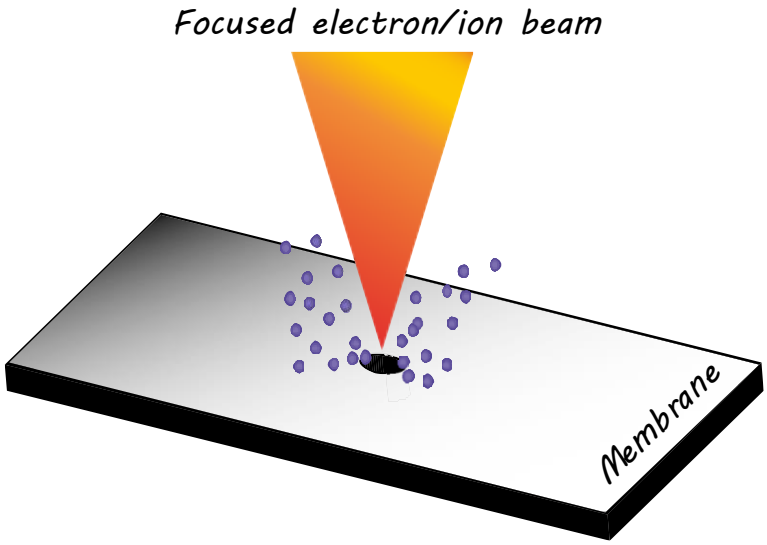

Figure 2.1 Schematic of nanopore fabrication using a focused electron or ion beam.

Nanopore fabrication based on a focused ion beam or electron beam is sketched in Figure 2.1. While the concept for both is same, the mechanism differs. Nanopore drilling by the former is a consequence of sputtering away the membrane surface by elastic atom-atom collisions. In contrast, the application of a highly energetic electron beam can affect nanopore geometry in two ways; direct atomic displacement by the elastic scattering associated with electron-atom interactions, hence the direct nanopore fabrication, or resizing the nanopore shape from a larger diameter to a smaller one by inelastic scattering occurring between the incident electron and the surface atoms **(8)**. While the electron beam interaction with the surface atoms causes localized heating of the surface, the surface free energy has to be minimized by reshaping the atomic structure around the incident area. As a result, surface tension effects deform the material to a more favourable state; either shrinking or expansion. The change in free energy is calculated by Equation 2.1 **(9)**;

$$\Delta F = 2\pi\gamma(d_{pore}L_{pore} - d_{pore}^2)$$ Equation 2.1

where γ is the surface tension, d_{pore} is the initial pore radius. As clearly seen, the numerical relationship between d_{pore} and L_{pore} defines whether the pore is shrunk or enlarged. For example, if the pore size is smaller than $L_{pore}/2$, the pore tends to shrink for a SiO_2 pore and vice versa.

Field emission scanning electron microscopy (FESEM) or conventional SEM is another way of reshaping the nanopore and reported to yield higher shrinking rates compared to TEM **(10-12)**. Upon the irradiation of the surface, the energy-dependant material transfer occurs. Independent of the original pore size, pores can be shrunk from 50–200 nm down to 10 nm. Several parameters that help to manipulate the shrinking process are imaging magnification, exposure time, beam dose and acceleration voltage. For example, as the pore surface is exposed to electron beam with energies ranging from 30 kV to 1 kV for a given time, the shrinking rate increases inversely with increasing beam energy intensity.

2.1.2 Nanopore fabrication using Focused Ion Beam

An ion beam system can either be a custom-built ion beam apparatus **(13)** or a dual beam apparatus which combines an ion beam source (FIB) with an electron beam gun (SEM) **(14, 15)**. The former can be incorporated into a feed-back controlled mechanism where the rate of transmitted ions through the nanopore is counted when the surface erosion reaches the back side of the membrane, forming a nanopore, while SEM is employed for direct imaging of the nanopore fabrication process in a dual beam technology. In fact, the working principle of FIB instrument is similar to that of SEM with a slight difference in beam source; an ion beam source is utilized as opposed to an electron beam gun.

CrossBeam® FIB/SEM system (Carl Zeiss XB1540) was used in the work presented here. As shown in Figure 2.2, SEM column is positioned vertically to the sample holder whereas FIB column is placed near SEM column at a certain angle to the sample holder and the gas injection system (GIS) is seen on the right-hand side. GIS can be used as a source to deposit metals (e.g. Pt, Tungsten, Au) at the pore mouth by electron-beam induced deposition **(16)**. As for the

nanopore fabrication, Ga^+ beam source is utilized to create a tightly focused ion beam where it is focused on a spot on the membrane. SEM is used to monitor the surface change before and after milling process. The process yields the production of pores with a diameter of 30-40 nm in seconds.

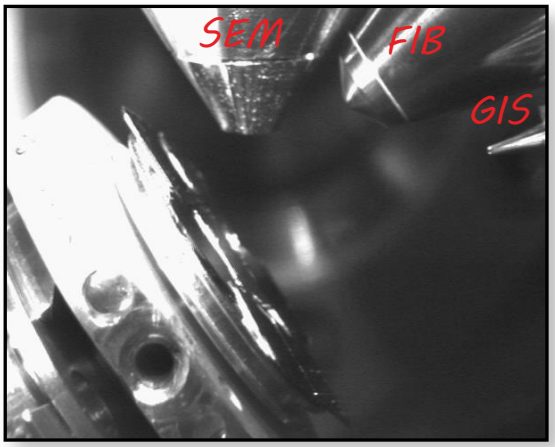

Figure 2.2 Picture of the specimen vacuum chamber of the CrossBeam® FIB/SEM system (Carl Zeiss XB1540).

2.1.3 Experimental procedure for nanopore fabrication

A general procedure for the sample preparation and nanopore fabrication is as follows[19];

- The sample is mounted on an SEM specimen stub with the help of SEM carbon disks. In order to avoid charging of the sample, the chip is grounded by applying a conductive silver paint on a small area of the chip. The stubs are fixed on a multi-stub holder and loaded to the vacuum chamber.
- The system is pumped to 5 x 10^{-6} mbar (system pressure: 5 x 10^{-6} mbar, gun vacuum: 5 x 10^{-10} mbar, sample chamber pressure: $<10^{-2}$ mbar). Samples are loaded to the specimen vacuum chamber and positioned, and the chamber is evacuated before guns are turned on.

[19] Any particular step followed for a specific membrane is given in related sections.

- Sample holder is tilted to 54º with respect to SEM gun where it becomes perpendicular to FIB gun.
- Working distance of SEM gun to the sample is set to 5 mm, called 'coincidence point'. Coincidence point is where ion beam crosses the electron beam after stigmation and aperture alignment is completed for the sharpest image possible on SEM (5 kV acceleration voltage). Beam alignment for a finer adjustment is also performed.
- FIB probe current is set to 30 kV and 1 pA, and corrected for the best focus on FIB.
- Milling process is conducted on SmartSem user interface. Magnification is set to 60 kX, where the pixel size is 4.4 nm and probe size is less than 10 nm for 1 pA beam current. Probe size and pixel size should be almost the same, because the shape of the geometrical feature would be affected by any difference. However, this might be unavoidable in some cases.
- A circular shape of approximately 20 nm features is created on the software after which nanopore is milled for a certain amount of time.
- Milling duration and magnification are changed depending on the sample used whereas other parameters are kept constant, unless stated otherwise.

2.2 The choice of the membrane

In this section, the nanopore fabrication using different membrane materials is shown; one is a novel nanopore platform which consists of an ultra thin polymer membrane, the other is a commonly used solid-state nanopore device; SiN. The properties of the polyimide membrane and nanopore fabrication are explained first. Secondly, the fabrication of SiN membranes and nanopores will be shown followed by the electrochemical characterization of nanopores.

2.2.1 Polyimide nanopores

Common polymer membrane materials are Polyimide (PI) **(17, 18)**, Polyethylene terephthalate (PET) **(19, 20)** and Polycarbonate (PC) **(21)**. Among them, PI seems more preferable because of its excellent mechanical and electrical properties **(22)**, which is perhaps the

reason that many of the single molecule detection experiments were carried out using PI nanopores **(18, 20)**. However current PI membranes used in nanopore experiments such as Kapton films are micron-scale thick, and signal-to-noise ratio (SNR) of the electrochemical signal is reduced according to Equation 1.14 and Equation 1.15. Therefore, the detection becomes challenging. Another disadvantage is the technique used to open the pores in polymeric membranes; feedback controlled track etching. Track etching is a highly demanding method that requires the employment of heavy ions to irradiate the surface followed by chemical etching and the overall process is time-consuming with many etching parameters influencing the pore's formation **(19)**.

In our experiments, nano-scale pores are fabricated in a commercially available, ultra-thin polymer membrane platform using FIB. The membrane is embedded into Quantomix QX-102 WETSEM capsules (Jeol UK) Figure 2.3a, containing a nanoscale thick free-standing PI membrane.

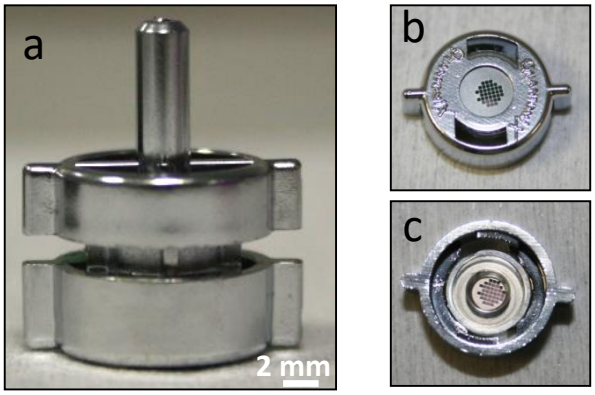

Figure 2.3 Pictures of the capsule and its components (liquid dish and sealing stub). a. Capsule with the liquid dish and the sealing stub (L_{total}: 18.6 mm). b. Bottom view of the liquid dish c. Top view of the liquid dish.

The capsule is conventionally used to image liquid samples through the ultra thin membrane using SEM **(23, 24)**. With its nanoscale free-standing membrane sealed perfectly within a metallic reservoir, it is thought to facilitate the demanding fabrication process of the silicon based-membranes. Furthermore, a polymer membrane might provide higher SNR than the

conventional solid-state nanopores (e.g. SiN) on account of its expected low capacitance and high resistance.

2.2.1.1 Properties of the polyimide membrane

The capsule consists of two main parts; liquid dish and sealing stub, as shown in Figure 2.3b and Figure 2.3c, respectively. The PI membrane is enclosed into the liquid dish through a perfect sealing with the help of a polycarbonate film.

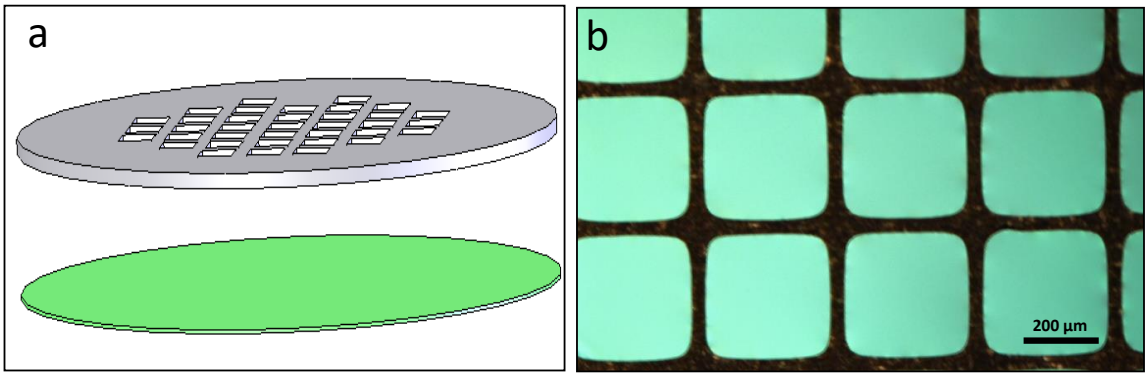

Figure 2.4 Schematic of the membrane structure and an optical image of the membrane. a. Schematic of the membrane structure: Gray; Nickel-polycarbonate protecting layer and green; PI membrane. b. Optical image of the membrane from bottom side: Black; Nickel-polycarbonate protecting layer, and green; PI membrane.

The membrane structure is made of 2 separate layers; one is nickel-polycarbonate and the other is approximately 150 nm thick PI membrane (gray and green in Figure 2.4a, black and green in Figure 2.4b, light gray and darker gray in Figure 2.5a, respectively). PI is protected with a Ni-polycarbonate layer (apprx. 300 µm thick) at the bottom of the liquid dish in order to avoid any pressure effect under high vacuum conditions of the SEM. The protecting layer consists of several grids (300 µm x 300 µm wide and 30 µm deep) which then enable free access to the PI membrane. The diameter of the entire membrane is 4 mm.

2.2.1.2 Nanopore fabrication

There are a few considerations which one should take into account in nanopore fabrication: First to mention, the membrane is designed for wet-SEM imaging; therefore the entire capsule

can be placed in the SEM holder. However it was found that using the sealing stub with the liquid dish in vacuum chamber causes an external pressure difference between the capsule inner side (atmospheric pressure) and the vacuum chamber of the FIB/SEM. Furthermore, ion-beam induced distruption of the surface tore apart the area of interest due to the stress impinged on the membrane. Compared to SiN membranes, the surface damage of PI upon the beam exposure is faster and can be related to lower tensile stress of PI membrane. Further experiments were, therefore, carried out by mounting the liquid dish on the sample holder using a sticky film, placed as shown in the inset in Figure 2.3b.

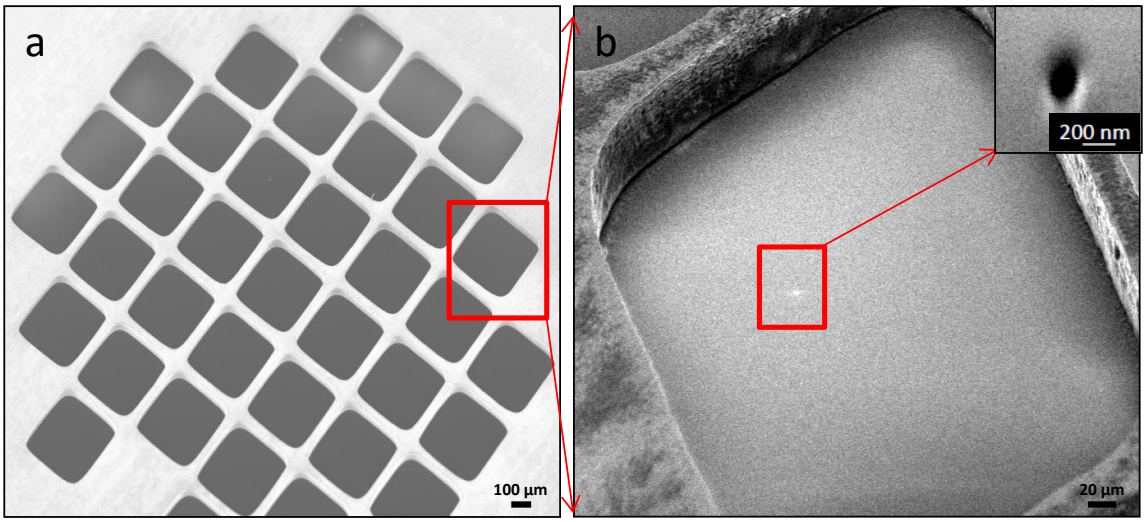

Figure 2.5 SEM images of the membrane and an individual nanopore. a. SEM image of the membrane surface: Light gray; Nickel-polycarbonate protecting layer and darker gray; PI membrane. The scale bar is 100 µm. b. SEM figure of an individual grid (inset: a nanopore drilled on the membrane, the scale bar is 200 nm). The scale bar is 20 µm.

Secondly it was noticed that insulating nature of the PI caused charging during imaging. The imaging difficulties on a transparent PI membrane used in Wet-SEM tissue imaging was also reported earlier, where a thin conductive carbon film (50 Å) was required on the inner side of the membrane, upon the application of low energy beam irradiation on the surface **(24)**. Conductive glue was, therefore, painted on the metal side of the capsule. Third, beam focus settings were performed on the metallic side of the capsule or on the grids due to the fact that polymer membrane was relatively more sensitive to the beam exposure and therefore damaged faster.

Another reason for working on the metal side was that the experimental working distance exceeds limits of SEM working distance when focus is performed on the membrane and the sample eventually damages the SEM gun.

To investigate the effect of ion beam dose in nanopore shaping, individual pore openings were fabricated on different spot sizes with 30 kV ion beam acceleration voltage and 1 pA beam current.

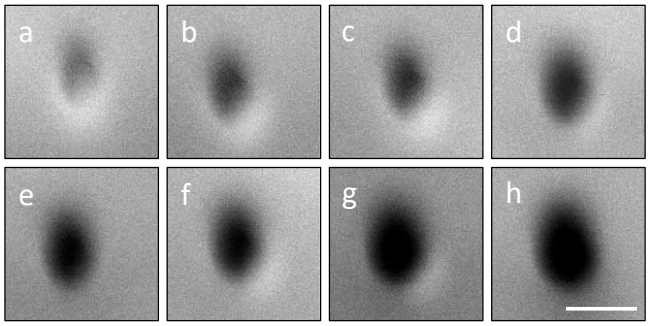

Figure 2.6 SEM images of individual pore openings. a. 2 seconds milling time (1.44 x 10^{21} C/m^2). b. 3 seconds milling time (2.16 x 10^{21} C/m^2). c. 4 seconds milling time (2.88 x 10^{21} C/m^2). d. 5 seconds milling time (3.16 x 10^{21} C/m^2). e. 6 seconds milling time (4.33 x 10^{21} C/m^2). f. 8 seconds milling time (5.77 x 10^{21} C/m^2). g. 10 seconds milling time (7.21 x 10^{21} C/m^2). h. 20 seconds milling time (1.44 x 10^{22} C/m^2). FIB beam parameters; 30 kV and 1 pA. The scale bar is 200 nm.

The milling time was varied from 1 second to 20 seconds corresponding to dose values ranging from 7.20 x 10^{20} C/m^2 to 8.29 x 10^{22} C/m^2, and the results are shown in Figure 2.6. A milling time of less than 5 seconds was observed to sculpt the surface, but not sufficient to complete the nanopore milling (i.e. 2, 3 and 4 seconds, as seen in Figure 2.6a, Figure 2.6b, Figure 2.6c, respectively). In contrast, a milling time of 5 seconds and above seemed to mill approximately 50 nm single nanopores in diameter (Figure 2.6d, and Figure 2.6e) while much larger nanopores (approximately 120 nm) were created within 20 seconds (Figure 2.6h). These results clearly show that the higher the ion beam dose, the larger the pore. However, milling time of 5–7 seconds was considered to be optimum to create pores under 100 nm in diameter.

2.2.2 Silicon nitride nanopores

To date, SiN has been of choice in many cases, because it is mechanically robust and chemically stable over a range of concentrations, pH and temperature. Furthermore, it can easily be modified chemically or physically to increase its functionality. Free-standing SiN nanopore membranes are generally supported on a micron thick <100> Si wafer (e.g L_{Si} = 300 µm) and individual nanopore chips are commonly 5 x 5 mm in size. The chip with the Si support provides good insulation between the nanopore chambers with high electrical and seal resistance.

2.2.2.1 Design considerations

For the development of a monolithic device which comprises a nanopore integrated into a microfluidic channel, SiN chips were designed to be 10 x 10 mm in our experiments.

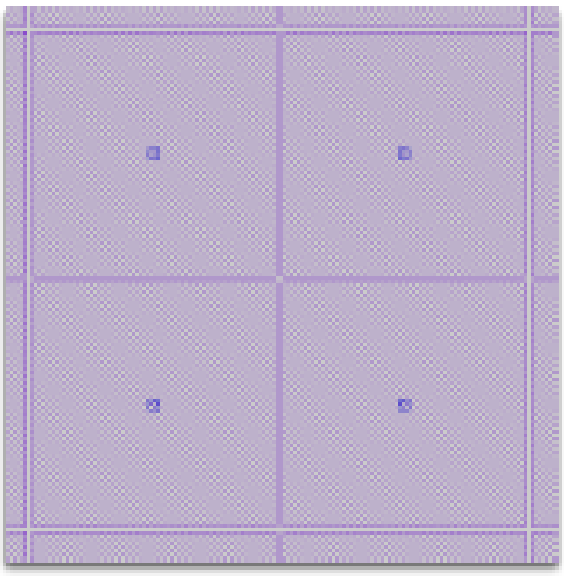

Figure 2.7 Snapshot of the chip design. Big square; individual chips, small squares in the centre; the initial feature size of SiN windows before etching. The spacing between each individual chip is 250 µm.

The spacing between each individual chip is typically 250 µm, as shown in Figure 2.7. Initial SiN window size of 444 x 444 µm results in 50 x 50 µm wide free standing SiN windows at the centre of each individual chip after KOH etch.

2.2.2.2 Device fabrication

Chip designs were drawn in a computer-aided design program; either AutoCad Civil 3D or KLayout drawing software, and transferred to a transparent acetate photomask or a chrome-on-glass photomask. Each mask design contains 54 individual chips. Acetate masks were used in the experiments presented in this chapter (fabricated by Micro Lithography Services Ltd, UK).

Semiconductor processing techniques are used to fabricate SiN nanopore devices. Fabrication procedure is outlined below and the workflow of the fabrication is shown in Figure 2.8;

- A thin layer of SiN (L_{SiN} = 100 nm) is deposited onto Si wafer from both sides by low pressure chemical vapor deposition (LPCVD) (Virginia Semiconductor Inc., USA/Active Business Company GmbH, Germany) (Step I, Figure 2.8).
- The wafer is cleaned with acetone and dried with N_2 prior to the process. O_2 plasma for about 5 min is also recommended to increase the surface cleanliness and to provide greater adhesion of the resist to the wafer surface.
- The wafer is then prebaked at 100 ºC for a few min.
- It is spin-coated at 4000 rpm for 60 s with AZ1512 HS photoresist (Clariant GmbH, Germany) which results in less than 2 μm thick uniformly distributed surface coverage.
- It is then soft baked at 115 ºC for 60 seconds.

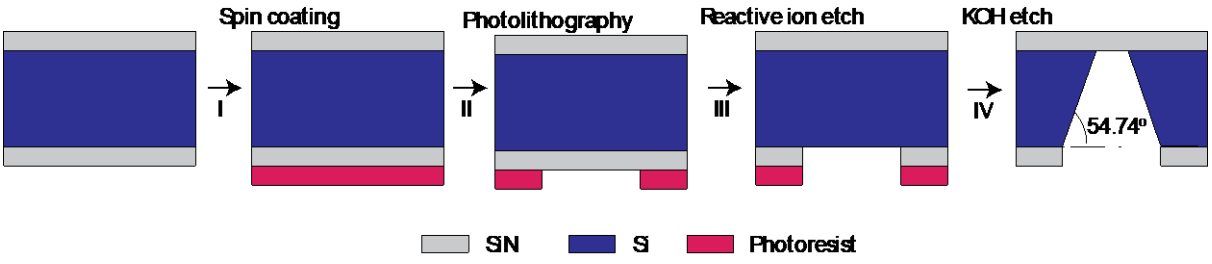

Figure 2.8 Workflow of the membrane. I. Spin-coating followed by photolithography. II. Resist development. III. Reactive ion etch of SiN. IV. KOH etch of Si at an angle of 54.74º. Overall process results in the creation of free-standing micron size SiN windows.

- The photomask is placed on the wafer and stabilised with a glass plate after which it is exposed to the monochromatic UV light from the glass side. The exposure energy is 80 mJ/cm^2.
- At the final stage of the photolithography, the resist is developed in 1:4 AZ400K developer (Clariant GmbH, Germany) for 30 seconds, rinsed with water and dried with N_2. Photolithography ends with micron scale SiN windows on millimeter scale chip patterns (Step II, Figure 2.8).
- Reactive ion etch (RIE) is carried out to remove SiN at the University of Surrey[20,21]. Conditions are set to be; 10 mTorr pressure, 100 watt RF power and 60 SCCM CF_4 gas flow rate for 3.5–4 min. Etch rate is 40-45 nm/min, stated by the manufacturer (Step III, Figure 2.8).
- 30% KOH solution is used to etch Si in a KOH bath at 80 ºC for about 5 hours **(25)**. KOH etch is generally isotropic; however the etching of Si with KOH solution is anisotropic and crystal orientation dependant. Because hydroxide ions remove Si atoms from <111> crystalline plane much slower (0.005 μm/min) than <100> plane (0.797 μm/min) **(26)**. As a result, Si substrate is etched with an angle of 54.74º. The reaction is shown as;

$$Si + 2\,OH^- + 2\,H_2O \xrightarrow{yields} SiO_2(OH)_2^{2-} + 2\,H_{2(g)} \qquad \text{Equation 2.2}$$

The etch rate was experimentally found to be 1.6 μm/min. Some of the wafers were etched longer than the required duration, in which the etch rate slowed down to 0.94 μm/min approximately. The difference in KOH etch from experiment to experiment might be due to temperature difference, the position of the wafer in the solution and the position of the container in the oil bath, thus insufficient agitation of the KOH solution. These factors led to the over-etching of some Si wafers and resulted in larger SiN

[20] Some of the RIE experiments are carried out by William Pitchwood and Dr. Kostis Michelakis University of Surrey.
[21] Details of RIE are discussed in CHAPTER 3.

window sizes than expected (up to 70 x 70 µm wide windows in some cases) (Step IV, Figure 2.8).

2.2.2.3 Nanopore fabrication

Unlike the capsule, Si membranes could be more easily loaded into the FIB since it is a planar device. Etched side of the chip was placed down on the disk so as to prevent the damage to the free-standing membrane.

FIB beam parameters were the same; 30 kV acceleration voltage and 1 pA beam current. Milling time of 6 seconds, corresponding to a dose of 2-5 x 10^{22} C/m^2, was sufficient to open pores varying from 20 nm to 60 nm. The variations are possibly a consequence of the day-to-day differences in beam conditions such as focus, alignment, and so on.

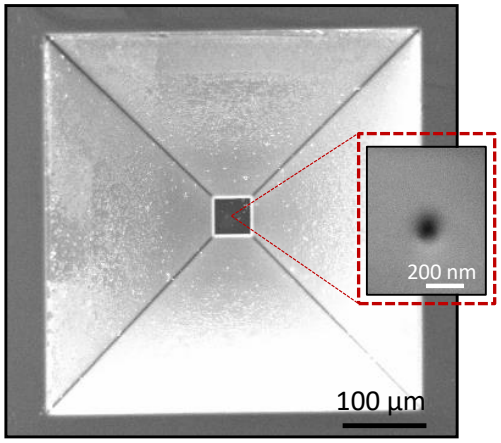

Figure 2.9 SEM image of a free-standing SiN windows (inset: a single nanopore drilled on the membrane). FIB parameters; 30 kV, 1 pA, $t_{milling}$ = 6 seconds. The scale bar is 100 µm and 200 nm, respectively.

2.3 Electrochemical characterization

2.3.1 Experimentation

2.3.1.1 Materials

KCl solution (VWR, UK) was prepared in 10 mM Tris.HCl and 1 mM EDTA buffer, pH = 8 (Sigma-Aldrich UK), autoclaved and filtered (Pall Corporation, UK, pore size: 200 nm).

Ag/AgCl electrodes were prepared by coating 0.25 mm Ag wire surface (GoodFellow, UK) with a solid thin layer of AgCl. Simply, Ag wire is chloridized in 2 M HCl (Chronopotentiometry, current: 0.01 mA, voltage: 6 V, and time: 900 s). Oxidation of Ag to Ag^+ at the electrode-solution interface (Equation 2.3) and the formation of AgCl on the Ag wire surface can be written as (Equation 2.4);

$$Ag_{(s)} \leftrightarrow Ag^+ + e^{-1} \qquad \text{Equation 2.3}$$

$$Ag^+ + CI^- \rightarrow AgCl_{(s)} \qquad \text{Equation 2.4}$$

The electrodes can be stored dry or in KCl solution in the dark.

2.3.1.2 Cell setup of the nanopore devices

Figure 2.10 shows a sketch of a typical nanopore platform. The SiN nanopore chip was sandwiched between two PDMS rings and placed between two cell chambers (generally made of PTFE or PEEK). Prior to the cell assembly, the chip was treated from both sides with O_2 plasma

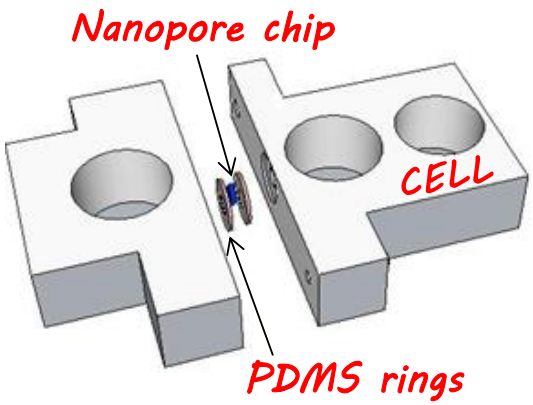

Figure 2.10 Sketch of commonly used nanopore cell assembly. The diameter of the PDMS ring is almost 0.35 cm and each chamber volume is about 1 ml.

for about 5 min in order to be able to improve the wetting quality of the chip and nanopore surface[22] and then dipped into ethanol and DI water subsequently. Once the cell was assembled

[22] This step also aids to remove potential air bubbles inside the nanopore.

with the chip, the cell compartments were filled with ethanol for at least 5 min, washed with DI water, and the electrolyte of interest couple of times subsequently.

As for the PI membrane, most of the membranes were pre-treated in IPA for about 15 min[23], washed with DI water, and the electrolyte of interest couple of times subsequently. The capsule was then dipped into a home-made PTFE cell filled with electrolyte, as illustrated in Figure 2.11. To increase the capsule inner volume (the liquid dish), which forms the cis side, and for easy handling of the membrane, a cylindrical plastic material was glued onto the polycarbonate side of the capsule.

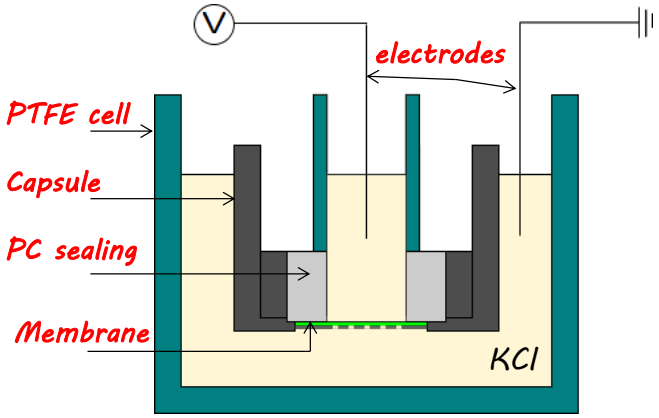

Figure 2.11 Schematic of the PI nanopore cell set-up.

2.3.1.3 Data acquisition and analysis

Preliminary ionic current measurements were performed using Gamry Reference 600 potenstiostat (Gamry Instruments USA) whereas the translocation experiments were carried out using a patch clamp amplifier (Axopatch 200B, Molecular Devices, USA). As for the recording, data was acquired using an electrophysiology data acquisition and analysis softwatre (pCLAMP^{tm}, Molecular Devices, USA), sampled at 50 kHz, filtered at 2-5 kHz using a 4-pole low pass Bessel filter, and digitized using an A/D convertor (Digidata® 1550 Data Acquisition

[23] The membrane is reported to be compatible with alcoholic chemical solvents such as methanol, ethanol, isopropanol (IPA), but not acetone and strong acidic chemicals like piranha solution and hydrogen peroxide.

System, Molecular Devices, USA). The sequential order of the data recording is illustrated in the schematic in Figure 2.12.

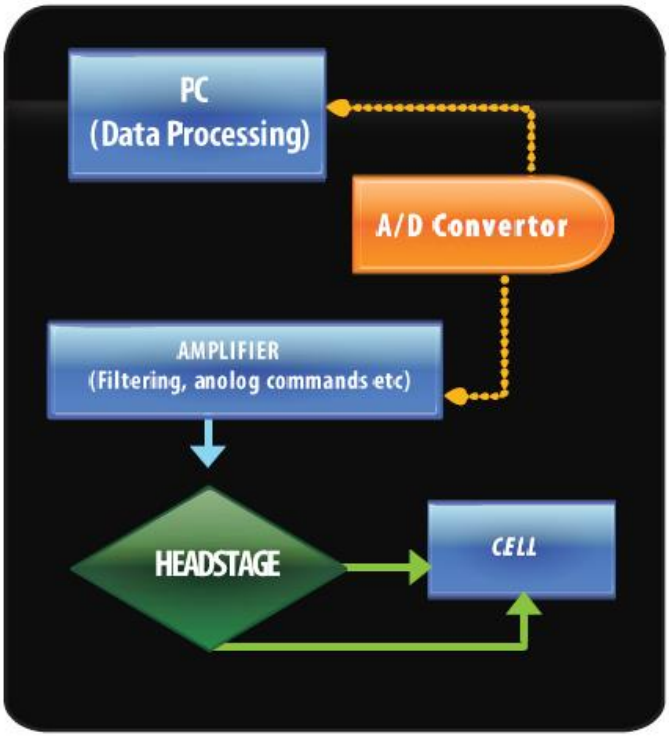

Figure 2.12 Sequential order of the data recording.

In order to detect single molecules using nanopore sensing, instrumentation able to detect low currents on the order of 10^{-12} A and fast transients is required. Axopatch 200B provides the lowest noise contribution at the market with a headstage attached, which the critical circuit component is cooled down to -15 ºC, minimizing noise as much as possible. The amplifier converts current to voltage signals, also known a current-to-voltage (I-V) converter, which can be controlled by either an oscilloscope or a computer program. The best way to measure the current is to use an operational amplifier that adjusts the voltage changes (IR) across a resistor automatically. However, this resistive-feedback circuitry is not ideal for highly sensitive current measurements. To achieve the required sensitivity, AxoPatch 200B utilizes a capacitor-feedback circuitry in which the current is measured as a function of voltage across a capacitor; basically the output voltage is the time integral of the input current. This low-noise capacitor-feedback headstage can operate like a voltage clamp, where the voltage is kept constant, but varied

independently of output current while recording current through a channel/pore or channels **(27)**. The membrane conductance (G_M) is mostly of interest to the users, but the only way to measure the conductance is to investigate the ionic current through the pore, which is proportional to G_M. The voltage clamp thus offers the opportunity to monitor any change in conductance **(28, 29)**.

Data analysis was performed using either Clampfit 10.2 (Molecular Devices, USA) or a Matlab code written by Dr. Joshua B. Edel. In Clampfit, threshold was defined with respect to the signal distribution. In a similar manner, but more rigorous way, Matlab code uses a peak finder algorithm that is assigned to find local maxima and minima of the experimental data and then to fit it with Poisson distribution. Baseline determination using Matlab code is illustrated in Figure 2.13.

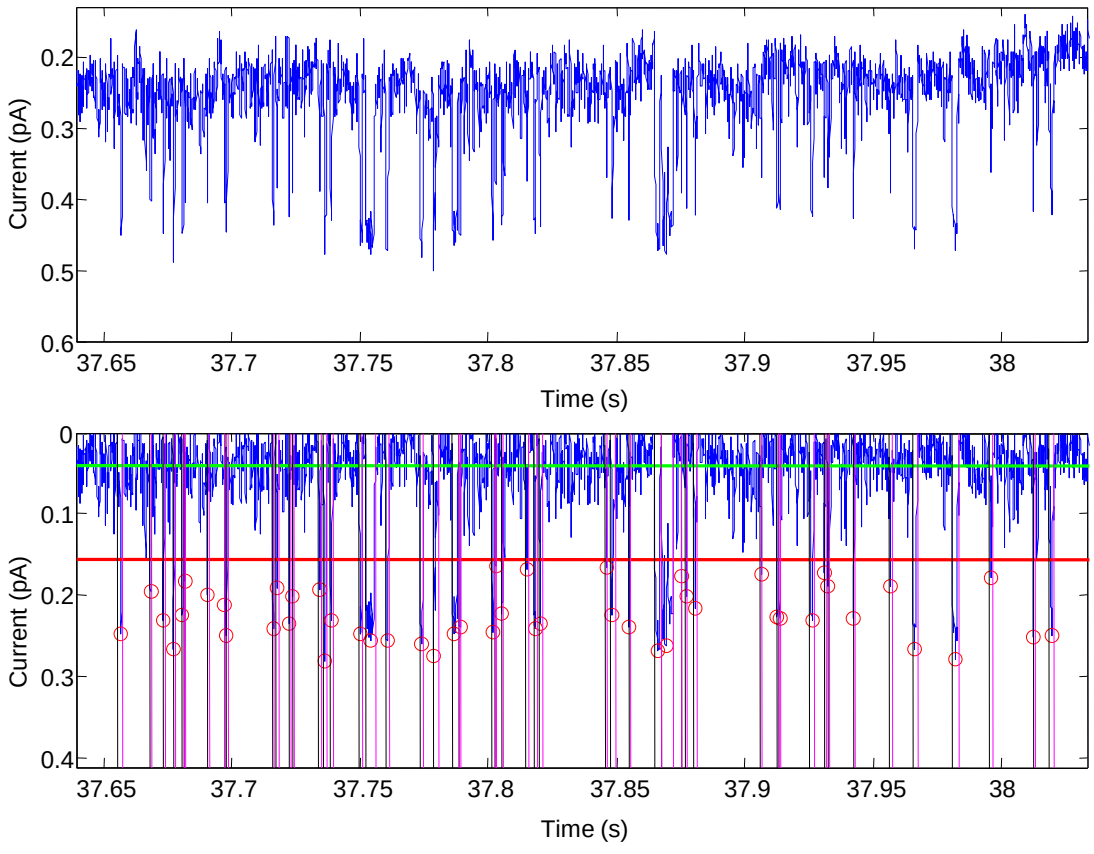

Figure 2.13 Example of a current trace that the background threshold is determined by fitting the experimental data to the Poisson distribution.

2.3.2 Electrochemical characterization

Nanopores were characterized by measuring the nanopore conductance, G, obtained from the slope of the ionic–current (I-V) curves, which were typically recorded within the range of ± 500 mV[24] (Ohm's Law);

$$G = \frac{I}{V} = \frac{1}{R} \qquad \text{Equation 2.5}$$

Due to the fact that the nanopore sizes used in the experiments were large, surface charge effects were neglected and the effective nanopore diameter was calculated from the simplified version of Equation 1.13, giving rise to Equation 2.6;

$$G = \pi \frac{d_{pore}^2}{4L_{pore}} \kappa \qquad \text{Equation 2.6}$$

I. Control experiments with the PI membrane were first performed with devices without nanopores in order to examine the sealing properties of the device and the capacitive current, I_{cap}. It was found that I_{cap} calculated from the I-V curve in Figure 2.14 (red) was 2.2±0.7 nF (18±0.1 nF/cm^2). It indicates the gigaohm resistance of the PI membrane between two compartments referring to non-porous membrane and that there is no leakage through the capsule parts. As for the comparison, I_{cap} of free-standing SiN membrane (50 x 50 μm windows size) was calculated and found to be 6.3±0.2 nF (0.3 mF/cm^2). It means that the PI capacitance is similar to that of SiN devices. G_{PI} was further investigated for the membranes treated under different milling durations. It was observed that a milling duration of 5 seconds did not produce the nanopore generally (black curve in Figure 2.14), however once the irradiated membrane was exposed to oxygen plasma for 5 min, a nanopore of approximately 100 nm in diameter (calculated from the slope of the green I-V curve in Figure 2.14) could be produced.

[24] Voltage range was generally chosen to be lower for PI nanopore devices (e.g. lower than ± 200 mV) as the mechanical stability of the nanopore was concerned.

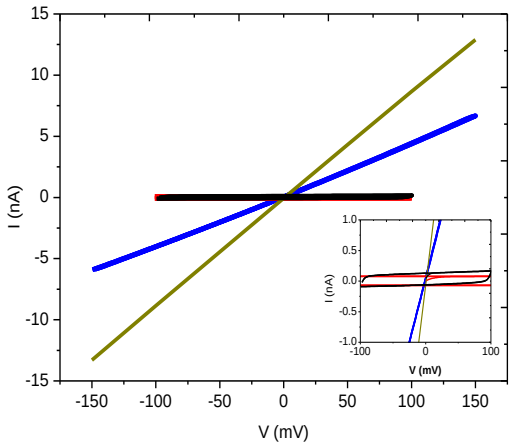

Figure 2.14 Cyclic voltammograms recorded using PI membranes. Red; without any treatment, black; 5 seconds milling of the membrane and IPA treatment prior to the experiment, green; 5 seconds milling and 5 min oxygen plasma treatment followed by IPA treatment, blue; 6 seconds milling of the membrane. (0.1 M KCl and V range is ± 0.1 and ±0.15 V).

The membrane was plasma-treated with the plasma for a certain period of time (2-9 min) and the change in the surface was monitored with an optical microscope. The result was that the surface was damaged gradually. Seemingly, the membrane surface was only sculpted with the ion beam irradiation when used a milling duration of about 5 seconds and below; however the nanopore was not created. With the assistance of the plasma, the sculpted feature was reshaped over time in a controllable manner, resulting in the production of a nanopore. It should also be noted that the overexposed membranes (i.e. 10 min) resulted in a permanent damage to the membrane. For the membranes milled for a duration of 6 seconds and longer, IPA treatment of the membrane for 15 min was sufficient to wet the surface, and led to a nanopore opening of 45 ± 33 nm in diameter (calculated from the blue I-V curve in Figure 2.14). An experimental observation was that the extensive exposure of the surface to the electron beam expands the nanopore diameter to 100 nm or above. This was related to the mechanical vulnerability of the PI membrane arising from its low tensile stress.

II. SiN nanopore size was generally in the range of 15–50 nm in diameter. Wide distribution of the nanopore size was related to the day-to-day differences in imaging process where the

milling conditions (e.g. focus, stigmation, beam alignment) might differ slightly and result in differences in beam intensity.

2.3.3 Noise performance of the nanopore devices

2.3.3.1 Dominant noise sources in nanopore experiments

Noise in nanopore devices can originate from a range of sources, including internal and external factors. A comprehensive review of the nanopore noise analysis can be found in the Axon-guide and a book chapter recently published by V. Tabard-Cossa **(30, 31)**. A brief summary of the most relevant noise sources in nanopore experiments is provided below;

There are mainly 4 types of noise sources occurring in nanopore-based detection **(30, 31)**;

- ***Thermal noise (also known as Johnson noise):*** It sets the noise floor in the absence of a voltage applied and is a sum of the resistance originating from feedback resistor and/or nanopore itself. It is generated by the random motion of the charge carriers in a conductor and nanopores with large resistance result in a lower thermal noise.

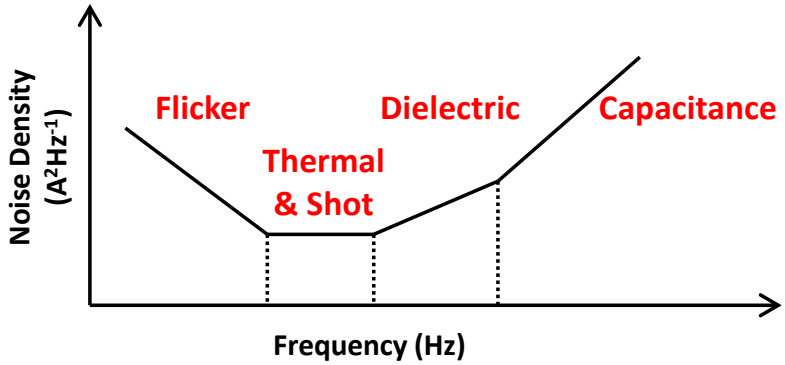

Figure 2.15 Dominant noise sources in PSD, modified from (32).

- ***Shot noise:*** It is a consequence of current flow across a potential barrier such as the noise arising from the input current in operational amplifier (headstage) or nanopore.

- ***High frequency noise:*** It is composed of dielectric noise and capacitance noise. It is primarily generated due to the high capacitance of the Si-based membrane and can only be avoided by advances in the membrane fabrication and also in the instrumentation.
- ***Flicker noise:*** It is a low frequency noise source and becomes pronounced with the applied voltage across the nanopore. Although the specific source of the flicker noise is not known, the nature of the charge carriers, their mobility through the pore wall, the electrostatic field effects and surface properties have been shown to play a role leading to flicker noise. Hence, the surface treatment of the membrane is generally important for the reduction of flicker noise **(33-37)**. These include atomic layer deposition, piranha treatment, and improved wetting properties of the surface and plasma treatment. A strong relationship between the salt concentration, pore diameter, the resistance of the pore and the flicker noise (e.g. a considerable reduction in low frequency noise with a high resistance value) has also been found **(38)**.

2.3.3.2 Investigating the nanopore noise

Nanopore noise was investigated by looking into the total root-mean-square, RMS, of the current signal. RMS noise is the square root of the average of the squared noise components and simply identical to the standard deviation of current signal. Any individual noise contribution to current or voltage can be evaluated by its power spectral density (PSD) obtained by converting a time-domain signal into its frequency components.

With the aim of understanding the noise level with PI nanopores, a PI nanopore with diameter of 14 nm was compared with a 19 nm wide SiN nanopore in diameter. An RMS of 36 pA for the PI nanopore was observed at a voltage of 0 mV whereas it was 48 pA for the SiN nanopore, as shown in Figure 2.16a. Once a voltage of 50 mV was applied, 100 times increase in the amplitude in the low frequency regime of the power spectrum (e.g. <100 kHz) was observed for the PI nanopore, compared to the SiN nanopore. This could be a potential consequence of the

greater current flow through the PI nanopore, which then affects the flicker and thermal noise of the system.

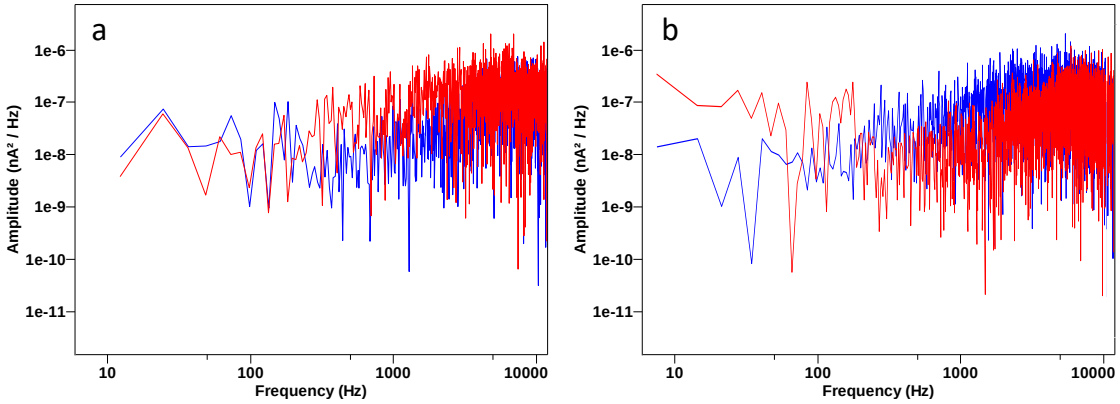

Figure 2.16 Power spectral densities of PI nanopore and SiN nanopore (red and blue, respectively). a. Recording at 0 mV. b. Recording at 50 mV. (1 M KCl, 10 mM Tris HCI and 1 mM EDTA, f_s = 50 kHz, f_f = 10 kHz).

A qualitative interpretation of PSD on the high frequency noise (e.g. 1-10 kHz) is that the PI membrane showed similar noise level to the SiN membrane, which agrees with the finding stated above where I_{cap} was of similar magnitude for both membranes. It is contradictory to the initial expectations that low capacitance of the PI membrane would have led to lower noise level, however it could be explained with the increase in the noise due to the mechanical structure of the membrane sealed with the nickel-polycarbonate layer.

2.3.4 Translocation of λ-DNA through PI nanopores

As a proof-of-principle, the capability of PI nanopores for biosensing was studied using a single PI nanopore with an experimental diameter of 17 nm, calculated from Equation 2.6. A control experiment was run in DNA-free solution by monitoring the current over time at -500 mV and a stable current trace was initially observed. Upon the addition of DNA (λ-DNA, 48.5 kbp dsDNA), translocation type events with an increase in nanopore conductance were observed, as shown in Figure 2.17a. ΔI with a mean amplitude of 130 pA and t_d with a mean of 13 ms corresponding to a speed of 0.12 cm/s (4 bp/μs) was found, as shown in Figure 2.17b[25].

[25] Cut-off in signal distribution is due to the noise rejection in data acquisition.

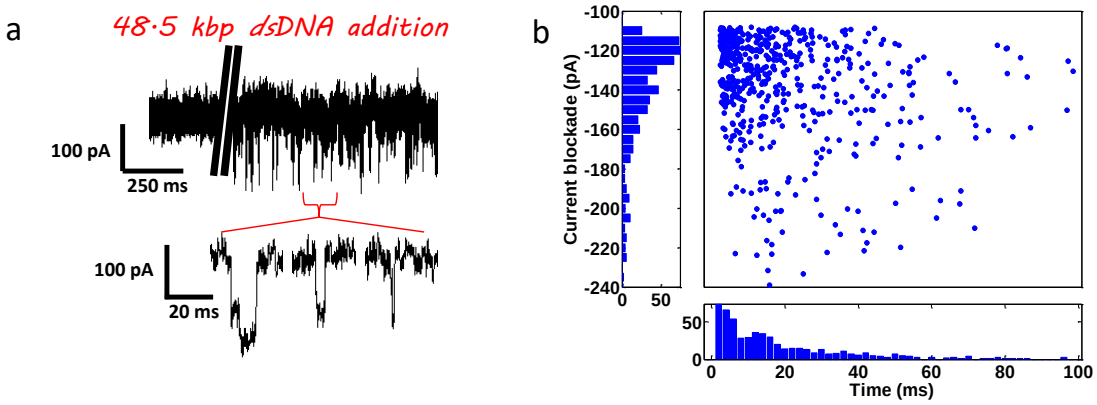

Figure 2.17 Translocation events of λ-DNA through 17 nm PI nanopore. a. Current-time trace before and after the addition of DNA and individual translocation events obtained from the trace. b. Scatter plot, and ΔI and t_d histograms of the translocation events. (0.1 M KCl, 10 mM Tris HCI and 1 mM EDTA, V_{bias} = -500mV, f_s = 50 kHz, f_f = 2 kHz).

The translocation speed is slower than the ones reported in literature for pores larger than 10 nm **(39-41)**. For example, Chen *et al* showed that translocation speed of 48.5 kbp is 3 cm/s through a 15 nm SiN membrane coated with Al_2O_3 (V = 500 mV). It is also similar to the speed values reported for the experiments conducted to slow down the high speed of the molecule to 0.1 cm/s, which is a challenging task through silicon based nanopores **(42)**. Slower translocation might be due to the stronger interactions between the biomolecule and the polymer membrane walls during translocation. In regards to the conductance increase, it has been reported that an enhancement in G is expected when worked at low salt concentrations (e.g. $C_{KCl} < 0.1$ M) due to the dominant surface charge effects **(43)**. The cross-over concentration is potentially dependant on the surface properties of the material used and is expected to be different for PI nanopores. Further work is therefore required to establish the salt effects on PI nanopores.

2.4 Conclusion

To summarize, we have fabricated individual pores in the nanometre ranges using two different membrane materials. The first one is a commercially available, approximately 150 nm thick polyimide membrane. The membrane does not require any semiconductor processing techniques as opposed to most of the membrane materials that have been used previously in nanopore research. Furthermore, compared to current track-etched polymer nanopores, a direct

and easy way of fabricating single polymer nanopores of less than 100 nm in diameter was shown to be possible using FIB milling. Subsequently, these pores were characterized electrochemically. Finally, DNA translocation was shown. It was found that the capsule is single-use, as the quality of the electrochemical signal deteriorated after multiple use. Although the PI nanopore platform can be considered as an alternative to other solid-state nanopore membrane materials, potential difficulties to integrate with any other platforms for a compact biosensing device make it a challenge.

Further experiments were thus carried out with devices comprising SiN membranes, as shown in the following chapters. In this chapter, the fabrication of SiN membranes and nanopores has also been illustrated. The use of SiN membrane provides the fabrication of a planar composite sensing device, which may be embedded into microfluidic channels.

References

1. Miles BN, Ivanov AP, Wilson KA, Dogan F, Japrung D, Edel JB. Single Molecule Sensing with Solid-State Nanopores: Novel Materials, Methods, and Applications. Chemical Society Reviews. 2012.

2. Cai Q, Ledden B, Krueger E, Golovchenko JA, Li J. Nanopore Sculpting with Noble Gas Ions. Journal of Applied Physics. 2006;100(2).

3. Schiedt B, Auvray L, Bacri L, Oukhaled G, Madouri A, Bourhis E, et al. Direct Fib Fabrication and Integration of "Single Nanopore Devices" for the Manipulation of Macromolecules. Microelectron Eng. 2010;87(5-8):1300-3.

4. Gierak J, Madouri A, Biance AL, Bourhis E, Patriarche G, Ulysse C, et al. Sub-5 Nm Fib Direct Patterning of Nanodevices. Microelectron Eng. 2007;84(5–8):779-83.

5. Yang JJ, Ferranti DC, Stern LA, Sanford CA, Huang J, Ren Z, et al. Rapid and Precise Scanning Helium Ion Microscope Milling of Solid-State Nanopores for Biomolecule Detection. Nanotechnology. 2011;22(28).

6. Kuan AT, Golovchenko JA. Nanometer-Thin Solid-State Nanopores by Cold Ion Beam Sculpting. Applied Physics Letters. 2012;100(21):213104.

7. James T, Kalinin YV, Chan C-C, Randhawa JS, Gaevski M, Gracias DH. Voltage-Gated Ion Transport through Semiconducting Conical Nanopores Formed by Metal Nanoparticle-Assisted Plasma Etching. Nano Letters. 2012;12(7):3437-42.

8. Kim H-M. Theoretical and Experimental Study of Nanopore Drilling by a Focused Electron Beam in Transmission Electron Microscopy. Nanotechnology. 2011;22(27):275303.

9. Storm AJ, Chen JH, Ling XS, Zandbergen HW, Dekker C. Fabrication of Solid-State Nanopores with Single-Nanometre Precision. Nat Mater. 2003;2(8):537-40.

10. Chang H, Iqbal SM, Stach EA, King AH, Zaluzec NJ, Bashir R. Fabrication and Characterization of Solid-State Nanopores Using a Field Emission Scanning Electron Microscope. Applied Physics Letters. 2006;88(10).

11. Zhang WM, Wang YG, Li J, Xue JM, Ji H, Ouyang Q, et al. Controllable Shrinking and Shaping of Silicon Nitride Nanopores under Electron Irradiation. Applied Physics Letters. 2007;90(16).

12. S Prabhu A. Sem-Induced Shrinking of Solid-State Nanopores for Single Molecule Detection. Nanotechnology. 2011;22(42):425302.

13. Li J, Stein D, McMullan C, Branton D, Aziz MJ, Golovchenko JA. Ion-Beam Sculpting at Nanometre Length Scales. Nature. 2001;412(6843):166-9.

14. Chih Jen Lo TA, Alexey Bezryadin. Fabrication of Symmetric Sub-5 Nm Nanopores Using Focused Ion and Electron Beams. Nanotechnology. 2006:3264–7.

15. Schenkel T, Radmilovic V, Stach EA, Park SJ, Persaud A. Formation of a Few Nanometer Wide Holes in Membranes with a Dual Beam Focused Ion Beam System. J Vac Sci Technol B. 2003;21(6):2720-3.

16. Ivanov AP, Instuli E, McGilvery CM, Baldwin G, McComb DW, Albrecht T, et al. DNA Tunneling Detector Embedded in a Nanopore. Nano Letters. 2011;11(1):279-85.

17. Siwy Z, Dobrev D, Neumann R, Trautmann C, Voss K. Electro-Responsive Asymmetric Nanopores in Polyimide with Stable Ion-Current Signal. Applied Physics a-Materials Science & Processing. 2003;76(5):781-5.

18. Heins EA, Siwy ZS, Baker LA, Martin CR. Detecting Single Porphyrin Molecules in a Conically Shaped Synthetic Nanopore. Nano Letters. 2005;5(9):1824-9.

19. Apel PY, Korchev YE, Siwy Z, Spohr R, Yoshida M. Diode-Like Single-Ion Track Membrane Prepared by Electro-Stopping. Nuclear Instruments and Methods in Physics Research Section B: Beam Interactions with Materials and Atoms. 2001;184(3):337-46.

20. Schiedt B, Healy K, Morrison AP, Neumann R, Siwy Z. Transport of Ions and Biomolecules through Single Asymmetric Nanopores in Polymer Films. Nuclear Instruments and Methods in Physics Research Section B: Beam Interactions with Materials and Atoms. 2005;236(1–4):109-16.

21. Harrell CC, Choi Y, Horne LP, Baker LA, Siwy ZS, Martin CR. Resistive-Pulse DNA Detection with a Conical Nanopore Sensor. Langmuir. 2006;22(25):10837-43.

22. Zuzanna Siwy DDD, Reinhard Neumann, Christina Trautmann, Kai Voss, inventor; Gesellschaft fuer Schwerionenforschung mbH (Darmstadt, DE), assignee. Method of Producing Nanostructures in Membrances, and Asymmetrical Membrane patent EP1338329. 2003.

23. Thiberge S, Nechushtan A, Sprinzak D, Gileadi O, Behar V, Zik O, et al. Scanning Electron Microscopy of Cells and Tissues under Fully Hydrated Conditions. Proceedings of the National Academy of Sciences of the United States of America. 2004;101(10):3346-51.

24. **Thiberge S, Zik O, Moses E**. An Apparatus for Imaging Liquids, Cells, and Other Wet Samples in the Scanning Electron Microscopy. Review of Scientific Instruments. 2004;75(7):2280-9.

25. **University BY**. Koh Etching [27.11.2013]. Available from: http://www.cleanroom.byu.edu/KOH.phtml.

26. Library VT. Wet-Chemical Etching and Cleaning of Silicon [29.11.2013]. Available from: http://www.virginiasemi.com/.

27. James V. Halliwell TDP, John Robins and, Standen NB. Voltage-Clamp Techniques. In: D O, editor. Microelectrode Techniques. Cambridge: The Company of Biologists; 1994. p. 17-35.

28. **Sarkman B, Neher E**. Single -Channel Recording. 2. ed. Sarkman B, Neher E, editors. New York: Plenum Press; 1995.

29. The Axopatch 200b User Guide [Internet].

30. Molecular Devices IMAT. The Axon Guide (Aguide to Electrophysiology & Biophysics Laboratory Techniques). 3. ed. California: MDS Analytical Technologies; 2008.

31. Tabard-Cossa V, editor Instrumentation for Low-Noise High-Bandwidth Nanopore Recording2013: Elsevier Inc.

32. Rosenstein JK, Wanunu M, Merchant CA, Drndic M, Shepard KL. Integrated Nanopore Sensing Platform with Sub-Microsecond Temporal Resolution. Nat Meth. 2012;9(5):487-92.

33. Tabard-Cossa V, Trivedi D, Wiggin M, Jetha NN, Marziali A. Noise Analysis and Reduction in Solid-State Nanopores. Nanotechnology. 2007;18(30).

34. Chen P, Mitsui T, Farmer DB, Golovchenko J, Gordon RG, Branton D. Atomic Layer Deposition to Fine-Tune the Surface Properties and Diameters of Fabricated Nanopores. Nano Letters. 2004;4(7):1333-7.

35. Smeets RMM, Keyser UF, Wu MY, Dekker NH, Dekker C. Nanobubbles in Solid-State Nanopores. Physical Review Letters. 2006;97(Copyright (C) 2010 The American Physical Society):088101.

36. Beamish E, Kwok H, Tabard-Cossa V, Godin M. Precise Control of the Size and Noise of Solid-State Nanopores Using High Electric Fields. Nanotechnology. 2012;23(Copyright (C) 2013 U.S. National Library of Medicine.):405301.

37. Venkatesan BM, Dorvel B, Yemenicioglu S, Watkins N, Petrov I, Bashir R. Highly Sensitive, Mechanically Stable Nanopore Sensors for DNA Analysis. Adv Mater. 2009;21(27):2771-+.

38. Smeets RMM, Keyser UF, Dekker NH, Dekker C. Noise in Solid-State Nanopores. Proceedings of the National Academy of Sciences of the United States of America. 2008;105(2):417-21.

39. **Chen P, Gu J, Brandin E, Kim Y, Wang Q, Branton D**. Probing Single DNA Molecule Transport Using Fabricated Nanopores. Nano Letters. 2004;4(11):2293-8.

40. Storm AJ, Storm C, Chen J, Zandbergen H, Joanny J-F, Dekker C. Fast DNA Translocation through a Solid-State Nanopore. Nano Letters. 2005;5(7):1193-7.

41. Ayub M, Ivanov A, Instuli E, Cecchini M, Chansin G, McGilvery C, et al. Nanopore/Electrode Structures for Single-Molecule Biosensing. Electrochimica Acta. 2010;55(27):8237-43.

42. Fologea D, Uplinger J, Thomas B, McNabb DS, Li J. Slowing DNA Translocation in a Solid-State Nanopore. Nano Letters. 2005;5(9):1734-7.

43. Smeets RMM, Keyser UF, Krapf D, Wu M-Y, Dekker NH, Dekker C. Salt Dependence of Ion Transport and DNA Translocation through Solid-State Nanopores. Nano Letters. 2005;6(1):89-95.

CHAPTER 3
Fabrication of Ultra Thin Nanopore Membranes

With advance in solid-state nanopore technology, the nanopore community has seen many improvements in both the device performance and the sensing ability of the device. This chapter focuses on the improved device performance by showing an alternative approach to fabricate ultra-thin nanopore membrane devices; Reactive Ion Etch. First how the fabrication procedure and chip design have been planned is discussed, secondly the fabrication and the optimization of the conditions are noted. The chapter ends with nanopore milling and DNA translocation through thinned membranes.

Detection ability of a solid-state nanopore device is mainly limited by its geometry (e.g diameter and membrane thickness) and surface properties as well as mechanical properties of the nanopore membrane. Although there has been numerous research on how nanopores with a diameter of comparable scale to the biomolecule cross-section can be fabricated, as well as how the nanopore surface can be modified, there is a limit to what can be done for the membrane thickness. Unlike its biological counterparts (5-6 nm), thinner membranes of engineered nanopores are difficult to work with because they are more prone to breakage during experimentation. Moreover, recalling Equation 1.14 and Equation 1.15, there is an inverse relationship between ΔI and the nanopore thickness, which means that using a thin nanopore membrane enhances the SNR. For example, translocation of dsDNA through a 100 nm thick nanopore causes current blockade amplitude of approximately 400 pA at 250 mV whereas it corresponds to 4 nA for a 10 nm thick pore.

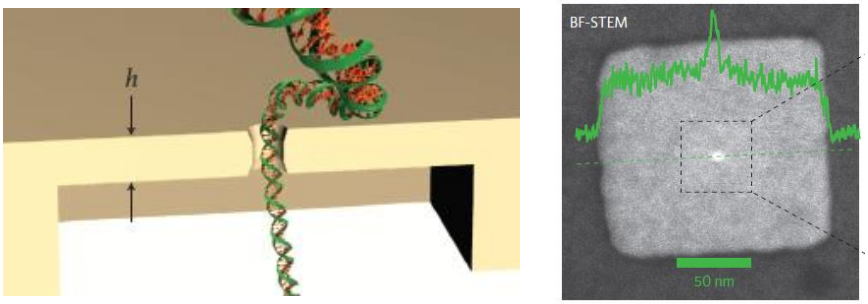

Figure 3.1 Left: Scheme of the DNA translocation through locally thinned membranes, Right: Bright-field Scanning Transmission Electron Microscopy image of the membrane (dark gray; the membrane, light gray; the locally thinned region). Initial membrane thickness is 41 nm and thinned region is 7 nm. Adapted from (1).

The use of a multi-layer graphene layer was an intriguing approach to the issue, published independently by several prominent research groups in the field **(2-4)**. As the graphene layer is mounted on a micron size pore followed by nanopore milling on the graphene, one can easily utilize it for nanopore biosensing applications, whether it be for sizing or sequencing. Another alternative approach has been reported by Wanunu *et al* where a top-down approach to locally thin the commonly used engineered nanopores was shown using Electron Beam Lithography

(EBL) **(1)**. Since only a small fraction of the membrane was thinned (as thin as 6 nm), the issue of handling was thus overcome.

Inspired by the work above, we fabricated locally thinned membranes by the direct application of reactive ion etch (RIE) as opposed to EBL. Although EBL also utilizes the RIE methodology and enables maskless lithography, our method eliminates the need to access EBL facilities that require e-beam writing systems and offers the opportunity to locally thin the membrane using conventional methods like soft lithography, which every nanopore user can easily practise. The concept is also analogous to the published work; there are several differences in fabrication steps that one might find preferable. It is believed that the procedure given below is also essential in terms of drawing a guideline of gradual SiN etching by RIE in nanoscales smaller than 30 nm.

The following sections first describe the principles of RIE, the design considerations, and the workflow of the fabrication. Secondly, the determination of critical conditions, the optimization and characterization steps are presented. The final section of the chapter addresses the optimized nanopore fabrication procedure, the electrochemical characterization of the chip, and an illustration of DNA translocation.

3.1 Fabrication strategy

Reactive ion etching is one of the dry etching methods that use ions, photons, electrons and radicals to remove the material of interest by knocking out atoms from the surface. The dissociation of the gases is a physical phenomenon while the attack of the products on the substrate is a chemical process. With the combination of both, RIE achieves highly resolved etched structures; either isotropic or anisotropic **(5)**. The substrate is placed in a vacuum chamber which consists of electrodes at the bottom and the top. Once gases are introduced and the plasma is ignited under vacuum by a strong RF electromagnetic field, the dissociation of the gases into chemically active ions and fragments occurs. Ions are accelerated towards the substrate surface due to the different charge distribution of the species in the chamber under the electric field. This

results in the chemical bombardment of the substrate surface after which the atoms are etched away from the exposed surface (unmasked lithographic patterns) and forms volatile products. By-products leave the chamber through an outlet at the bottom of the vacuum chamber.

RIE is an advanced technology in the field of micromachining which can produce high-aspect ratio patterns with high uniformity by simply choosing the right conditions. RF power, pressure (P), temperature (T), gas type and flow rate are the critical parameters that can be changed. In general, RIE uses halogen-based gases (e.g. SF_6, CF_4, CI_2). If the ions are too aggressive to the substrate, H_2, O_2 or Ar can be used either to manipulate the etch rate or to increase the etch selectivity for a specific material **(6)**. In particular, fluorine chemistry is used for SiN etch **(7)**.

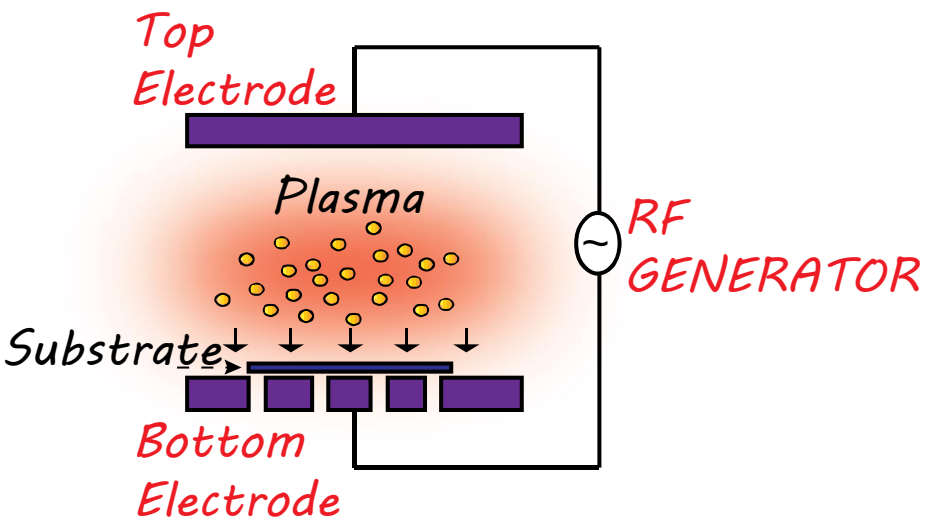

Figure 3.2 Schematic of the RIE process inside the vacuum chamber.

Carbon tetrafluoride (CF_4) was used as a source of plasma in the experiment presented in this chapter, because its etching rate is known to be relatively slower compared to another fluorine-based gas, SF_6 **(8, 9)**. Plasma converts CF_4 into fluorinated fragments and the fluorine atoms react with the SiN by forming volatile SiF_4, N_2 and other fluorine gases. The possible chemical reaction is shown as **(10)**;

$$CF_x + SiN \rightarrow SiF_4 + N_2, F_2, CFN \qquad \text{Equation 3.1}$$

Under specific conditions (60 SCCM CF_4 gas flow, 100 W RF power, 60 mT vacuum pressure), the etch rate of SiN is reported to be 35-45 nm/min by the manufacturer. As the aim was the gradual etch of etch SiN with high accuracy, the flow rate of CF_4 gas was lowered to a level of 10 SCCM. Additionally, Ar gas (50 SCCM) was introduced to the main gas stream as a diluent to further slow down the etch rate. Thirdly, vacuum pressure was reduced since the gas species become less aggressive with reduced pressure. Lastly, RF Power was lowered to 25-35 W.

3.2 Fabrication of locally thinned membranes

3.2.1 Design considerations

Fabrication requires two photomasks; back and front masks. The front side mask contains a square of 5 x 5 µm for an individual chip[26]. Regarding the back side mask; this is similar to the previous SiN nanopore chip design explained in CHAPTER 2. However the initial SiN windows were designed to be 430 x 430 µm (resulting in 20 x 20 µm free-standing SiN windows) because this presumably provides better mechanical stability. The spacing between the chips was also removed, because the KOH would start etching the Si from both sides and break apart the wafers to pieces at the early stage of wet etching.

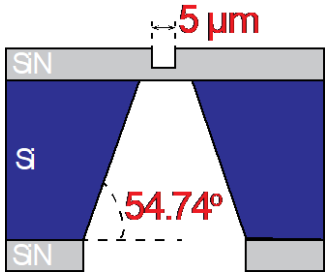

Figure 3.3 Sketch of the final shape of the locally thinned nanopore devices.

The alignment markers were modified from an initial design drawn by Dr. Joshua B. Edel and processed by Nanofabrication Centre, University of Minnesota, USA. The markers are placed

[26] The printed shape of the feature was, however, found to be slightly distorted due to the resolution limitations on image transferring process of the mask manufacturer.

at the right and left side of the wafer, both of which are 37 mm away from the centre. Figure 3.4 shows the back and the front side markers aligned to each other (purple and black, respectively). In the back side mask, the size of the big and small squares are 289 x 289 µm and 95 x 95 µm, the smallest feature size is 15 x 5 µm. In the front side mask, the smallest feature size is the same

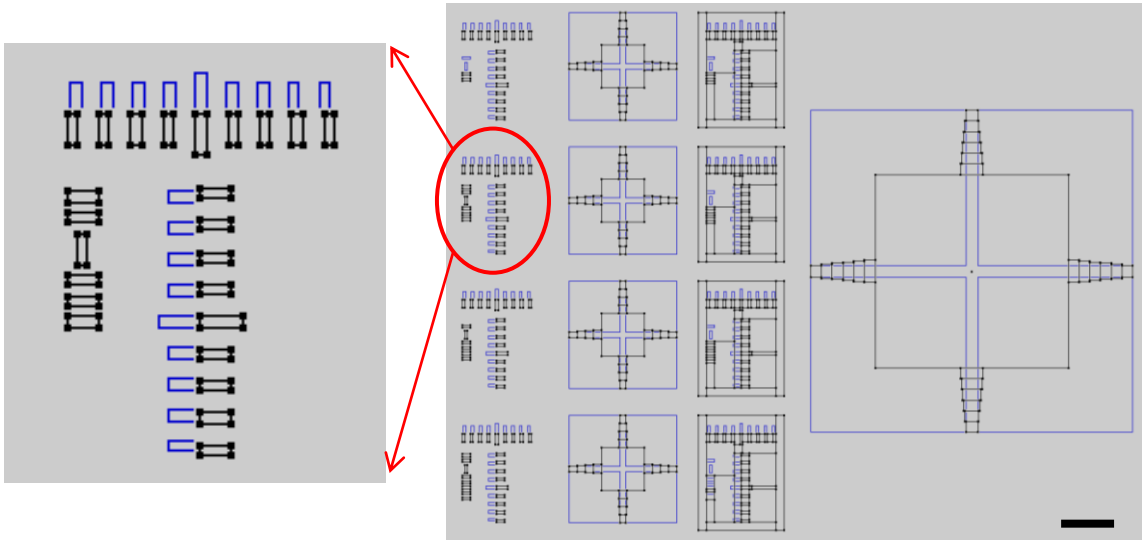

Figure 3.4 Snapshots of the marker designs. The scale bar is 95 µm.

and the biggest square is 360 x 360 µm, which provides a field of view large enough to position the back side markers during infrared illumination (IR). As Si is transparent in the IR regime of the spectrum due to its atomic bonding properties, IR illumination can be used to view bask side features on the wafer through the Si and enables the alignment of different features on both sides of the wafer. Initially the large features in the front mask are positioned and located onto the large features in the back mask through the positioned front features. Subsequently, the finer alignment is achieved through the alignment of small features. As highlighted in red in Figure 3.4, the alignment shifts 0.5 µm for each right and left small feature, which is aimed to provide higher alignment accuracy.

The chip designs containing individual chip sizes of 10 mm x 10 mm and 5 mm x 5 mm were drawn using KLayout and transferred to 5 inch chrome photomasks (low reflective chrome on standard spec soda lime glass) by JD Photo-Tools, UK. Each photomask was produced with different polarity (view from chrome-side and view from glass-side). The back side mask was

printed at a resolution of 64 000 dpi whereas the front side mask was printed at 128 000 dpi resolution, referred to super-high resolution.

3.2.2 Device fabrication

Resist development, back side alignment and Dektak profiling were carried out in London Centre for Nanotechnology (LCN) while RIE was carried out at the University of Surrey.

The fabrication procedure consists of two lithography and RIE steps[27], as stated below;

- The wafer is rinsed with acetone and DI water and placed in an oven at 200 ºC for 20 min to dehydrate. It is cleansed with N_2 afterwards.
- Hexamethyldisilazane (HDMS) is first spin-coated to promote the adhesion of the resist. Spin coating parameters; ramping up to 1000 rpm and then 4000 rpm for 0.5 seconds each, held at this speed for 30 seconds.
- Secondly S1818 photoresist is spin-coated with the same spinning conditions.
- The wafer is then placed on a hot plate at 115 ºC for 60 seconds to evaporate the excessive resist solvent (Step I, Figure 3.5).
- The wafer is placed on the mask aligner (Quintel Q4000-6 Mask Aligner) and cleaned with N_2. Pressure contact mode and UV mode are selected on the software. Subsequently, the right and left side markers are aligned so that the pattern design on the wafer is centred. If it is not aligned properly, one may encounter problems during the back side alignment because of the off-centre position of the feature. The wafer chuck has 6 mm flexibility of rotation and X-Y movements once in contact with the mask, however still separated by tens of microns. Alignment is monitored from a TV monitor and once completed, the pressure contact mode is selected. With pressure contact mode, 2 μm resolution and above can be achieved. For lower feature sizes, one can select vacuum contact mode, however this can disrupt the resist layer.

[27] Experimental observations and the reasons for several additional steps are given in the following sections.

- The wafer is exposed to UV light with a total exposure energy of 70 mJ/cm^2 (UV wavelength; 365 nm).
- Development is performed using Shipley's CD-26 developer for 60 seconds (Step II, Figure 3.5).
- The wafer is then hard baked at 115 ºC for 60 seconds.

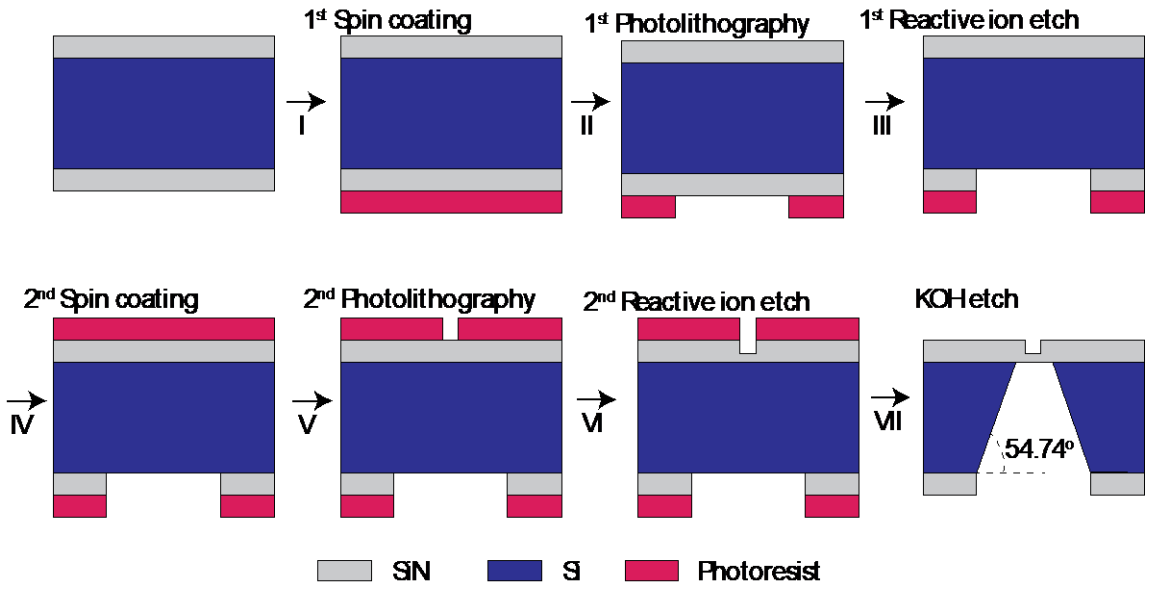

Figure 3.5 Schematic of the fabrication workflow. I. Spin coating the photoresist. II. Photolithography and resist development. III. Back side SiN is completely etched by RIE (Experiment conditions; 60 SCCM CF_4 gas flow, 100 W RF power, 60 mT vacuum pressure). IV. Second spin coating for the front side followed by back side alignment. V. Second photolithography for the front side of the wafer. VI. Second RIE for the gradual removal of SiN at the front side. VII. KOH etch.

- The back side features are etched before the back side alignment so that IR illumination is enabled. RIE conditions are; 60 SCCM CF_4 gas flow, 100 W RF power, 60 mT vacuum pressure[28] (Step III, Figure 3.5).
- Second photolithography is carried out on the back side of the wafer for the back side alignment. The same photolithography procedure as described above is followed (Step IV and step V, Figure 3.5).

[28] This experiment was carried out by William Pitchford and Dr. Kostis Michelakis.

- After the alignment of the mask and the wafer by optical imaging, IR illumination is selected. Back side alignment is achieved through the coarse alignment of big features and the subsequent alignment of small features. The resolution limit is around 5 μm where it matches the smallest feature size in the chip design.
- The resist is developed as described above (Step V, Figure 3.5).
- The low energy O_2 plasma treatment is applied prior to the second RIE; 30 W plasma power for 15 seconds.
- The RIE sample chamber is first cleaned by the flow of 50 SCCM O_2 gas at 60 mT chamber pressure, 100 W RF power for 5 min and subsequently by the flow of etchant gases for 30 min, where Ar dilution of the etchant gases is applied (10 SCCM CF_4 and 50 SCMM Ar gas flow, 100 mTorr vacuum pressure, 25 to 35 W RF power).
- Initial test experiments are run using individual plain SiN chips and the etch rate is defined by the change in SiN thickness using ellipsometer. RIE is performed on the sample using the diluted gas flow accordingly (Step VI, Figure 3.5).
- The wafer is dipped into 30% KOH at 80 ºC for more than 5 hour, resulting in free-standing locally thinned SiN windows (Step VII, Figure 3.5) **(11)**.

3.3 Etch characterization

Etch rate was investigated using different experimental methods. These include Dektak profiling (LCN), ellipsometer (University of Surrey) and Atomic Force microscopy. The quality of etching was also confirmed with SEM (LCN).

3.3.1 Determining the etching rate

Although the etch rate of SiN is defined by the manufacturer, it is highly recommended that the etch rate for each specific experiment is pre-examined; because RIE chamber conditions might be slightly different due to changes in laboratory environments as well as the geometrical and qualitative differences of the tested material. Therefore, two sets of preliminary experiments were carried out using ten different SiN wafers (L_{SiN} = 80 nm, feature size of 430 x 430 μm for

each individual chip) in order to determine the optimal window for etch duration within the range of 2.30-10 min (Step III, Figure 3.5). Initial settings were; 10 SCCM CF_4 and 50 SCMM Ar gas flow, 100 mTorr vacuum pressure, 25 W RF power.

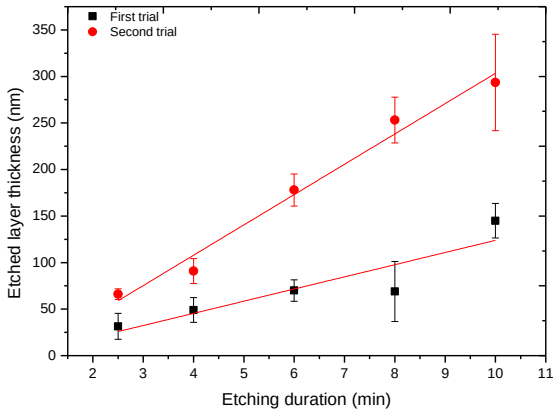

Figure 3.6 Dektak surface profiling results of the etch. Etch parameters: 10 SCCM CF_4 and 50 SCMM Ar gas flow, 100 mTorr vacuum pressure, 25 W RF power. Initial SiN thickness; ~ 80 nm. Error bars represent the standard deviation of the mean, which was calculated from at least 3 different measurements on each wafer.

After RIE, the wafers were washed in acetone in order to remove the resist and dried prior to the surface profiling experiments using Dektak Surface Profiler. The etch depth is plotted against the etch duration in Figure 3.6. For two of the trials, a linear change in the etch depth was observed with an increase in the etch duration. However, the slopes for the curves were different, indicating a faster etch rate in the second trial. The average etching rate was 11.9±2.1 nm/min for the first set of experiments whereas it rose up to 28.0±3.5 nm/min for the second trial. It is conceivable to think that the gas flow and the chamber conditions became more stabilized over time, hence more aggressive. Another observation is that the etch depth is much larger than the thickness of the SiN for the etch duration of more than 4 min. The reason for this is that the over-etching of the SiN layer led to the etching of Si underneath.

It can be concluded that the overall etch rate was 19.9±3.4 nm/min, and therefore, the optimal etch duration for gradual thinning is shown to take place potentially within approximately 2.5 min under the above stated RIE conditions.

3.3.2 Gradual etch of SiN

The next set of experiments was aimed at thinning the membrane gradually, therefore conducted with back-side processed wafers (Step VI, Figure 3.5). The first generation thinned nanopore devices[29] were fabricated in accordance to the above results (an etch duration of approximately 2.5 min). Work was carried out on a single wafer and the alignment of the back side features to the front features was achieved successfully. It was found that thinning the SiN down to 35-40 nm was feasible within 2.5 min, but the etch rate was unpredictable. The etch depth of SiN was observed to be as low as 20 nm in some cases.

The second generation nanopore devices were fabricated at different RW power; 25 W and 35 W. By doing so, etch depths of 20-25 nm at 25 W within 2.33 min and almost 50 nm at 35 W within 2.17 min were achievable. Etching at 25 W resulted in un-etched structures within the region of interest while the surface of the etched regions was relatively smooth at 35 W.

These preliminary experiments revealed that the etch quality can be improved by manipulating the etch parameters and the etch rate can be predicted by running test experiments prior to the sample processing. Therefore, next generation devices were processed with several additional steps to the second RIE (step VI, Figure 3.5);

- ***Plasma cleaning the RIE chamber*:** RIE chamber was cleaned prior to the investigation of the etch rate. The requirement for this step was that the measured bias value fluctuated and deviated from the set value significantly, although the parameters were being kept the same.

[29] Back side RIE was carried out by William Pitchford, AFM characterization was carried out by Dr. Agnieszka Rutkowska for these specific experiments while the KOH etch was performed by Thomas Gibbs.

- ***Further cleaning of the RIE chamber***: The chamber was run under the same conditions for a certain amount of time, in accordance to each particular experiment.

These two steps assure that any residual particles and gases remaining from the previous user are removed. It also improves the etching conditions by reducing the bias fluctuations during the etching[30]. Specific observations are given in related experiments below.

- ***Post-cleaning the wafer***: The wafer was treated with low energy O_2 plasma after the second photolithography step. Non-treated surfaces resulted in etching defects and nanopillar-like un-etched structures. The plasma duration was kept sufficient enough to remove the undeveloped resist from the regions of interest, without disturbing the resist-protected layer.
- ***Initial test experiments***: In addition to the above steps, a set of initial test experiments were conducted due to the unpredictability in gas conditions. In most cases, 5 x 5 mm individual plain SiN chips were used and the etch rate was defined by an ellipsometer.

Fabrication of the third generation thinned nanopore devices were conducted accordingly[31] and the results for the initial test experiments are shown in Figure 3.7a and Figure 3.7b, where the etch depth is plotted against the etch duration (i.e. 2.17-2.7 min) and the etch rate, respectively. The results given in Figure 3.7a can be interpreted to show a linearity in the etch depth over time. However, the etch rate at 2. 5 min etch duration deviated from the trend. A plausible explanation for this could be the assumptions made on the initial SiN thickness, where the thickness was assumed to be 72 nm. In fact, the SiN thickness is not uniform across the wafer and varies within an error rate of 10 nm. As a result, chips taken from different regions of the wafer would lead to different etch rates. From Figure 3.7b, the average etch rate was defined to be 23.5±3.3 nm/min, and therefore the sample wafer was etched for a duration of 2.7 min.

[30] However, measured RF power was still slightly lower than the applied power. It was assumed that the shortcoming of the system comes from the instrumental faults relating the power meter and voltage meter. Therefore it was regarded that the actual chamber conditions should be kept the same.
[31] RIE chamber was cleaned with the chosen gases under the same experimental conditions for 5 min.

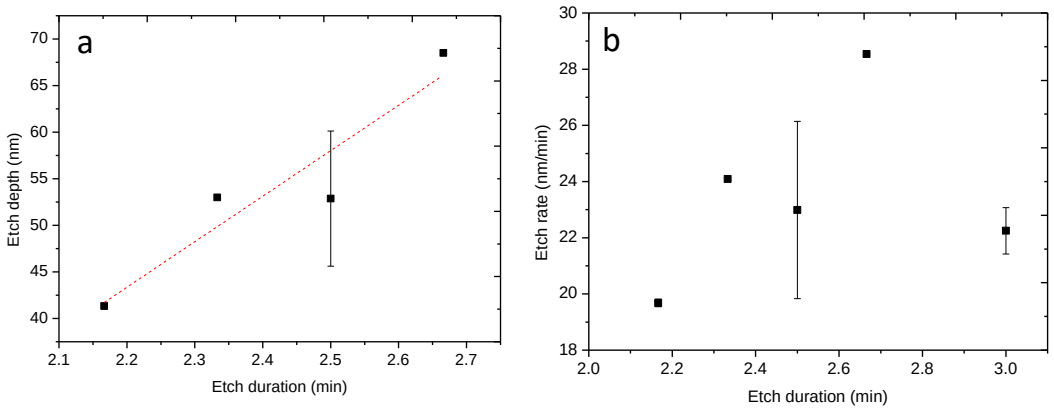

Figure 3.7 Etch results of the third generation thinned nanopore devices. a. Etch duration versus etch depth (dash line is used for illustration). b. Etch duration versus etch rate. Error bars represent the standard deviation of the mean, which was calculated from at least 2 different measurements taken from individual chips using ellipsometer.

After KOH etch (step VII, Figure 3.6), the characterization of 'the thinned regions' of the third generation devices was carried out by AFM (Agilent, USA). KOH etch allows free-standing SiN windows to be visible under light illumination and therefore the positioning of the AFM tip[32] could be directed precisely.

As shown in Figure 3.8, the sample was thinned down to about 45 nm with an etch rate of 10.7 nm/min. The etch rate was compared to the etch rate obtained from the initial test experiments (Figure 3.7) and found to show a 54% difference. Above observation is a well-known phenomena called '*aspect ratio dependant etch* (ARDE)', which states that the etch rate is faster for large features than the small ones **(12)**. This can be explained due to the geometrical limitations on the gas interactions with the exposed surface. In addition, the exposed area of the entire sample is also larger (5 x 5 mm test chips compared to 4 inch sample wafer), which further reduces the etch rate. The contribution of both cases to the discrepancy in etch rate was expected to be almost 50% and agrees well with the experimental findings.

[32] AFM tip is a PPP-NCHR probe (point probe plus non-contact/tapping mode-high resonance frequency, Nanosensors^{TM}, UK) and the tip radius is less than 10 nm with a 30 nm Al coating on the detector side, which promotes higher reflectivity.

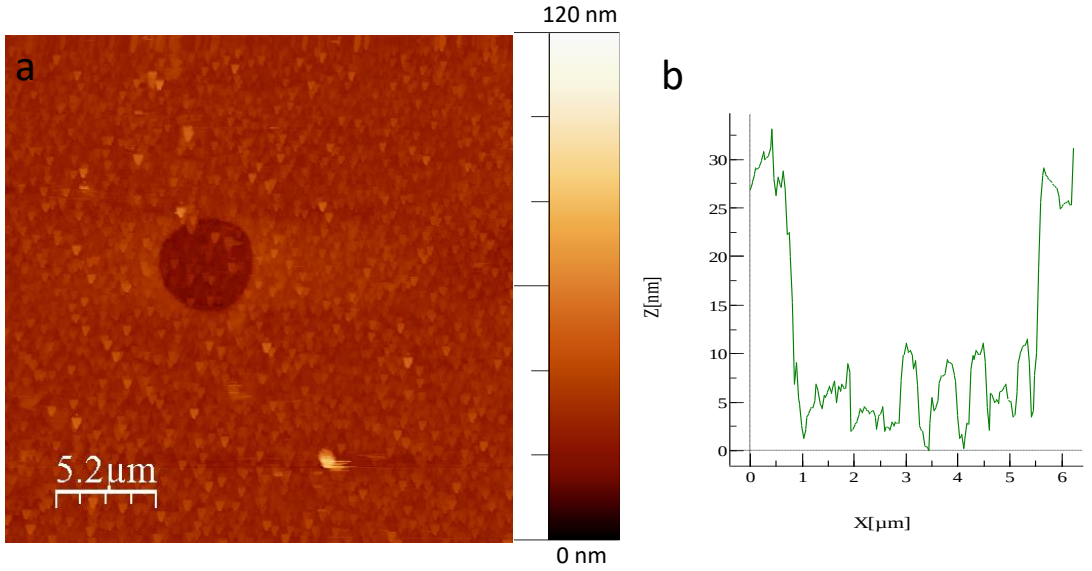

Figure 3.8 AFM characterization of the third generation thinned nanopore device. a. Topography image, and b. Surface profiling plot of the associated image.

Further work carried out with William Pitchford on the fabrication of the fourth generation thinned nanopore devices aimed to obtain thinner SiN membranes[33]. The etch rate was studied for two different RF power values; 25 W and 35 W. Ellipsometry measurements were taken for the

Table 3.1 Experimental readings of RF power and bias for the fabrication of the fourth generation thinned nanopore devices.

Set RF Power (W)	Power measured (W)	Bias measured (V)
25	15 ± 1	39 ± 2
35	24 ± 2	49 ± 1

initial SiN thickness of each test chip prior to etching, and this was compared with the etch results afterwards[34]. A further assumption was introduced at this stage that the higher RF power

[33] Cleaning procedure is kept same except that the RIE chamber was let running with the chosen gases for 30 min.
[34] In previous experiments, the thickness of each SiN chip was estimated to be the same; disregarding the regional differences in wafer thickness.

would improve the etch quality. Table 3.1 shows the experimental observations of the power readings of the instrument, indicating that stable bias and power readings had been achieved.

Figure 3.9a and Figure 3.9b illustrate the relationship between the etch duration and the depth of etched SiN thickness, and the etch rate, respectively. The average SiN thickness of the sample chips was 72 ± 3 nm.

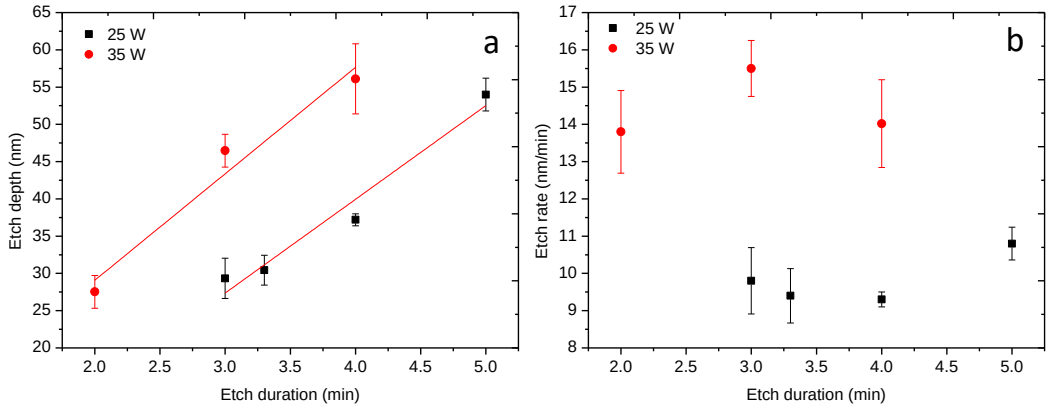

Figure 3.9 Etch results of the fourth generation thinned nanopore devices. a. Etch duration versus etched SiN thickness. II. Etch duration versus etch rate. Error bars represent the standard deviation of the mean, which was calculated from at least 2 different measurements taken from individual chips using ellipsometer.

The results indicated that there is a linear relationship between the etch depth of SiN and the etch duration with an R^2 value of 0.93 and 0.94 at 25 W and 35 W, respectively. The overall etch rate also remained more stable compared to previous experiments; 9.6 ± 0.3 nm at 25 W and 14.4 ± 0.9 nm at 35 W.

In accordance with the results of the test experiments above, the sample wafer was processed at 35 W for 5.5 min. As a result, the membrane was further thinned down to 20 nm with an etch rate of about 10 nm/min. The deviation from the initial etch rate was 24%. This indicates that the higher the RF power, the lower the deviation in the etch rate. As seen in Figure 3.10, the surface roughness changes in the order of 10 nm. In comparison with the earlier results, it can be concluded that the surface roughness was improved with the O_2 plasma cleaning step too. One of

the reasons for the observed surface roughness might be due to the lack of surface cleanliness of the thinned regions. Another reasonable explanation for this could be that a fluorocarbon layer on the SiN may have formed during the etching process which could have eventually slowed down the etch rate, which corresponds well with that approximated in literature (25% of its initial value) **(13)**. A combination of both reasons might lead to the observed un-etched structures.

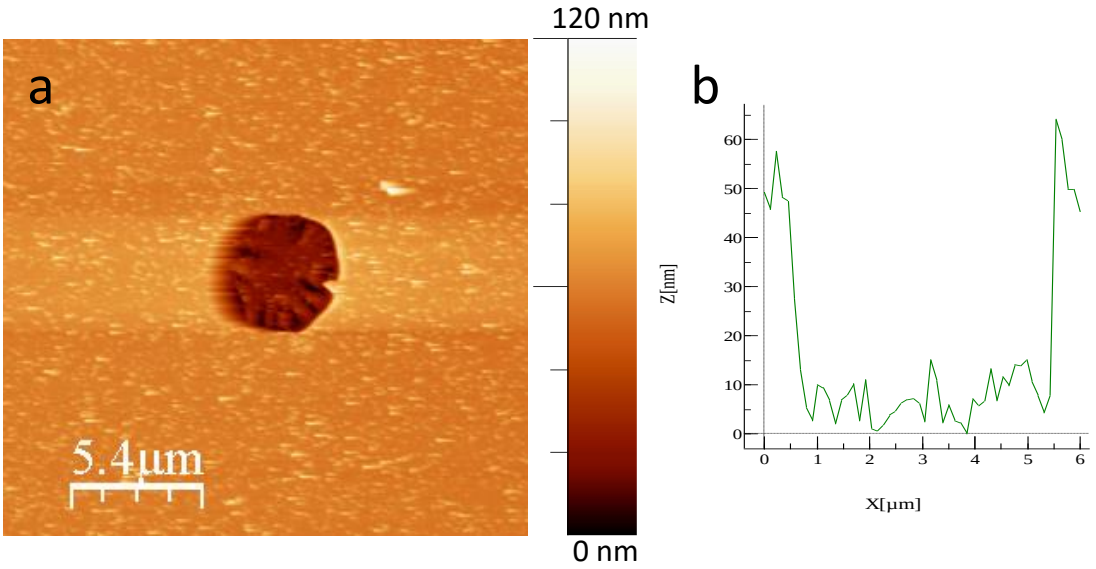

Figure 3.10 AFM characterization of the fourth generation thinned nanopore devices. a. Topography image, and b. Surface profiling plot of the associated image.

In conclusion, the chamber cleaning and the plasma cleaning of the wafer are highly recommended to be undertaken in order to achieve relatively high surface etch quality. Most importantly, the initial test experiments increased our predictions on the etch rate and contributed to the achievements of a stable plasma formation. The etch quality can be further improved by the addition of O_2 or N_2 gas (or both) to the stream of CF_4/Ar **(8, 13)**.

3.4 Nanopore fabrication

The alignment of the back-side features to the front-side features was highly successful as it always occurred within the SiN windows, as seen in Figure 3.11. The off-centred positioning of the thinned regions was within the flexibility of the alignment which is less than 10 µm. However the etched features were misshapen because of two reasons. Firstly, the photomask features were

originally distorted. In addition photolithography is diffraction-limitied and so the critical dimension (CD) that can be transferred successfully is approximately 1 μm, as shown in Equation 3.2;

$$CD = \frac{k\lambda}{NA}$$ Equation 3.2

where k is an experiment related-constant (0.5 – 0.8), λ is the wavelength of the UV light and NA is the numerical aperture of the optical lenses (0.5 - 0.6). This image degradation with small features is common and can be compensated, if necessary, by modifying the mask features, called '*optical proximity effect correction*' **(14)**.

The nanopore fabrication procedure is similar to that given in CHAPTER 2 with the only difference being the milling duration. The thinned nanopore devices could be drilled within a milling time of only 0.1 seconds to 2 seconds. The FIB imaging magnification used was either 60 kX or 80 kX. However with the fourth generation nanopore devices, a magnification of 50 kX had to be used due to several reasons.

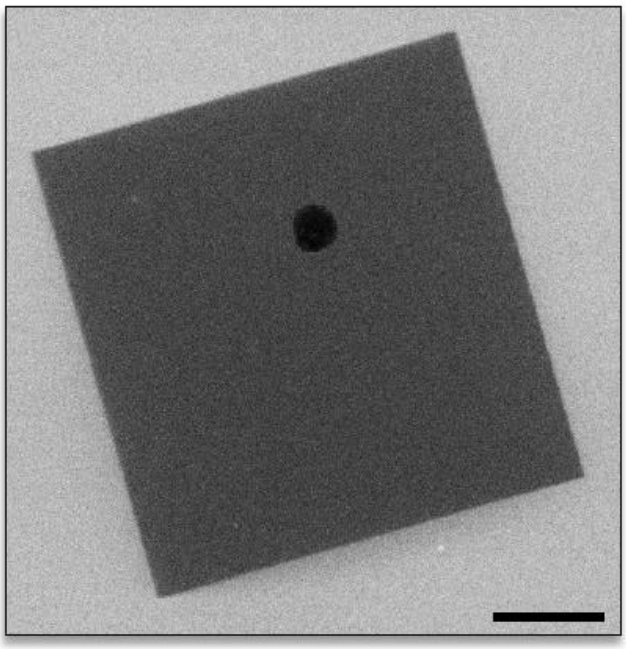

Figure 3.11 SEM image of the fourth generation locally thinned free-standing SiN windows. Darker gray: SiN window, black circle: thinned region. The scale bar is 10 μm.

When these devices were irradiated with the ion beam at high magnification (e.g. 80 kX), the SiN surface started to get distorted immediately and it possibly even thinned further. They were also torn apart from the thinned area once the milling was initiated. The final effect was that the thinned region was completely destroyed within seconds. A possible reason for the damage is that the pixel size becomes lower than 5 nm at high magnification, meaning that the diffusion area of the beam (probe size of 8 nm at 1 pA FIB beam current) becomes higher than the scanned pixel area. It is possible that this resulted in the overlapping of the beam sputtering, and hence intensified beam irradiation on the surface. Another possible reason is that the Ga^+ ion beam penetration depth is in the order of 10 nm **(15)**. It is thus clear that the currently used FIB is not suitable for very thin samples.

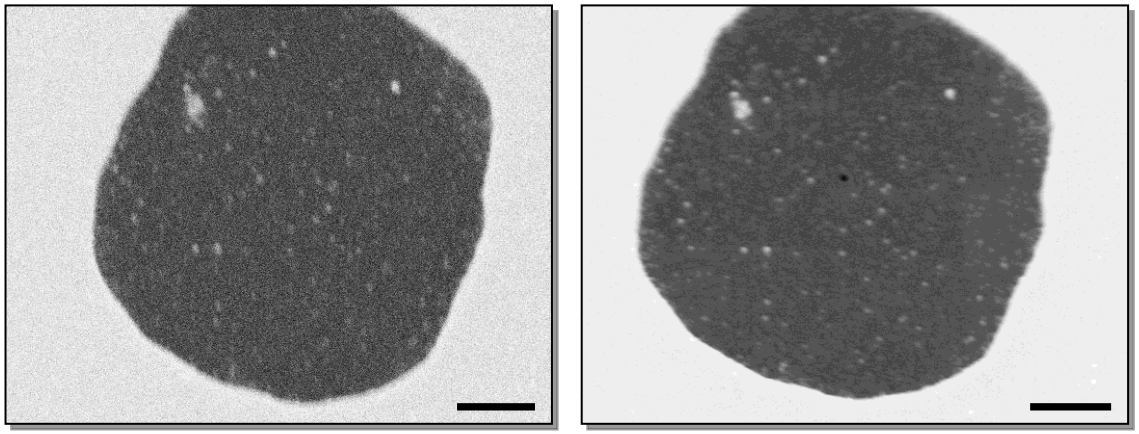

Figure 3.12 SEM image of the thinned region on a fourth generation locally thinned membrane. Left: SEM image before nanopore milling. Right: SEM image after nanopore milling. FIB parameters: 30 KeV, 1 pA, 50 kX, $t_{milling}$ = 0.1 seconds. d_{exp} = 65 nm. The scale bar is 1 µm.

The beam damage could be avoided by lowering the magnification to 50 kX, which resulted in the inevitable disadvantage of obtaining low image and milling quality. As a consequence, under these new conditions, only nananopores of a large diameter (approximately 100 nm) could be fabricated. Figure 3.12 shows SEM images before and after the milling. As concluded in the AFM characterization of the devices, the images depict that the surface of the thinned region is sufficiently smooth for nanopore applications.

3.5 Electrochemical characterization

Devices were characterized by measuring the ionic-current and calculating the nanopore diameter from the relevant I-V curves using Equation 2.5 and Equation 2.6. I-V curves measured using different nanopore devices are plotted in Figure 3.13; an unprocessed SiN chip (L_{SiN} = 100 nm) and a processed SiN chip (i.e. the first generation thinned nanopore devices (L_{SiN} = 40-45 nm) and the fourth generation thinned nanopore devices (L_{SiN} = 20-25 nm)).

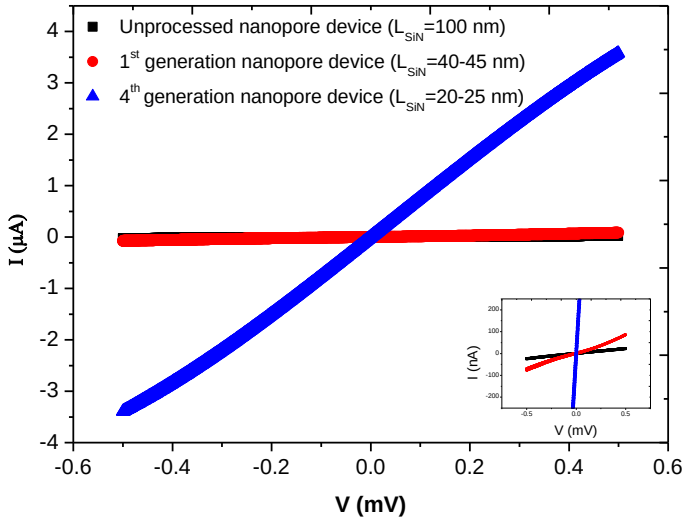

Figure 3.13 Cyclic voltammograms obtained using unprocessed and processed SiN chips. Black: I-V curve for unprocessed SiN nanopore, red and blue: I-V curve for the first and the fourth generation thinned nanopore device, respectively. FIB milling parameters; 30 kV acceleration voltage and 1 pA beam current, $t_{milling}$ = 6, 3 and 0.25 seconds, magnification = 60 kX, 60 kX and 50 kX, respectively. (1 M KCl, V range is ± 0.5 V).

Using a 100 nm thick unprocessed SiN nanopore device, a milling duration of 6 seconds resulted in the fabrication of pores with a diameter of 32-35 nm, calculated from the black I-V curve in Figure 3.13. When a first generation device was used, 3 seconds of milling duration[35] was sufficient to produce similar nanopore sizes, represented by the red I-V curve in Figure 3.13. However, a fourth generation nanopore device milled within 0.25 seconds resulted in the fabrication of 100 nm large pores in diameter, calculated from the blue I-V curve. Expectedly, as

[35] Even a milling duration of 0.5 s was sufficient to fabricate pores.

the membrane becomes thinner, lesser amount of ion beam irradiation is sufficient to drill nanopores with similar sizes. The conclusion is that for very thin membranes (i.e. L_{SiN}~20 nm), the ion beam within a milling duration of less than 1 second produces nanopores in the range of 100 nm in diameter.

3.6 Translocation of λ-DNA using locally thinned SiN nanopores

Translocation experiments were performed using the 40-45 nm thinned SiN membranes[36] and the results were compared to those of 100 nm thick unprocessed nanopore devices.

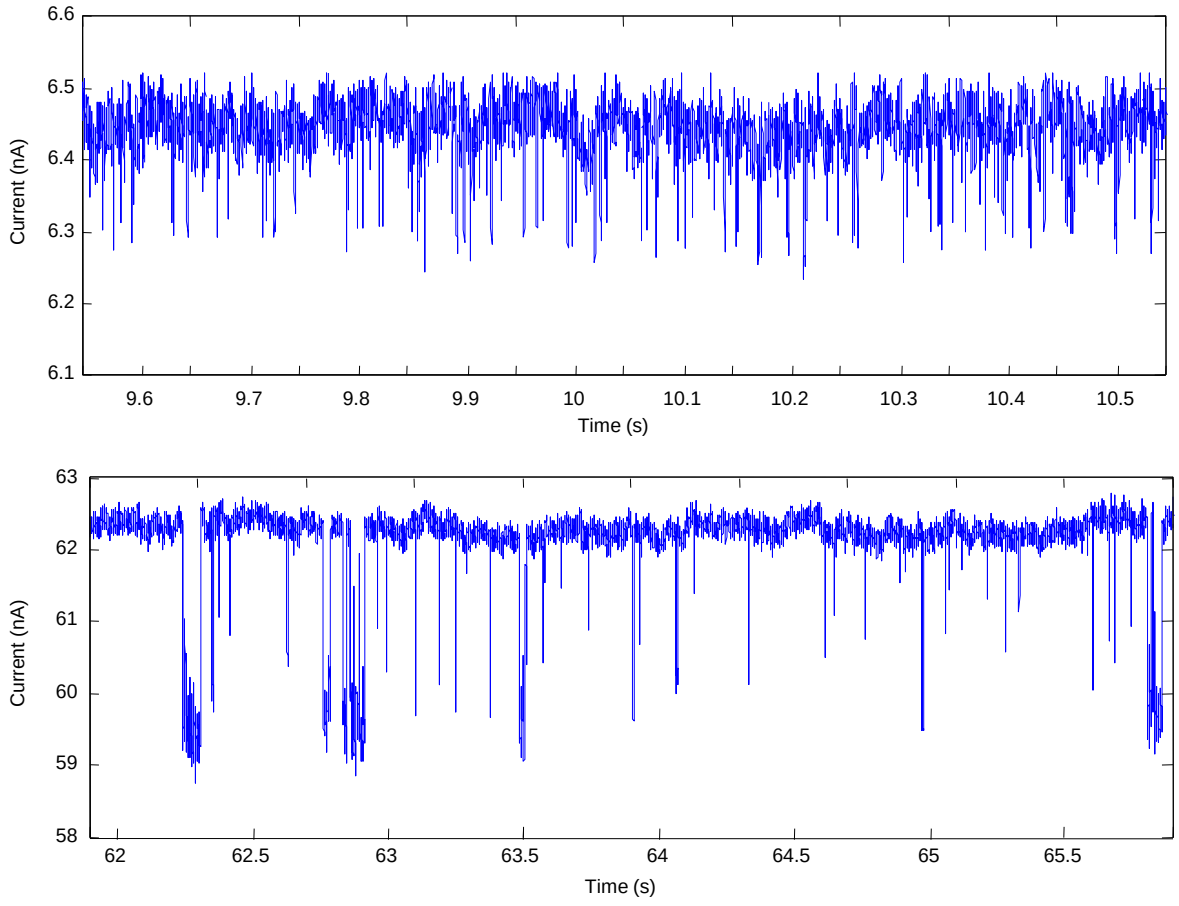

Figure 3.14 Examples of 10 seconds current-time traces recorded at 250 mV. Top trace: L_{SiN} = 100 nm, d_{exp} = 12-21 nm. Bottom trace: L_{SiN} = 40-45 nm, d_{exp} = 33-35 nm. d_{exp} was calculated using Equation 2.5 and Equation 2.6.

[36] Chip size was 5 x 5 mm.

Examples of current-time traces are shown in Figure 3.14; the top trace belongs to the translocation data recorded using 100 nm think SiN nanopores whereas the bottom trace is of 40-45 nm thin nanopores. The SNR is almost increased 3 times. Interestingly, the event frequency was comparably less than that obtained using thick membranes, which can be related to the differences in cleaning steps.

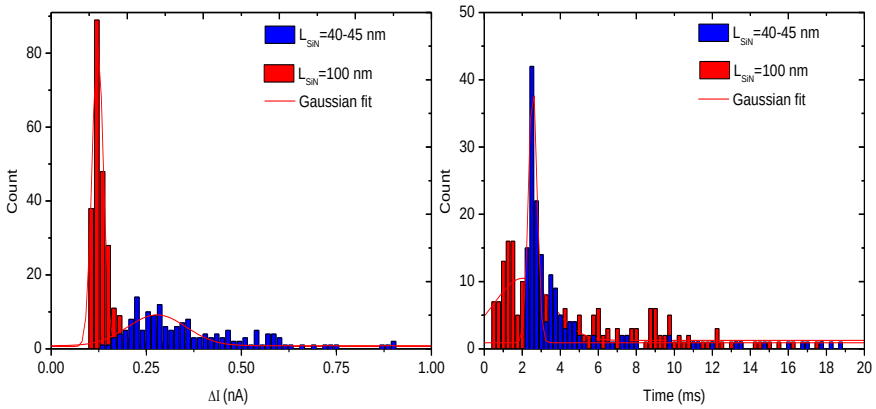

Figure 3.15 t_d and ΔI histograms for λ-DNA translocation events through nanopore devices with different nanopore thickness. Blue; L_{SiN} = 40-45 nm, red; L_{SiN} = 100 nm. The histograms were fitted with a Gaussian function.

Figure 3.15 presents t_d and ΔI distributions of λ-DNA translocation, fitted by a Gaussian function while Table 3.2 shows a summary of translocation statistics. By comparison to the data obtained with thick membranes, ΔI for thinned membranes was found to be 0.28±0.18 nA, which was almost 3 times higher and t_d yielded longer event duration (2.55±3.47 ms for L_{SiN} = 40-45 nm and 2.01±0.52 ms for L_{SiN} = 100 nm). The increase in ΔI is expected in accordance with Equation 1.15 and proves the enhanced detection capability of nanopore chips. However the change in t_d is contradictory to the expectations because the local electric field at the nanopore is higher for thinned nanopores used. In addition, one would anticipate a reduction in the interactions between a thinned nanopore and the molecule during translocation, and therefore a shorter t_d. The contradiction might be a consequence of the differences in the surface smoothness of the devices, where the molecule has to interact with the etched nanopore surrounding, which might in fact be slightly rough compared to the unprocessed SiN devices.

Table 3.2 Summary of λ-DNA translocation events shown in Figure 3.15.

L_{SiN} (nm)	t_d (ms)	ΔI (nA)
40-45 *(d_{pore} = 33-35 nm)*	2.55±3.47	0.28±0.18
100 *(d_{pore} = 12-21 nm)*	2.01±0.52	0.13±0.04

As a proof-of-principle, the voltage dependency of the translocation using thin membranes was also studied and it was found that ΔI increased when the voltage was increased from 250 mV to 300 mV. This is also in good agreement with theory.

3.7 Conclusion

We have demonstrated a detailed procedure to fabricate ultra thinned SiN nanopore membranes using RIE. To do so, two steps of photolithography and two steps of RIE were proposed and followed. One of the important findings was that the plasma has to be stabilised prior to specific experiments and several pre-characterization steps have to be followed in order to achieve highly predictable etch rate and smoothness. Secondly, it was found that the employment of higher RF power yields lower deviation in etch rate when switched from individual chips to a wafer. As a result of several optimization and characterization steps, SiN membranes from an initial thickness of about 72 nm to almost 20 nm could be successfully etched.

It was also found that the SEM/FIB experiments should be carried out with caution to prevent any damage to the thinned membrane. DNA translocation results also confirmed better SNR, as shown in literature.

References

1. Wanunu M, Dadosh T, Ray V, Jin J, McReynolds L, Drndic M. Rapid Electronic Detection of Probe-Specific Micrornas Using Thin Nanopore Sensors. Nat Nano. 2010;5(11):807-14.

2. Garaj S, Hubbard W, Reina A, Kong J, Branton D, Golovchenko JA. Graphene as a Subnanometre Trans-Electrode Membrane. Nature. 2010;467(7312):190-3.

3. Merchant CA, Healy K, Wanunu M, Ray V, Peterman N, Bartel J, et al. DNA Translocation through Graphene Nanopores. Nano Letters. 2010;10(8):2915-21.

4. Schneider GgF, Kowalczyk SW, Calado VE, Pandraud Gg, Zandbergen HW, Vandersypen LMK, et al. DNA Translocation through Graphene Nanopores. Nano Letters. 2010;10(8):3163-7.

5. Community MaN. Etching Process [27.11.2013]. Available from: https://www.memsnet.org/about/processes/etch.html.

6. Coburn JW. Plasma Etching and Reactive Ion Etching. Whetten NR, editor. California: American Institute of Physics, Inc.; 1982.

7. Williams KR, Muller RS. Etch Rates for Micromachining Processing. J Microelectromech Syst. 1996;5(4):256-69.

8. Kastenmeier BEE, Matsuo PJ, Oehrlein GS, Ellefson RE, Frees LC. Surface Etching Mechanism of Silicon Nitride in Fluorine and Nitric Oxide Containing Plasmas. Journal of Vacuum Science & Technology a-Vacuum Surfaces and Films. 2001;19(1):25-30.

9. **Kastenmeier BEE, Matsuo PJ, Oehrlein GS**. Highly Selective Etching of Silicon Nitride over Silicon and Silicon Dioxide. Journal of Vacuum Science & Technology a-Vacuum Surfaces and Films. 1999;17(6):3179-84.

10. Pant BD, Tandon US. Etching of Silicon Nitride in Ccl2f2, Chf3, Sif4, and Sf6 Reactive Plasma: A Comparative Study. Plasma Chemistry and Plasma Processing. 1999;19(4):545-63.

11. **University BY**. Koh Etching [27.11.2013]. Available from: http://www.cleanroom.byu.edu/KOH.phtml.

12. **Bai KH, Chi KK, Kim MC**. Ion and Neutral Transportation Consideration in Etching of Thin Si3n4 in High Aspect Ratio Structures for Aspect Ratio Independent Etching. J Vac Sci Technol B. 2006;24(3):1292-6.

13. **Kastenmeier BEE, Matsuo PJ, Beulens JJ, Oehrlein GS**. Chemical Dry Etching of Silicon Nitride and Silicon Dioxide Using Cf4/O-2/N-2 Gas Mixtures. Journal of Vacuum Science & Technology a-Vacuum Surfaces and Films. 1996;14(5):2802-13.

14. Harriott LR. Limits of Lithography. Proceedings of the IEEE. 2001;89(3):366-74.

15. Gierak J. Focused Ion Beam Technology and Ultimate Applications. Semiconductor Science and Technology. 2009;24(4).

CHAPTER 4
Integration of Nanopores into Microfluidic Channels

This chapter describes the integration of SiN nanopores into microfluidic channels. Starting with the design considerations of the microfluidic device, the fabrication of the microfluidic chip and marrying that with the SiN nanopore device are shown. The last part of the chapter provides information about the electrochemical cell setup of the integrated chip.

Nanopores have already proven to be an excellent alternative to conventional biosensing techniques such as gel/capillary electrophoresis or optical detection tools. The superiority of nanopores arises from their ability to probe molecules at single molecule level, or potentially at nucleotide level. Furthermore, the detection is label- and gel-free with high-throughput, cost and time effectiveness. Nonetheless, increasing the functionality of nanopores is the key to the development of nanopore-based biosensors. Perhaps the most conceivable way of doing so is to merge them into microfluidic channel networks as the microfluidic science is acknowledged to offer manufacturing of such portable devices. As regards to the microfluidic integration, following text provides a brief introduction about the kinds of microfluidic platforms and shows the reasons why PDMS is chosen in this project as the material of microfluidic channels.

Early generations of microfluidic networks were based on glass and subsequently silicon technologies. Glass microfluidic devices are frequently fabricated using wet etching, and assembled to make suspended structures by thermal or anodic bonding. However the glass technology is limited by the difficulties in creating complex geometries and integration. As an alternative, silicon devices have been widely used until the first introduction of polymer technologies in the field in the late 20th century. These are fabricated based on several alternating steps of wet and dry etching, Although the science of silicon micromachining is well established, silicon has also some undesirable drawbacks including its opacity, compatibility issues with chemical/biological functionalities, electrical conductivity, difficulties in fabricating moving parts and its integration into other materials if fabricated as a microfluidic chip, and most importantly the cost **(1-3)**.

Nonetheless, such materials are mechanically stable under extreme conditions, which are of great importance for a variety of applications outside laboratory. However polymers are now being more preferred, perhaps still for exploratory research, due to their simplicity in fabrication, compatibility with biological samples, and flexibility in integration into other microsystems as well as being electrical insulators **(1, 3, 4)**. A wide range of options (e.g. PMMA, PC or PDMS) is available to work with and most of them are non-toxic, chemically resistant, and optically

transparent. A polymeric microfluidic device can be fabricated by three step processes; mould manufacturing, replication of the polymer cast and assembly. While there exist different routes for each step[37], the most favourable one is arguably casting of PDMS by soft lithography, which was first introduced in late 90's **(5, 6)**. In contrast to chemical and physical etching required in glass and silicon technologies, soft lithography is rather simple and PDMS replication is extremely easy to perform, even in nanoscales, and to reproduce for rapid prototyping, because PDMS is a flexible elastomeric material that can form into any shape. The process starts with manufacturing of a mould with specific patterns, typically by the cross-linking of a photoresist on a silicon substrate upon UV exposure, pouring the PDMS matrix onto the Si master, and peeling it off after casting. Assembly or integration requires only a flat surface such as a glass slide and plasma treatment of both surfaces. It does have downsides as well, such as swelling of PDMS in most solvents, adsorption of molecules onto PDMS, and difficulties in creating 3D networks. However it still remains in the focus of many applications due to its simplicity and cheaper production. For the obvious reasons noted above, we choose to fabricate microfluidic channels using PDMS; the detailed procedure and its integration with the nanopore devices are outlined below.

4.1 Fabrication of microfluidic chips

4.1.1 Design considerations

The entire PDMS chip is 25 x 25 mm in size. The chip design consists of a microfluidic channel and two types of markers, as shown in Figure 4.1. Microchannel dimensions are 6 mm x 75 μm x 75 μm (length, width, depth, respectively), and results in less than 50 psi pressure drop across the channel (for flow rates smaller than 0.3 μl/min). This provides reasonable working conditions for the fluid flow. The centre of tubing connections are designed to be 2 mm away

[37]Some of the techniques that have been used for mould production are LIGA, the German acronym for 'Lithographie, Galvanoformung and Abformung' or 'lithography, electroforming, moulding', DRIE, deep reactive ion etch, and traditional micromachining techniques. Replication might involve of hot embossing, liquid injection or thermoforming.

from the edges of the SiN window so as to prevent leakage when the fluid is pumped through the channels.

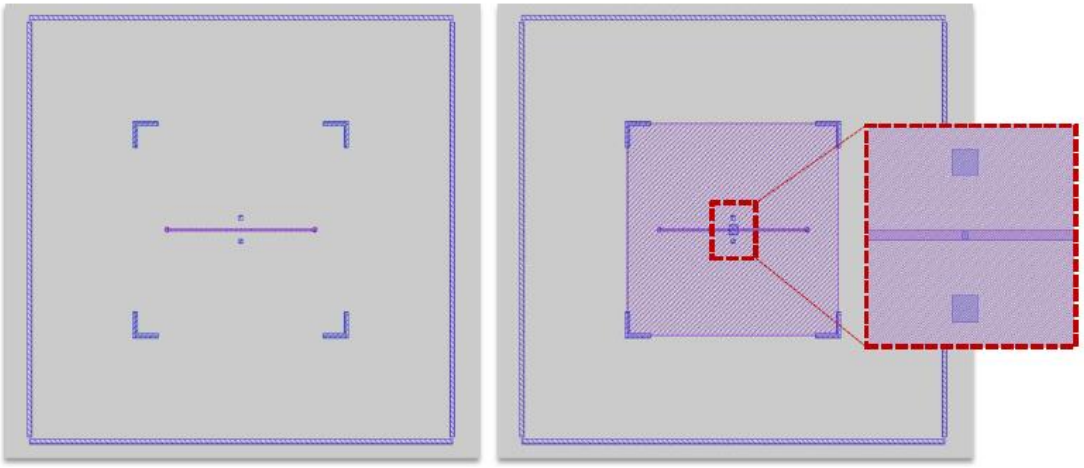

Figure 4.1 Snapshots of the proposed design of the PDMS and integrated chip (left and right images, respectively). Gray; PDMS chip, purple square; SiN chip, inset; free-standing SiN membrane aligned to the centre of microfluidic channel.

The design consists of several markers on each individual chip, which aimed to assist the positioning of the PDMS chip onto the nanopore device and the finer alignment of the channel to the SiN window. For example, the square markers in the centre of the PDMS chip assure the central positioning of the chips and that the channel is entirely embedded onto the SiN chip. They are 200 μm x 200 μm wide windows and the centre-to-centre distance is 450 μm. In a 75 μm wide channel, it means that the gap between the edge of the marker and the channel is around 275 μm and sufficiently wide to maintain the channel structure during PDMS-peeling. Each mask design contains of 12 individual chips. The layout for the photomask was drawn in KLayout drawing software, if necessary, modified by AutoCad Civil 3D. Acetate mask was produced by Micro Lithography Services Ltd, UK.

4.1.2 Device fabrication

PDMS kit (Sylgard 184A, Dow and Corning, UK) is a two-part silicone resin solution, containing a curing agent and base (cross linker). Once mixed thoroughly at certain ratio and poured onto a structural template (mould), the structures are imprinted on the PDMS cast.

Change in the mixing ratio results in different rigidity of the chip. The mould can be used for multiple times and generally fabricated on a Si wafer. A negative epoxy photoresist (SU- 8 photoresist, MicroChem, UK) is used as the moulding media with high chemical and thermal stability. It is suited for near UV radiation (350 - 400 nm) and UV light gives rise to the cross-linking of the resist to the substrate surface by heat. Fabrication of the PDMS is well-documented in the literature **(7)** and any form of it can be reproduced easily.

The mould fabrication process was conducted according to the product protocol described below, and the workflow of the fabrication procedure is illustrated in Figure 4.2;

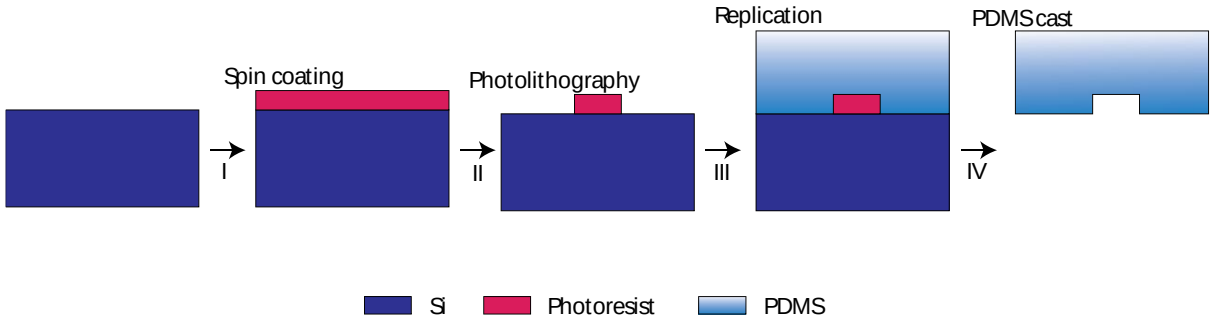

Figure 4.2 Fabrication workflow of the PDMS chip. I. Spin-coating the photoresist. II. Photolithography and resist development. III. PDMS casting. IV. PDMS chip peeled off.

- The wafer (IDB Technologies, UK) is rinsed with acetone and then DI water, dried with N_2.
- The wafer is then pre-baked at 95 ^oC for a few minutes in order to dehydrate the surface.
- The resist is spin-coated on the wafer at 2000 rpm for 30 seconds. Recommended amount of the resist is 1 ml per inch of the wafer diameter (Step I, Figure 4.2).
- The wafer is then soft-baked at 65 ^oC for 5 min and at 95 ^oC for 15 min. It is necessary to evaporate the solvent which thus leads to the densification of the coated layer.

- The mask is placed on the wafer with a glass plate at the top, and stabilized with tapes after which the substrate is exposed to the UV light from glass side with an exposure energy of around 200 mJ/cm^2.
- Post exposure bake conditions are 1 min at 65 ºC and 4 min at 95 ºC.
- MicroChem's SU-8 developer is used to develop the resist by simply immersing the wafer into the developer solution for 6 min (Step II, Figure 4.2).
- The wafer is then rinsed with IPA and dried with N_2.
- The final mould thickness is about 75 μm.

PDMS replication and casting process is as follows;

- PDMS curing agent and the base are mixed at 9:1 weight ratio.
- The mould is placed into a square petri dish and the PDMS casting mixture is poured down onto the mould (Step III, Figure 4.2).
- PDMS is then degassed under vacuum for about 30 min.
- Then the petri dish is heated up at 65 ºC for about 2 hours to cast the PDMS.
- As PDMS is hydrophobic, it does not stick to the mould and individual PDMS chips are gently removed by cutting them with a razor blade and the holes for the inlet and the outlet of the channel can be opened (Step IV, Figure 4.2).

4.2 Integration

Integration was achieved by plasma treatment of the surfaces and bringing the chips into contact afterwards. Plasma is created upon the application of a strong electric field and leads to the ionization of the oxygen gas into negatively and positively charged ions and radicals. The radicals attack the substrate surface and thereby change the surface properties chemically. For PDMS, it is hydrophobic once fabricated due to its –O-Si$(CH_3)_2$- methyl groups. After the plasma treatment, these groups are converted to silanol groups –O-Si(OH)-, which is hydrophilic **(8)**. Depending on the plasma power, treatment duration and gas pressure, the level of hydrophilicity can be changed, thus the bonding strength. In general low plasma power for short duration

varying from 75 W power, 75 mTorr pressure to 20 W, 30 mTorr for less than a minute is advised **(7-9)**. In addition, plasma treatment results in the removal of the organic contaminants on the surface of both chips, which improves the smoothness of the surface.

Integration process is described below;

- 1 mm holes were opened up in PDMS chip using a 1 mm punch with plunger (Selles Medical Ltd, UK) and the chip is sonicated in ethanol for 20 min, washed in water, and dried with N_2.
- SiN chip was immersed into acetone, IPA and water for 5 min, respectively, and dried with gentle application of N_2.
- Both chips (flat surface of the SiN chip and channel side of the PDMS chip) were exposed to oxygen plasma (Harrick Plasma, USA) for about 70 seconds. The chips were brought into contact under a stereomicroscope, straight after the plasma treatment (within 20 seconds). The SiN chip was fixed under the optics using an adhesive film (Gel-Pak, UK) while the PDMS chip stayed mobile for the manual alignment. Otherwise, controlling the stability of both chips during integration and the alignment becomes impossible. The field of view of the microscope for the alignment was about 4 mm (Magnification 4x) and enabled easy and reproducible alignment.

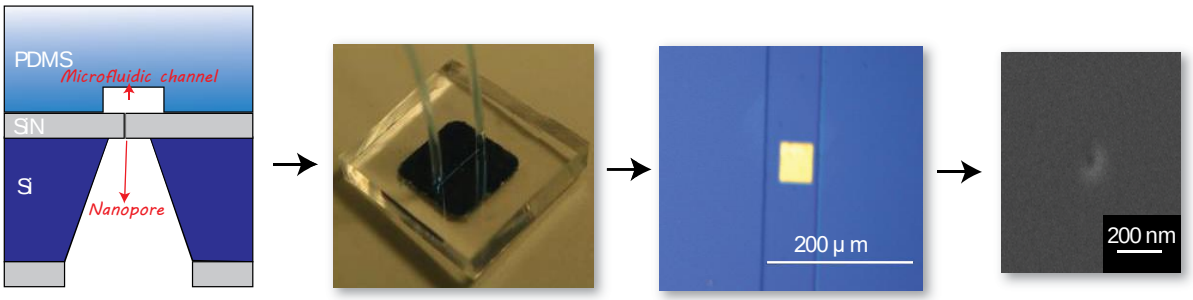

Figure 4.3 Far left: Schematic of the integrated chip. Left image in the middle: Photograph of the chip. Right image in the middle: Optical image of the microfluidic channel aligned to the free-standing SiN window. Far right: Example SEM image of a nanopore.

- Upon the alignment, pressure was applied on the integrated chip manually in order to strengthen the bonding between both chips. After carefully removing the chip from the adhesive surface, the chip was placed on a hot plate at 80 ºC for couple of hours. It was found that increasing the temperature up to 100 ºC improves the bonding and thus shortens the bonding time. A heavy plate was placed at the top of the chip. In contrast, bonding of the PDMS to glass is relatively stronger that does not require the application of an external pressure.

Figure 4.3 presents a schematic of the integrated chip and a photograph of the actual device (far-left and left, respectively) as well as an optical image of an example (right), where a 73±2 µm wide microfluidic channel was integrated onto a 50 x 50 µm free-standing SiN window (yellow square) with a nanopore. An example SEM image of a nanopore (d_{pore} = 23±5 nm) is shown in the far-right figure. The success rate of alignment is sufficiently high, providing that the surface of each chip is clean, smooth and hydrophilic enough.

4.3 Cell setup of the integrated nanopore chip

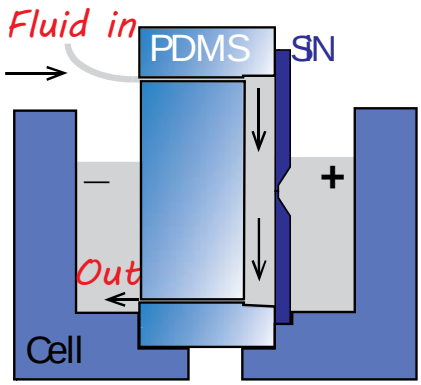

Figure 4.4 Schematic of the cell assembly and electrochemical set-up.

The SiN side of the integrated chip was exposed to O_2 plasma for at least 5 min and wetted first with ethanol and then DI water. Electrolyte solution was infused into the microfluidic channel after the tubing of the syringe was inserted into the inlet opening of the PDMS chip. The principle of the cell design is similar to the common nanopore cell platforms, where the cell contains 2 compartments. Schematic of the integrated chip nanopore cell set-up is shown in

Figure 4.4. The chip was tightly sealed between two polymeric cell reservoirs, where the edges of the SiN chip in the trans reservoir is protected precisely in order to eliminate any noise contribution to the current signal. The volume of the chambers is approximately 1 mL while the sample volume of the microfluidic channel is about 1 nL. Prior to each experiment, electrolyte solution was flushed through the channel for at least 10 min at 1 - 5 µl/min flow rates and then both reservoirs were rinsed with DI water followed by the electrolyte, so that any residual particles either inside the channel or outside was removed.

4.4 Apparatus setup

It is important to remember that as much as possible should be done to avoid noise during recording, it would otherwise be harder to eliminate it later while trying to analyse the data.

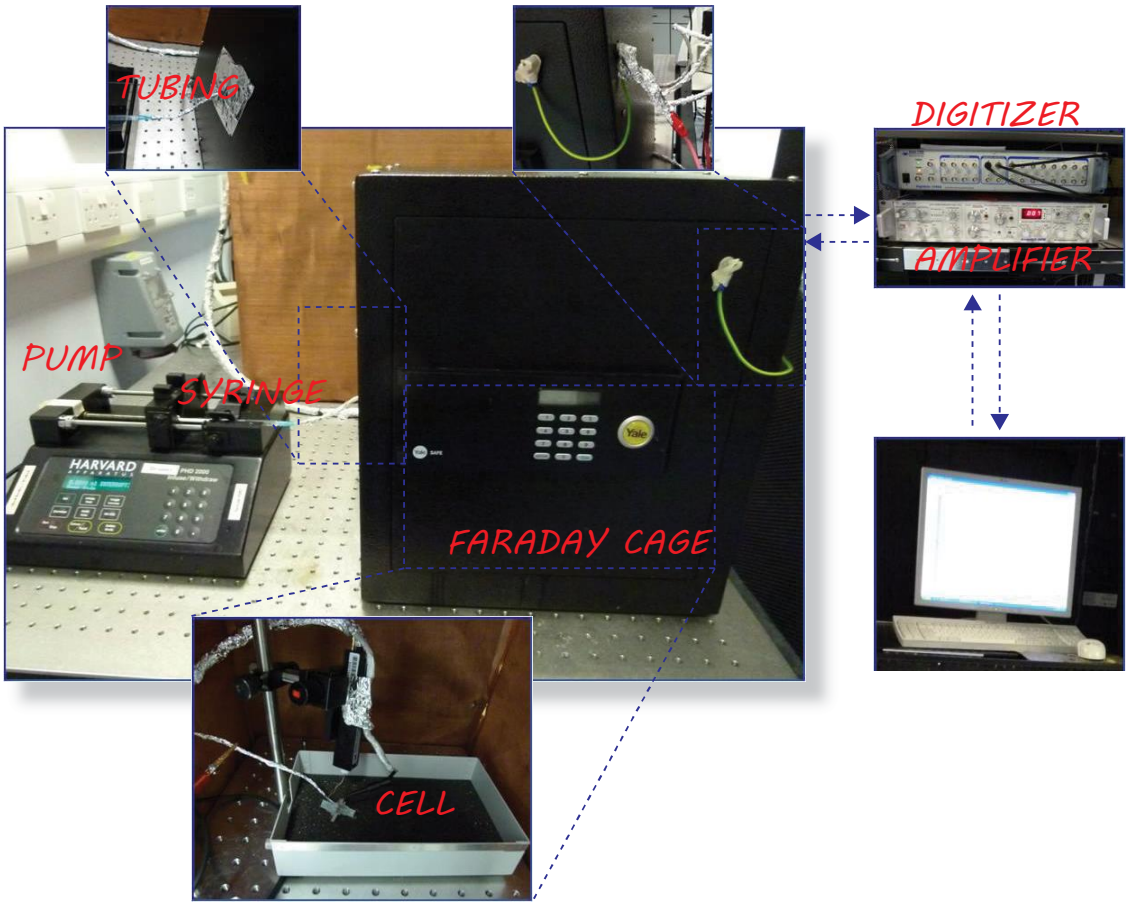

Figure 4.5 Photography image of the apparatus setup.

Therefore several precautionary steps were followed to minimize the noise: All the cables connecting the head- stage to the amplifier and the digitizer were wrapped in aluminium foil. The apparatus was placed in a Faraday cage[38] on an anti-vibration table. Faraday cage provides the isolation of the electrochemical set-up from any possible external electrical interference. Syringe tubing connection between the pump (Harvard Apparatus, UK) and the chip was also wrapped in aluminium foil tightly for the same reason and grounded. The outside connections to the cage were supplied through a hole where it was also sealed with insulating tapes. Moreover, the cage was also grounded. Figure 4.5 illustrates all the precautions stated above as well as the apparatus set-up inside the cage and the amplifier instrumentation.

4.5 Conclusion

In this chapter, the integration of SiN nanopore devices into PDMS microfluidic channel has been demonstrated. Compactness of the device is an immediate advantage compared to conventional SiN chips in terms of easy handling and the reduced sample volume is an extra benefit of the chip on account of the sample consumption. Moreover, the concept of integration can be applied to any other planar nanopore devices by simply changing the geometries of each individual chips. More importantly, the integration introduces the capability of in-flow electrochemical detection at single molecule level.

References

1. Abgrall P. Lab-on-Chip Technologies: Making a Microfluidic Network and Coupling It into a Complete Microsystem—a Review. Journal of micromechanics and microengineering. 2007;17(5):R15.

2. Xia Y, Whitesides GM. Soft Lithography. Angewandte Chemie International Edition. 1998;37(5):550-75.

[38] In our experiments, a Safebox was used.

3. Quake SR, Scherer A. From Micro- to Nanofabrication with Soft Materials. Science. 2000;290(5496):1536-40.

4. Whitesides GM. The Origins and the Future of Microfluidics. Nature. 2006;442(7101):368-73.

5. Effenhauser CS, Bruin GJM, Paulus A, Ehrat M. Integrated Capillary Electrophoresis on Flexible Silicone Microdevices: Analysis of DNA Restriction Fragments and Detection of Single DNA Molecules on Microchips. Analytical Chemistry. 1997;69(17):3451-7.

6. Duffy DC, McDonald JC, Schueller OJA, Whitesides GM. Rapid Prototyping of Microfluidic Systems in Poly(Dimethylsiloxane). Analytical Chemistry. 1998;70(23):4974-84.

7. Jo BH, Van Lerberghe LM, Motsegood KM, Beebe DJ. Three-Dimensional Micro-Channel Fabrication in Polydimethylsiloxane (Pdms) Elastomer. J Microelectromech Syst. 2000;9(1):76-81.

8. Tang KC, Liao E, Ong WL, Wong JDS, Agarwal A, Nagarajan R, et al. Evaluation of Bonding between Oxygen Plasma Treated Polydimethyl Siloxane and Passivated Silicon. International Mems Conference 2006. Journal of Physics Conference Series. 342006. p. 155-61.

9. Bhattacharya S, Datta A, Berg JM, Gangopadhyay S. Studies on Surface Wettability of Poly(Dimethyl) Siloxane (Pdms) and Glass under Oxygen-Plasma Treatment and Correlation with Bond Strength. J Microelectromech Syst. 2005;14(3):590-7.

CHAPTER 5
Optical Investigation of DNA Behaviour in Flow

The motivation of this chapter emerged from the need to understand flow characteristics and the rheological properties of DNA. To achieve these aims, we utilized a commonly used fluorescence based single molecule tool; Confocal Microscopy which offered the greatest advantage of exploring single molecule kinetics along with conventional fluorescence microscopy for visualization of molecules in real-time.

To begin with, the working principles and the necessary instrumentation of these tools are briefly described. Secondly, DNA and its fundamental physical qualities are presented. In the final sections, the experimental findings are discussed; the flow velocity measurements by both techniques, the determination of the flow velocity and flow-limited regime by FCS, and the study of DNA behaviour in flow, respectively.

5.1 Principles of fluorescent imaging

5.1.1 Phenomena of Fluorescence

Fluorescence in its simplest term is the re-emission of absorbed light by a fluorescent molecule, called a '*fluorophore*'. Fluorophores are typically highly conjugated organic molecules. Upon the absorption of light, the electronic state of a fluorophore is excited from the so-called '*ground-state*' to a higher electronic state. Photons with lower energy, longer wavelength are emitted during relaxation back to the ground electronic state. This results in a shift between the absorption and emission spectra, which is called '*Stokes shift*'. Stokes shift is an essential property which forms the basics of the fluorescence detection. The details of the fluorescence process is easily illustrated by a Jablonski diagram **(1)**. As shown in Figure 5.1, S_0, ground state, represents the energy level of the molecule before the excitation while S_1 and S_2 are the excited energy states.

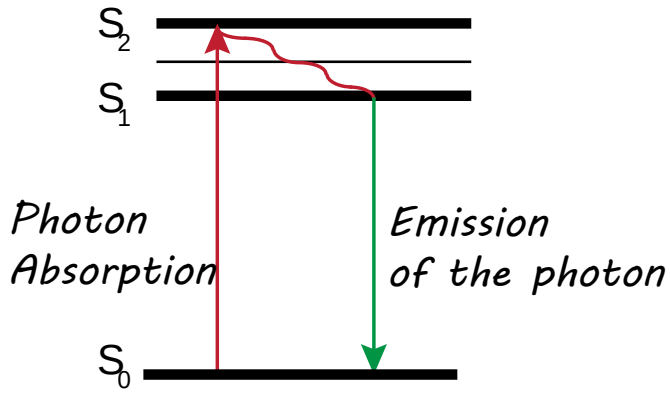

Figure 5.1 Schematic of a Jablonski diagram.

Other important measurable properties include fluorescence quantum yield, intensity and life-time. Fluorescence quantum yield is the ratio of number of emitted photons to the number of photons absorbed. Because of the energy losses in the process, the quantum yield is generally a figure less than the unity. A flurophore with high quantum yield indicates high fluorescence intensity. The third feature, fluorescence life-time is defined by the average time the molecule

spends in the excited state before returning to the ground state. The fluorescence life-time is generally in the order of nanoseconds, while excitation occurs within femtoseconds **(2)**.

5.1.2 Fluorescence Microscopy

Fluorescence detection in a microscopy set-up is mainly based on the Stokes shift. A specific wavelength of light is used to illuminate the sample and the fluorescent light emitted, with a longer wavelength, is collected separately. In principle, one can build-up a very powerful fluorescence microscope on account of this fact, by initially adding-on specific optical tools to a conventional optical microscope and digitizing the signal for high-quality reproduction.

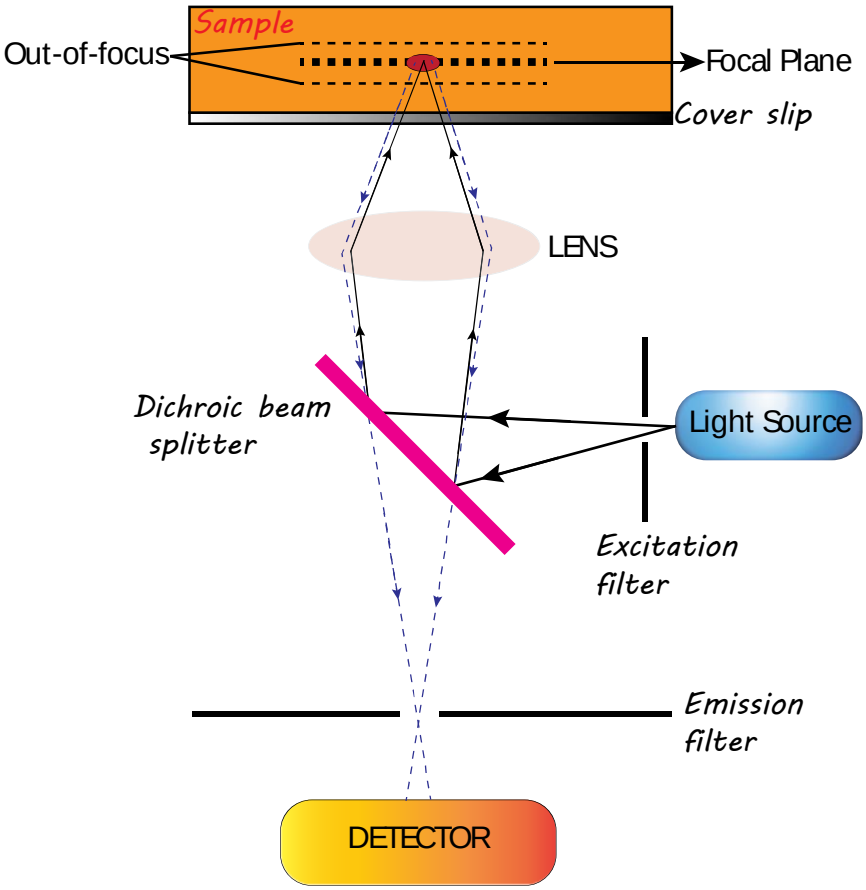

Figure 5.2 Basic components of Confocal Fluorescence Microscope; light source, filters, mirrors, objectives and a detector.

The simplest method to carry out fluorescence detection is to use wide-field fluorescence microscopy (FM). In wide-field FM, the entire sample is exposed to the light and the fluorescence readout can be viewed by an eye piece or a camera. A more advanced version of an

FM is a confocal FM, here the excited light is more focused (single-spot illumination) and the out-of-focus light coming from the sample is rejected by a pin hole just before the detector, as shown in Figure 5.2. The detection is primarily based on counting single photons emitted from the probe volume over time. More sophisticated FMs exist such as scanning confocal FM and Total Internal Reflection Fluorescency (TIRF). The former is an extended version of a confocal FM, which raster scans the sample with focused light, pixel by pixel, generating 3D cross-sectional images of a sample. In TIRF, only a small portion of the sample is illuminated by an evanescent wave of light so the background fluorescence interference becomes negligible **(3)**. In both cases, the readout signal is improved compared to a conventional FM.

Both wide-field and confocal FM have been used in the research carried out in this chapter. The following section aims to briefly introduce the necessary components of these tools.

5.1.3 Components of a fluorescence microscope

Necessary components of a fluorescence microscope, either wide-field or confocal, are a light source, filters, an objective and a detector.

- **Light source:** The light source has to be powerful enough to provide a detectable signal owing to the low intensity of the emitted signal compared to the excitation source. Mercury or Xenon arc lamps are commonly used in wide-field FM. These lamps are sources of white light with a number of sharp lines occurring at a specific wavelength (e.g. 450 nm and above 800 nm for Xenon arc lamp). For these, it is necessary to use an excitation filter for a specific fluorophore in order to select correct excitation wavelengths. For a confocal FM, a laser diode is used instead, which provides monochromatic light with a much higher intensity which is easily focused. Potential wavelengths range from 400 nm to 1500 nm **(2)**.
- **Filters:** 3 sets of optical filters are required; an excitation filter, a dichroic beam splitter and an emission filter. The excitation filter is employed in order to disperse polychromatic or white light into a monochromatic light at a specific wavelength for

maximum sensitivity. The dichroic beam splitter reflects the excited signal to the objective and transmits the emitted signal to the detector without any cross talk between them. An emission filter is usually placed before the detector so as to reject any interference from the excited light to the signal with already low intensity.

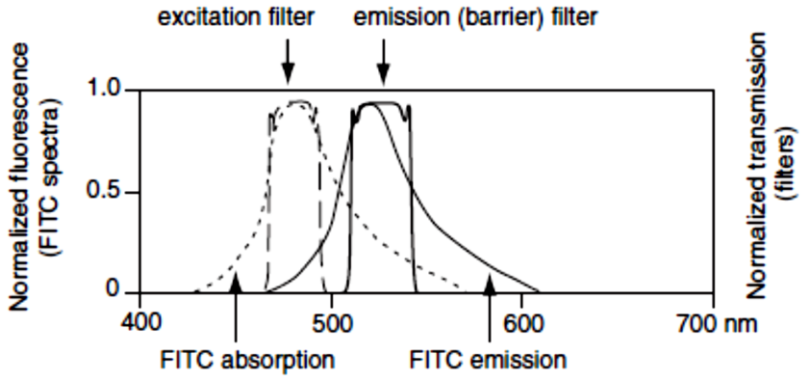

Figure 5.3 An example of normalized absorption and emission of spectra for a dye, fluorescein isothiocyanate, (FITC) and transmission spectra of excitation and emission filters (4).

- **Objectives:** The quality of the image is primarily determined by the objectives as the light reaches the sample through the objective for the first time and the emitted signal is collected by the objective **(5)**. The resolution depends on the wavelength of the light, the refractive index of the imaging medium and the angular aperture of the objective. The relationship between these factors is given by Rayleigh criterion shown in Equation 5.1;

$$R = {}^{\lambda}/_{2n(\sin x)} \qquad \text{Equation 5.1}$$

where R is the resolution, λ is the wavelength of the light, n is the refractive index of the medium between the sample and the objective (e.g. air, water, oil) and x is equal to half of the angular aperture of the objective. The function '*n(sinx)*' defines the numerical aperture (NA) of an objective which is an indicator of the resolution of an objective. Another important property related to NA is the depth of field, Z, which is the maximum

distance between the sample and the objective **(6)**. The relationship between NA and Z is shown in Equation 2;

$$Z = n\lambda NA \qquad \text{Equation 5.2}$$

- **Detectors:** Detectors in FM convert photons of light into electric current. Zero-noise detectors with 100% photon conversion efficiency (often called quantum efficiency) would be ideal for capturing high quality images. However the best detectors available on the market can only convert light with 80%–90% efficiency due to noise contributions generated within the device or out-of-focus background. Avalanche photodiodes are frequently used. These are highly sensitive and capable of working in the red and near infrared region of the spectrum with quantum efficiencies up to 70% **(7)**.

  CCDs are another type of detector. These accumulate charge in proportion to the photon intensity. Charge accumulation occurs in the form of pixels and is converted to an image, which may be dynamic or static. Previously CCDs have exhibited lower QE, however recently developed 'electron multiplying CCDs, EMCCD, have overcome this problem by using an output amplifier additionally (up to 90% QE) **(8)**. Other advantages of EMCCDs include reduced background noise and faster response time compared to that of CCDs **(9)**.

  In a confocal FM, APDs are preferably used as it allows single photon counting. Wide-field FMs are generally associated with a CCD camera or EMCCD for real-time monitoring of the dynamics in the sample.

The technology of FM is vast and out of the scope of this chapter. The detailed study of the subject can be found in relevant references **(2, 4)**. However, it can be highlighted that appropriate optical components are chosen depending on the application and there is frequently a compromise between sensitivity, spatial resolution and temporal resolution **(10, 11)**.

5.2 Physical qualities of DNA

DNA is the genetic code of life, upon which all the existential functions and survival of living organisms rely. The first identification of DNA was in the late 19th century when Friedrich Miescher isolated a hitherto unknown entity with a large portion of phosphorous groups **(12)**. It was many years later that Watson and Crick proposed the double-helix structure of DNA in 1953, in a landmark study **(13)**. Despite the fact that many have contributed to the elucidation of how DNA works, our knowledge of DNA and its functions today primarily stems from this discovery.

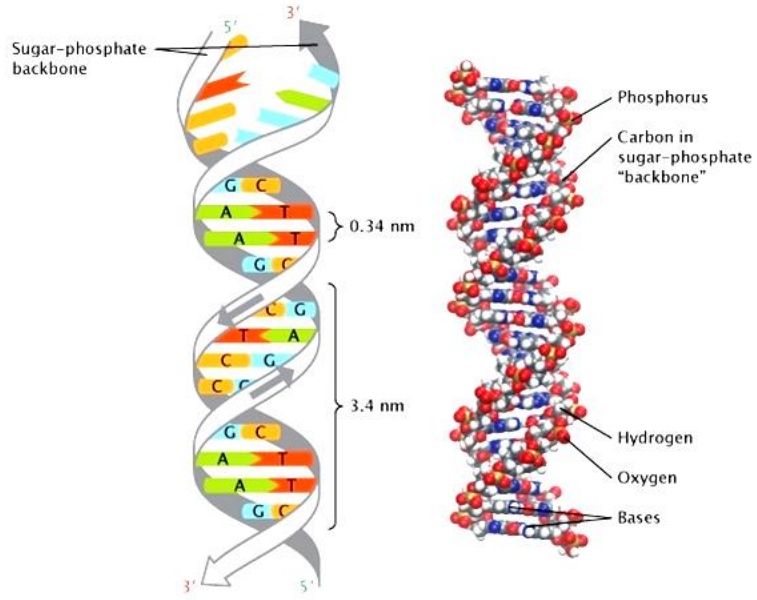

Figure 5.4 Double helix structure of DNA (14).

DNA is a semi-flexible charged polymer composed of alternating units of building blocks called nucleotides. Nucleotides consist of one of four potential types of bases (adenine, guanine, thymine or cytosine) covalently bound to a deoxyribose sugar and a phosphate group. Single stranded DNA, ssDNA, consists of a sequence of bound nucleotides via phosphodiester bonds, whilst double stranded DNA, dsDNA, is composed of two complementary DNA strands linked together via hydrogen bonds (i.e. adenine to thymine, guanine to cytosine). The cross-section of DNA strand is approximately 1 nm for ssDNA and 2.2 nm for dsDNA. The distance between two

nucleotides units is 0.34 nm. Incredibly, human DNA, with a total length of about 2 m, is compacted into chromosomes within a single cell.

There are a couple of universally accepted length scales often used to describe the state of DNA in more detail when either free or confined. For example, the total length of DNA when stretched fully is described by the '*contour length*' (L_c). This is the product of N nucleotides, or monomers, with a length of a;

$$L_c = Na \qquad \text{Equation 5.3}$$

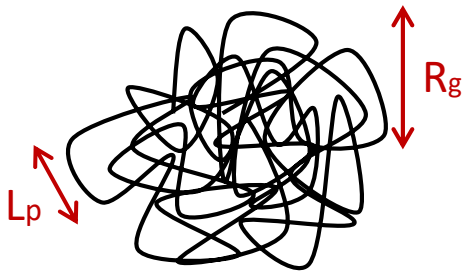

Figure 5.5 Relaxed DNA, coiled up in solution.

However, DNA in its relaxed state is coiled up and has a spherical shape defined by a gyration radius (R_g), where R_g scales with $N^{0.6}$. The helical structure of the sphere contains semi-flexible units of the strand with a certain degree of stiffness named by the persistence length (L_p). It is a way to measure the chain flexibility and differs depending on several factors such as solution concentration **(15)**. For instance, λ-DNA with a contour length of 16.5 μm has a R_g of ~734 nm at thermal equilibrium and consists of 500 persistence lengths. L_p is estimated to be 33 nm at 1 M NaCl and 51 nm at 0.1 M NaCl **(16, 17)**. When confined within a volume smaller than $2R_g$, DNA is forced to deform from its relaxed state. An elaborative review on DNA in confinement and confinement related DNA studies can be found in reference **(15)**.

5.3 Experimental set-up

5.3.1 Instrumentation

A custom-built confocal FM set-up was used. This was built around a commercial microscope (Olympus IX71). The microscope is equipped with a mercury lamp and an EMCCD camera (Photometrics, The cascade II 1024) with a QE of 90% for wide-field imaging. The camera is thermoelectrically cooled down to -60 ºC for maximum performance. A water immersion 60x objective (UPlanSapo 60XW, Olympus) with a numerical aperture of 1.20 was used for imaging. Working distance of the objective is 280 μm. The image acquisition was performed with an open-source software package; Micro–Manager, which runs as a plugin to ImageJ **(18)**. The software settings were as follows; binning was 1, the exposure time and gain was kept constant at 0.1 ms and 3, respectively. Brightness and contrast were adjusted manually from the software. Confocal imaging was performed using a 488 nm continuous air-cooled argon ion laser (Coherent UK LTD, UK) and an APD detector (Perkin-Elmer Optoelectronics, France) with green fluorescence emission in the spectral region. A Labview data acquisition software written by Joshua B. Edel was used for FCS experiments.

5.3.2 Device preparation

A microfluidic PDMS chip with a channel dimension of 6 mm x 75 μm x 75 μm was bonded onto a 160 μm thick microscope cover slip. Initially the surface of the PDMS chip and the cover slip were sonicated in ethanol for 15 min, dried with N_2, and exposed to O_2 plasma for about 30 seconds prior to bonding. The chip was then placed on a hot plate at 65 ºC to ensure strong bonding. Upon the bonding, it was mounted onto the transitional stage of the microscope, the inlet of the channel connected to the syringe pump, and the outlet to a vial. Gas-tight syringes were used in the experiments presented in this section, unless stated otherwise.

5.3.3 DNA labelling with YOYO

YOYO-1 (1,1'-(4,4,7,7-tetramethyl-4,7-diazaundecamethylene)-bis-4-[3-methyl-2,3-dihydro-(benzo-1,3-oxazole)-2-methylidene]-quinolinium tetraiodide) is one of the most commonly used fluorescent probes. It intercalates with dsDNA and upon binding a strong fluorescence enhancement is observed on account of its high association constant **(19, 20)**. It has also been reported that the YOYO-1/DNA complex is very stable and has a higher binding affinity compared to other fluorophores such as ethidium bromide or acridine orange **(21)**. In addition, the complex has the highest quantum yield and high SNR. Although the observed fluorescence enhancement is slightly lower than that of another fluorophore/DNA complex (TOTO-1/DNA), absorption and emission wavelengths of this complex are not compatible with commercial fluorescence filters, making it an undesirable choice of dye (absorption at 514 nm, emission at 533 nm). The absorption and emission wavelengths of YOYO-1/DNA complex are 491 nm and 509 nm respectively and are within the detection capability of the filters used.

Experimentally, λ-DNA was stained with YOYO-1 at 5:1 base-pair:dye ratio. A 3 μl solution of 1 mM YOYO-1 iodide was mixed with 10 μl of 15.5 nM λ-DNA stock solution and incubated at room temperature for approximately 20 min. The mixture was diluted to 1 ml to give a concentration of 155 pM and 15.5 pM DNA/YOYO complex.

5.4 Velocity measurements of flow-induced molecule migration

The speed of flow-induced particle migration has been studied via various techniques for almost a century. Early studies include the use of Pitot-static tubes and hot-wire anemometers; however both are invasive methods which require the insertion of a physical probe into the flow stream. With the invention of the laser, a non-invasive method was introduced; laser-probed Doppler anemometer, but this requires sophisticated electronics and optics making it an undesirable choice for velocity measurements. Other non-invasive techniques based on instantaneous optical particle tracking have been developed; particle image velocimetry (PIV), which measures the distance between two successive burst of light, producing two images in the

same image frame **(22)**. Also recent advances in optical imaging have paved the way for single-molecule detection in flowing samples with increased sensitivity and reduced detection volumes such as laser-induced fluorescence reported by Keller *et al* **(23, 24)**. In a similar manner, the combination of confocal detection with fluorescence correlation spectroscopy (FCS) provides highly sensitive flow velocity measurements based on single-molecule detection **(25)**. FCS is a well-established technique that enables the study of reaction kinetics and dynamics related to rotational diffusion, translational diffusion and flow velocities of molecules.

In this study, the velocity measurements were carried out using two different methods; optical tracking of the molecules by wide-field fluorescence imaging, and confocal detection incorporated with FCS.

5.4.1 Velocity measurements by wide-field imaging

The velocity profile of the fluid flow in a rectangular channel is parabolic[39]. However one can simply estimate the averaged velocity of the flowing molecule from its relation to the volumetric flow rate, as represented in Equation 5.4;

$$V_L = \frac{Q}{A_c} \qquad \text{Equation 5.4}$$

where V_L is the average linear velocity (m/s), Q is the volumetric flow rate (m^3/s), and A_c is the cross-sectional area of channel. Experimentally, the velocity of the molecule can be measured by tracking the movements of the molecule in consecutive video frames that are recorded using wide-field fluorescence microscopy. It is important to note that three dimensional velocity profile can also be mapped out, provided that the position of the molecule of interest is well-defined and matched with the findings.

We initially measured the velocity of the DNA molecules at a variety of flow rates accordingly and compared the experimental findings to the theoretical V_L, calculated from Equation 5.4. The flow rates were varied between 0.02 µl/min and 0.1 µl/min, and the

[39] It will be discussed in more detail CHAPTER 6.

measurements were taken from a position that is at least 15 μm away from the channel walls so that the best resolution is achieved and the error arising from averaging is minimized. The results are shown in Figure 5.6.

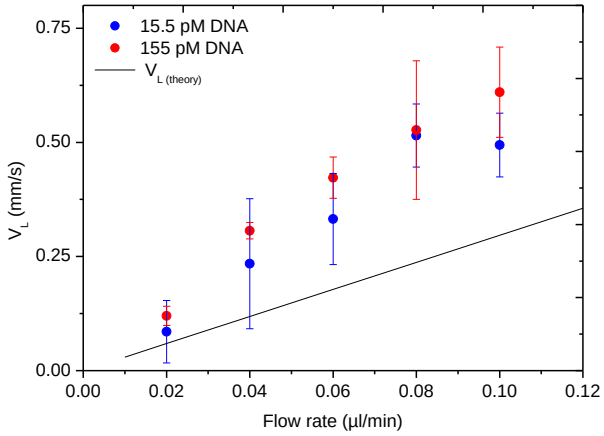

Figure 5.6 Velocities obtained using wide-field FM imaging. Blue: C_{DNA} = 15.5 pM, red: C_{DNA} = 155 pM, black line: Theoretical linear flow velocity ($V_{L(theory)}$) calculated from Equation 5.4.

The findings indicate that the experimental results agree with $V_{L(theory)}$ at slow flow rates (e.g. 0.02 μl/min) while it becomes faster than $V_{L(theory)}$ at relatively high flow rates (e.g. 46% faster at 0.08 μl/min and 60% faster at 0.1 μl/min, C_{DNA} = 155 pM). Furthermore, the results for the velocity of different DNA concentrations did not differ considerably, which might have been the case on account of increased electrostatic interactions and potential conformational changes in crowded media for concentrated DNA samples. It is highly likely that the deviation in V_L for each particular flow rate is related to averaging the velocities at different regions of the channel where the parabolic flow profile is still present.

5.4.2 Velocity measurements by fluorescence correlation spectroscopy

The employment of FCS in co-operation with confocal detection provides a more accurate way of determining the flow velocities. FCS was first introduced in 1970's **(26, 27)**. However applications of FCS in flowing systems was first shown theoretically and then experimentally by

Magde *et al* 1978 **(28)**. Its applications in microfluidic channels have been shown by various researchers later **(25, 29-31)**.

The idea is that when fluorescently labelled molecules pass through a detection/probe volume defined by the laser beam, stochastic fluorescence bursts are detected and recorded over time [40]. Burst analysis is performed by using photon counting histograms (PCH) where the distribution of the number of photons in each burst is defined statistically. FCS is employed for further statistical analysis of the bursts in order to understand the primary source of the concentration fluctuations.

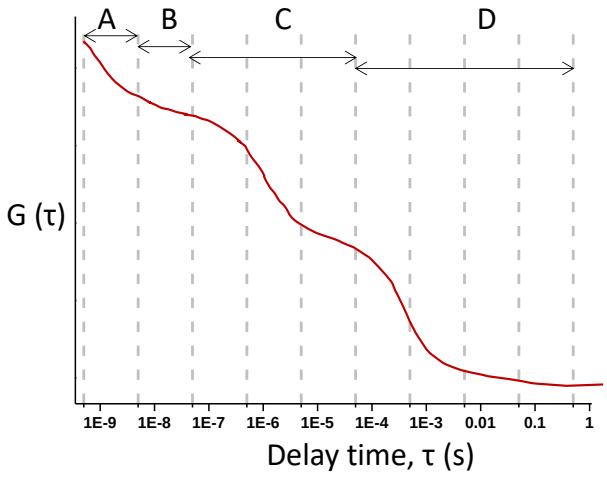

Figure 5.7 Diagram of the possible temporal changes of the process that affect the single molecule autocorrelation data. Labelling scheme refers to different temporal changes (A; rotation/and antibunching, B; intermolecular processes, C; triplet formation, D; diffusion). Reproduced from (32).

FCS measures the self-similarity of the fluctuations in a time scale by comparing the signal with itself at a time of t and after a delay time of τ. The normalized fluorescence correlation function can be written as;

$$G(\tau) = \frac{\langle \delta I(t) \delta I(t+\tau) \rangle}{\langle I(t) \rangle^2} \qquad \text{Equation 5.5}$$

[40] Concentration fluctuations, within the probe volume, are modulated by diffusion, chemical reactions or conformational changes and this leads to the deviations from mean signal intensity and burst width.

where δI(t) and δI(t+τ) are the amplitudes of the fluctuations from the mean at time t and t+τ, respectively, and <I(t)> is the mean of the signal.

A variety of physical mechanisms might influence FCS. The principle contribution arises from diffusion with a time scale longer than 10^{-5} seconds. Other sources (some of them is illustrated in Figure 5.7), include triplet crossing, intermolecular processes, rotational diffusion, photobleaching and flow **(32)**. In order to reveal the time scales of contributing processes, the function has to be fit to a relevant theoretical model. For a system where diffusion dominates the fluctuations, a 3D *diffusion* model for the autocorrelation functions is given by Equation 5.6;

$$G(\tau)_{diff} = 1 + \left(\frac{1}{N}\right) A \qquad \text{Equation 5.6}$$

where N is the mean number of particles in the probe volume and A;

$$A = \left(1 + \frac{\tau}{\tau_{diff}}\right)^{-1} \left(1 + \frac{\tau}{\gamma^2 \tau_{diff}}\right)^{-1/2} \qquad \text{Equation 5.7}$$

where τ_{diff} is the average diffusion time (or correlation time) and γ is called '*structure factor*'. τ_{diff} is given by Equation 5.8;

$$\tau_{diff} = \frac{w_0^2}{4D} \qquad \text{Equation 5.8}$$

and γ is defined by Equation 5.9;

$$\gamma = \frac{w_0}{z_0} \qquad \text{Equation 5.9}$$

where w_0 is the laser beam waist ($1/e^2$ radii of the laser beam), D is the translational diffusion coefficient and z_0 is the probe depth.

In a flowing system, a theoretical 3D fit to the autocorrelation function is given by Equation 5.10 **(25, 28, 29)**;

$$G(\tau)_{diff+flow} = 1 + \frac{1}{N} A exp\left\{(\frac{\tau}{\tau_{flow}})^2 A\right\}$$ Equation 5.10

where τ_{flow} is the average flow time of the molecules through the probe volume. By using τ_{flow} deduced from the experimental data, the flow velocity is calculated by Equation 5.11;

$$V_{flow} = \frac{w_0}{\tau_{flow}}$$ Equation 5.11

5.4.3 Time trace analysis

FCS is best performed when SNR is sufficiently high. There are couple of factors affecting SNR, including sample concentration, intensity changes in the laser light sources, QY of the dye-molecule complex and detector efficiency. As for the sample concentration, one has to confirm that only a single molecule is present in the probe volume. For a 1 nM sample concentration the volume occupancy is 0.6 molecules per 1 fl volume. The number of fluorophores in the volume is described by the Poisson distribution, where the probability is around 0.33 for one, 0.10 for two molecules **(2)**, approaching to 0.55 when the volume does not contain any molecule. In more dilute samples; SNR becomes highly sufficient for single molecule detection as the probability for two or more molecules in the volume drops to almost zero **(33)**.

In order to determine the optimal working conditions for single molecule detection and higher SNR, 3 sets of experiments with 2 different concentrations of DNA and salt solution were carried out; 155 pM and 15.5 pM λ-DNA in 10 mM KCl, and 15.5 pM λ-DNA in 1 M KCl. Flow rate was varied between 0 µl/min and 2 µl/min. The time traces were collected with 50 µs resolution and re-sampled with 200 µs resolution. Real-time autocorrelation curves were generated every 500 milliseconds (N = 50000) within a 60 seconds recording time using the normalized autocorrelation equation.

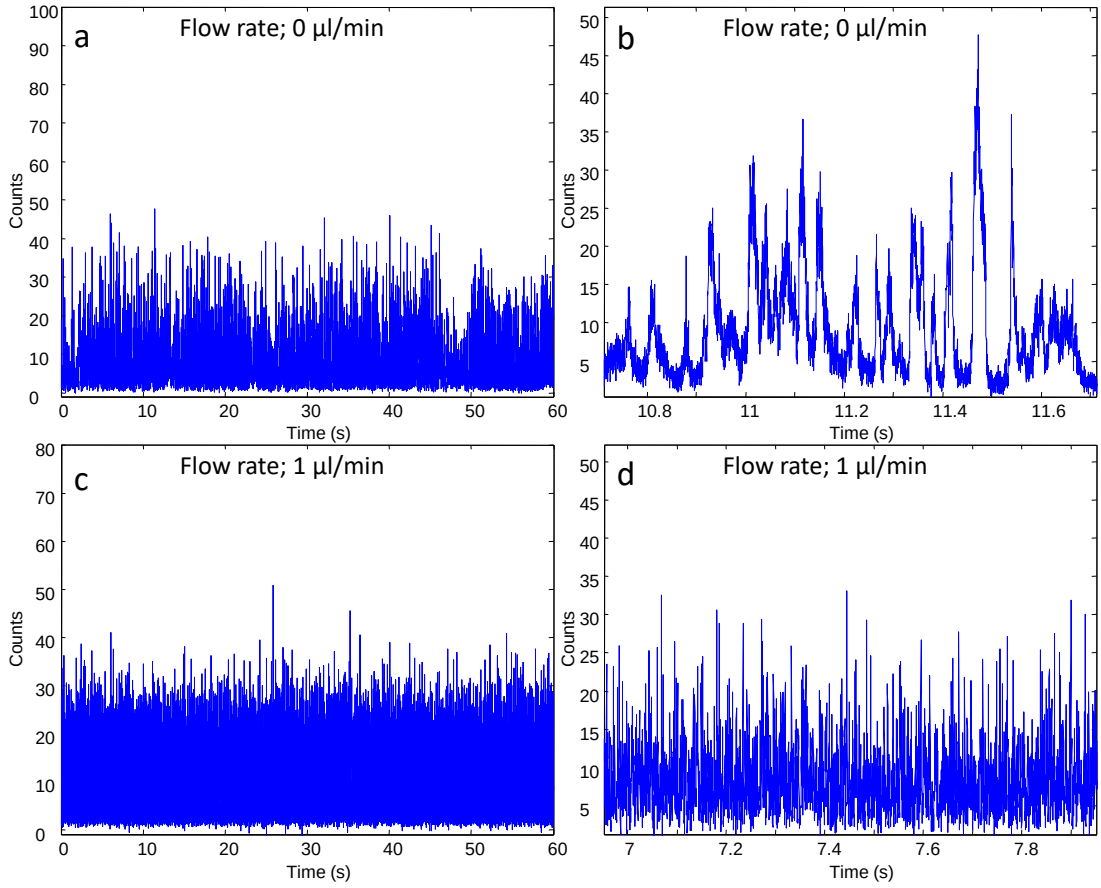

Figure 5.8 Representative single-molecule fluorescence burst scans of 155 pM DNA-YOYO complex in 10 mM KCl. a. 60 seconds time trace at 0 µl/min. b. Expanded 1 second time trace of panel 'a'. c. 60 seconds time trace at 1 µl/min. d. Expanded 1 second time trace of panel 'c'.

Figure 5.8 and Figure 5.9 show several time traces of fluorescent burst scans recorded using 155 pM and 15.5 pM complex solution in 10 mM KCl at different flow rates (e.g. 0, 0.3, and 1 µl/min), respectively. The SNR increased significantly from almost 8 to 80 when a 10x diluted complex solution was used. It is a consequence of the low volume occupancy. For a 1 fL volume, it is expected that the probe volume contains an average of 0.1 molecules for 155 pM and 0.01 for 15.5 pM, where the probability of detecting discrete events is higher.

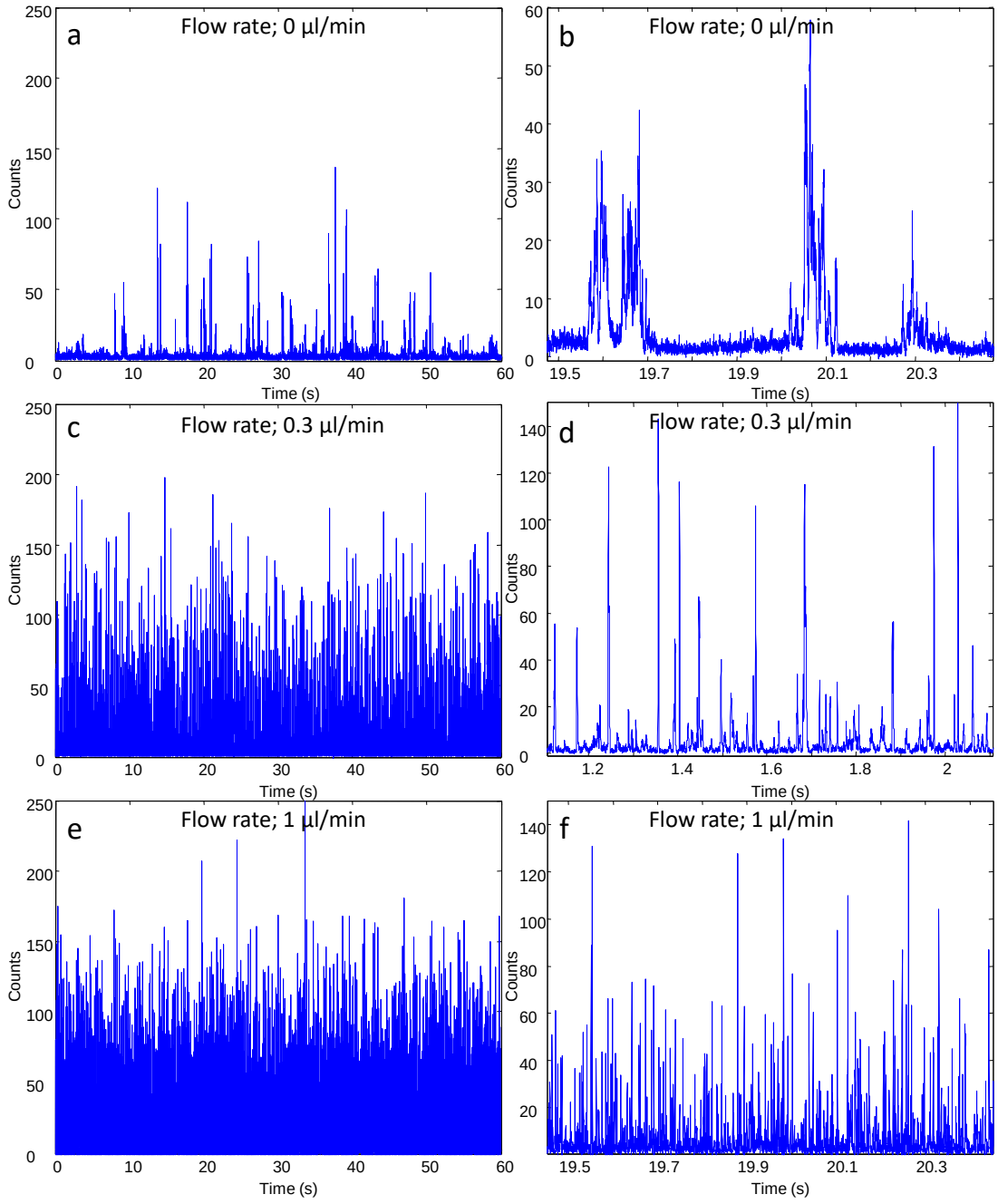

Figure 5.9 Representative single-molecule fluorescence burst scans of 15.5 pM DNA-YOYO complex in 10 mM KCl. a. 60 seconds time trace at 0 µl/min. b. Expanded 1 second time trace of panel 'a'. c. 60 seconds time trace at 0.3 µl/min. d. Expanded 1 second time trace of panel 'c'. e. 60 seconds time trace at 1 µl/min. f. Expanded 1 second time trace of panel 'e'.

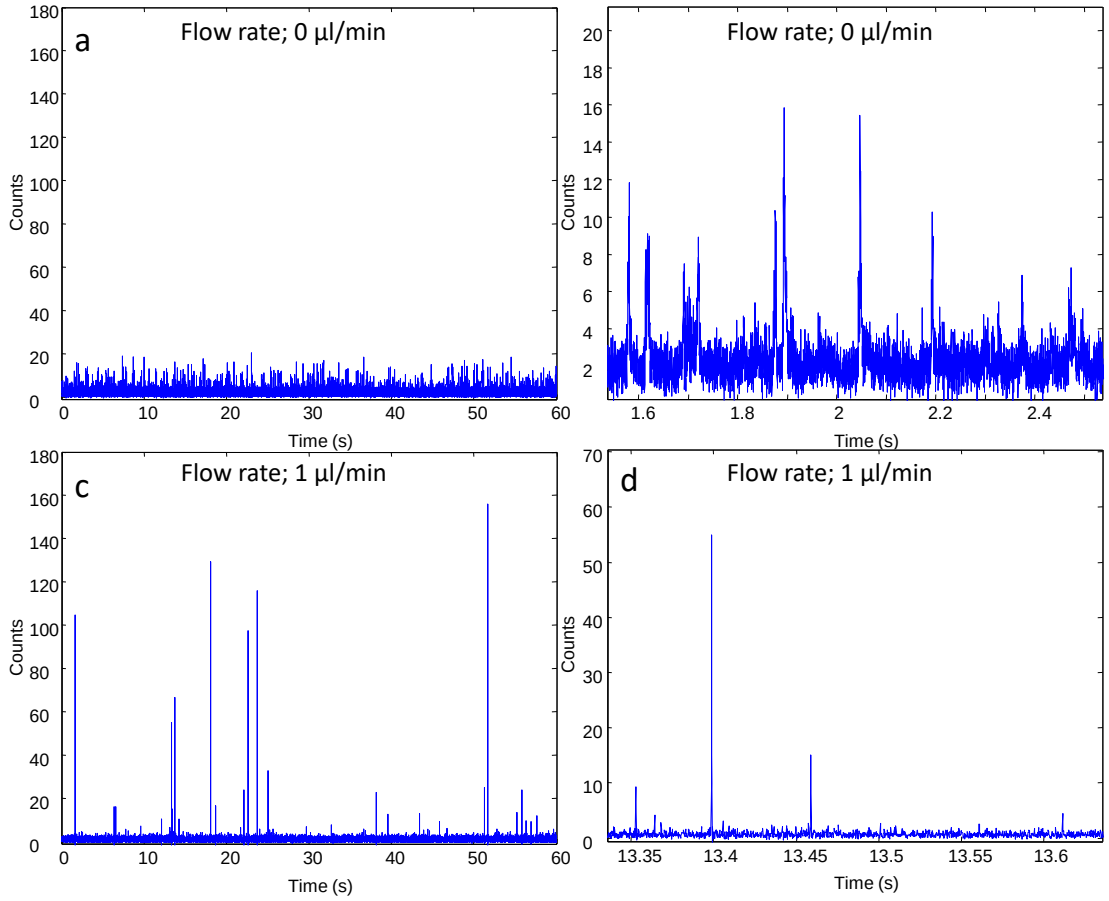

Figure 5.10 Representative single-molecule fluorescence burst scans of 15.5 pM DNA-YOYO complex in 1 M KCl. a. 60 seconds time trace at 0 µl/min. b. Expanded 2 seconds time trace of panel 'a'. c. 60 seconds time trace at 1 µl/min. d. Expanded 2 seconds time trace of panel 'c'.

The effect of salt concentration on the fluorescence signal intensity was also studied, as shown in Figure 5.10. For a 15.5 pM DNA solution, the SNR dropped to 5 at flow rate of 0 µl/min when using a 1M KCl buffer. At 1 µl/min, there was a significant decrease in the number of fluorescent bursts although SNR did not change significantly from that in 10mM KCl, as shown in Figure 5.9. Salt effect is a consequence of quenching of YOYO in high concentration of chloride ions.

Therefore, FCS studies were focused on the data obtained with 15.5 pM sample concentration in 10 mM KCl. Figure 5.11 shows the autocorrelation curves obtained from the burst scans at flow rates between 0 µl/min and 2 µl/min. An immediate observation is that there is a clear shift in the full width half maxima (FWHM) from right to left in the time scale. It can

also be seen that the amplitude of G(τ) increases with increasing flow rate. Unfortunately, the data collected at flow rates above 0.3 µl/min was truncated. Nonetheless, the data does not appear to contradict the trends just stated. FWHM calculated from the relevant fits to the autocorrelation curves corresponds to the related time scales such as τ_{diff} or τ_{flow}, whereas G(τ) at τ = 0 represents the occupancy of the probe volume; namely the number of molecules occupying the probe volume at a time.

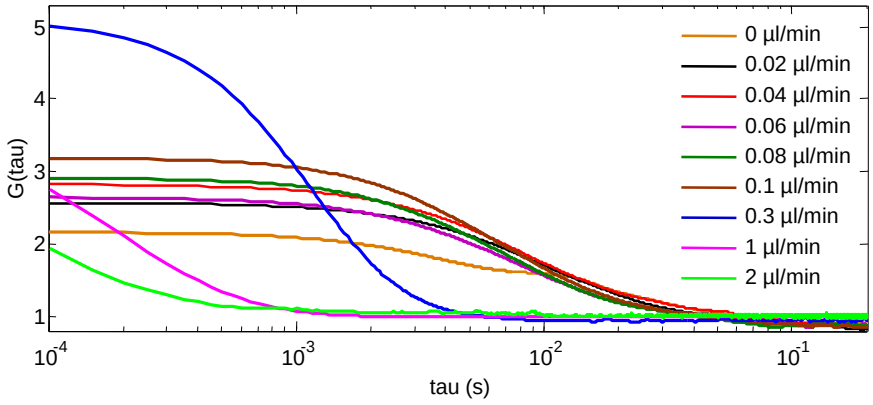

Figure 5.11 Autocorrelation curves of 15.5 pM sample solution for different flow rates.

The physical meaning of the data can be studied quantitatively by fitting the curves with a relevant model, as described earlier. The autocorrelation curve obtained in the absence of flow was fitted with the 3D *diffusion* model, Equation 5.6, and the others with the 3D *diffusion+flow* model, Equation 5.10. The value for τ_{diff} deduced from the fit of the 3D *diffusion* model to the data collected under no flow was then fixed when fitting the data collected under flow and τ_{flow} determined for each flow rate. This approach has the advantage of providing a means of determining the diffusion- and flow-limited regimes in a flowing system.

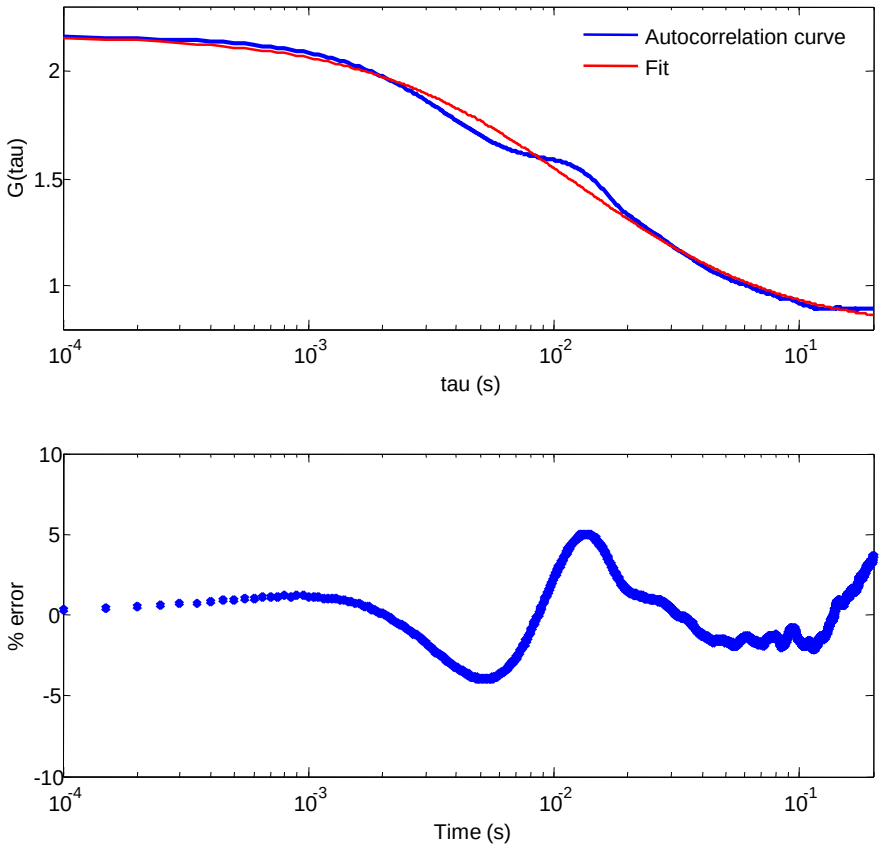

Figure 5.12 Autocorrelation curve and the fit for 0 µl/min flow rate (blue and red, respectively). The fitting function is the 3D *diffusion* model.

Figure 5.12 shows the autocorrelation curve of 0 µl/min flow rate fitted by the 3D *diffusion* model and the error analysis (top and bottom panel, respectively). Although there seems to be a second unknown component in the autocorrelation curve, the curve could be fitted with less than 2% error. This second component might arise from the kinetics of conformational changes of DNA since DNA is a mobile structure, unlike a nanoparticle, that diffuses in and out of the probe volume with more fluctuations due to its chain flexibility **(34)**. Another possible reason for this might simply be due to the absorption of DNA complex onto the cover slip or the reflection of free-YOYO adsorption to the PDMS, which was experimentally observed by wide-field imaging.

The fit yields a τ_{diff} value of 12.5 ms. Using Equation 5.8, the experimental diffusion coefficient of DNA (D_{DNA}) can also be calculated and compared to literature for further validation.

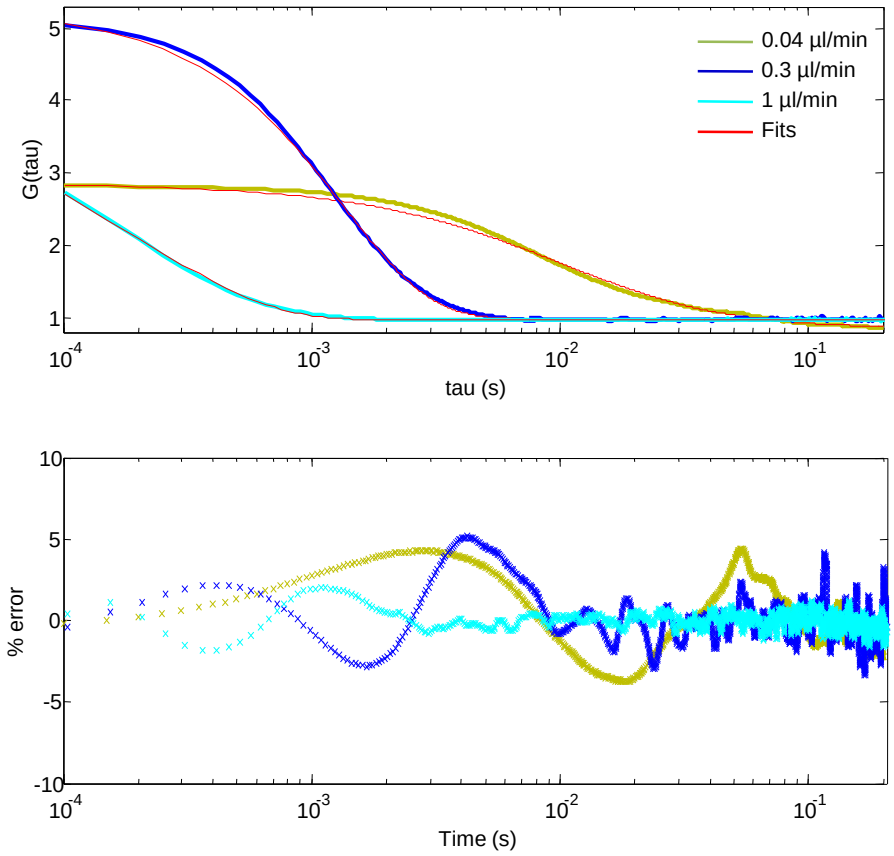

Figure 5.13 Autocorrelation curves of 15.5 pM sample solution for selected flow rates.

To calculate w_0, the autocorrelation curve of a dye with a well-known diffusion coefficient is investigated, and τ_{diff} and w_0 are found accordingly, using Equation 5.6, Equation 5.7 and Equation 5.8. It was measured to be 568 nm by William Pitchford and this yields D_{DNA} to be 6.45 x 10^{-12} m^2/s, which is in good agreement with the literature (Smith *et al* reports that the self-diffusion coefficient of a single is 0.47 x 10^{-12} m^2/s for λ-DNA **(35)**). Using the calculated τ_{diff}, the 3D *diffusion+flow* model (Equation 5.10) was fit to the autocorrelation functions obtained under different flow rates. Several examples along with the fits (i.e. 0.04 µl/min, 0.3 µl/min and 1 µl/min) and the relevant error analysis (top and bottom panel, respectively) are shown in Figure 5.13. The second component that was observed at 0 µl/min flow rate is not discernable with the increased flow rate and each autocorrelation function was fit with less than 5% error.

The values of τ_{flow} extracted at each flow rate are plotted in Figure 5.14a. An interesting observation is that τ_{flow} decreased more than 100 times with increasing flow rate before reaching a

plateau at a flow rate of 0.3 µl/min where it was 10 times smaller in magnitude than τ_{diff}. When τ_{diff} becomes greater than τ_{flow}, the system is no longer diffusion-limited, rather flow-limited **(30)**. Therefore the above result is an indication of the flow-limited regime at 0.3 µl/min flow rate. The determination of this regime is of great importance to the nanopore-based electrochemical detection of DNA in flow[41].

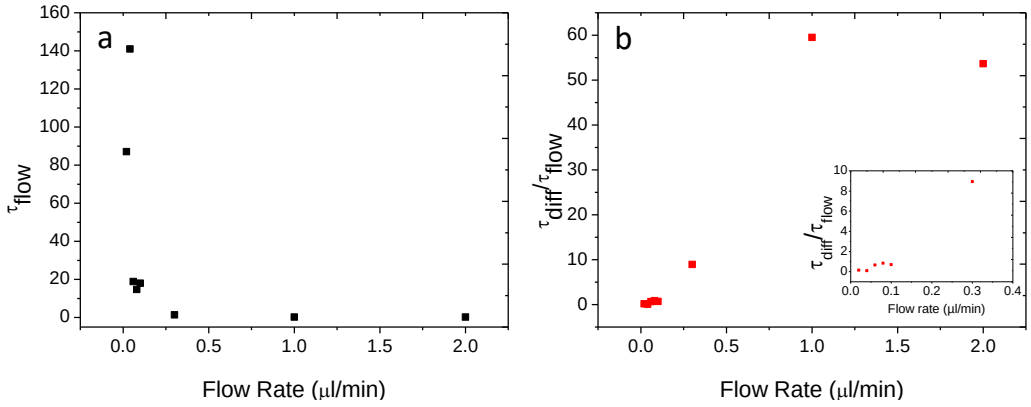

Figure 5.14 Flow rate versus τ. a. τ_{flow} versus flow rate. b. τ_{diff}/τ_{flow} versus flow rate.

Using Equation 5.11, the experimental flow velocity (V_{flow}) was calculated and plotted in Figure 5.15. It seems that V_{flow} was similar to the linear flow velocity within the microfluidic channel as calculated from Equation 5.4 using Q_{flow}. For example, V_{flow} was 4.03 mm/s at a flow

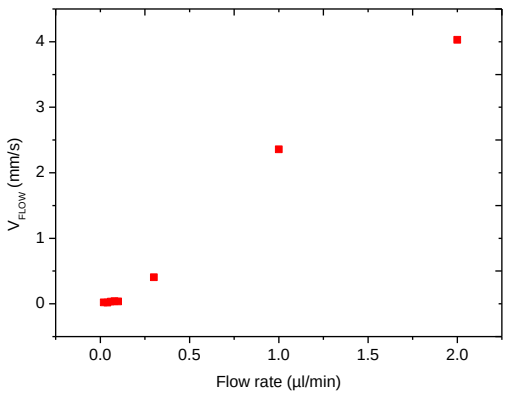

Figure 5.15 Flow rate versus flow velocity.

[41] Further discussion is presented in CHAPTER 6.

rate of 1 µl/min which is comparable to Q_{flow} (5.93 mm/s). The discrepancy is probably a consequence of a parabolic velocity profile. Equation 5.4 assumes that both sheath flow and analyte flow contributes to Q_{flow} and it is uniformly distributed within the microfluidic channel **(36)**. In fact, the hydrodynamic flow profile in microfluidic channels is not uniform and posses a parabolic flow profile[42]. For instance, Gösch *et al* states that the velocity profile in a 50 µm channel differs from 18 mm/s to 2 mm/s in the centre and near the wall, respectively, at a flow rate of 15 mm/s **(29)**. The focal plane in the experiments discussed above is predicted to be located in the centre of the channel; however there is still possibility that the positioning is off-centred. As a result, the velocity difference is expected, but occurs within a reasonable estimate.

5.5 Investigation of DNA behaviour under flow

The conformational dynamics and rheological properties of flexible polymers like DNA under various types of flow (e.g uniform, extensional, shear, mixed) have been studied extensively **(37-39)**. It is well-known that if there is no external force impinging on the molecule, the molecule stays in its relaxed coiled state. However, in the presence of flow, the molecule undergoes several conformational distortions in its chain due to the force balance between Brownian or elastic coiling forces and stretching drag forces **(40-42)**. The stretching drag force resulting from flow velocity and the reducing hydrodynamic interactions as the molecule uncoils results in the molecule becoming elongated with increasing flow velocity.

The transition from a coiled to elongated state is expected to be different depending on the velocity gradient and flow type. In shear flow, the molecule experiences 2 steps of distortions as opposed to a sharp transition in extensional flow **(43)**;

- ***For slow flow velocities;*** the relative distortions are proportional to the relaxation time of the molecule.
- ***For larger flow velocities;*** two states are possible depending on the magnitude of the flow rate. An intermediate state is observed at relatively lower flow velocity, where

[42] Flow profile is presented in detail in CHAPTER 6.

elongation is saturated as the molecule maintains a partially coiled state. At very high flow velocities, hydrodynamic interactions between DNA base-pairs are decreased sufficiently and the molecule becomes fully elongated.

The degree of the elongation can be determined by a dimensionless number called the '*Weissenberg number*' (Wi). Wi is the product of the shear rate and the relaxation time of the molecule in question, as illustrated in Equation 5.12;

$$Wi = \dot{\gamma}\xi \qquad \text{Equation 5.12}$$

where $\dot{\gamma}$ is the shear rate and ξ is the longest relaxation time. The shear rate is a function of the velocity gradient and given by Equation 5.13;

$$\dot{\gamma} = \frac{dV}{dx} \qquad \text{Equation 5.13}$$

It is clear that the higher the Wi the higher the elongation because of increased shear rate in the function. Unfortunately, determining a precise Wi value for the transition from a coiled to elongated state is not trivial because of the complexity of the modelling.

In one theoretical study, Chen *et al* reported that elongation is only expected when Wi >> 1 **(44)**. At lower Wi, the flow would not create a sufficient force to deform the molecule from its relaxed state. With a modest approximation, Larson *et al* suggested that the transition occurs at a critical value of Wi (0.275) in mixed shear and elongational flow **(42)**. These values differ due to the application of different flow and use of a different theoretical model. Smith et. al reported that the extension is much sharper in elongational flow compared to that in shear flow, and the probability distribution of extension in shear flow is very low at Wi < 2.5 **(45)**. For example, weak deformation from the coiled state in shear flow occurs at Wi = 1.3, $\dot{\gamma}$ = 0.2, corresponding to an extension of less than 5 μm for λ-DNA. Extension increases up to half of DNA contour length with a standard deviation of approximately 4 μm when Wi is increased to 76, $\dot{\gamma}$ = 4.0. Another essential point to be taken from this experiment is that the extension reaches an asymptotic plateau at almost half of the DNA contour length after Wi = 20.

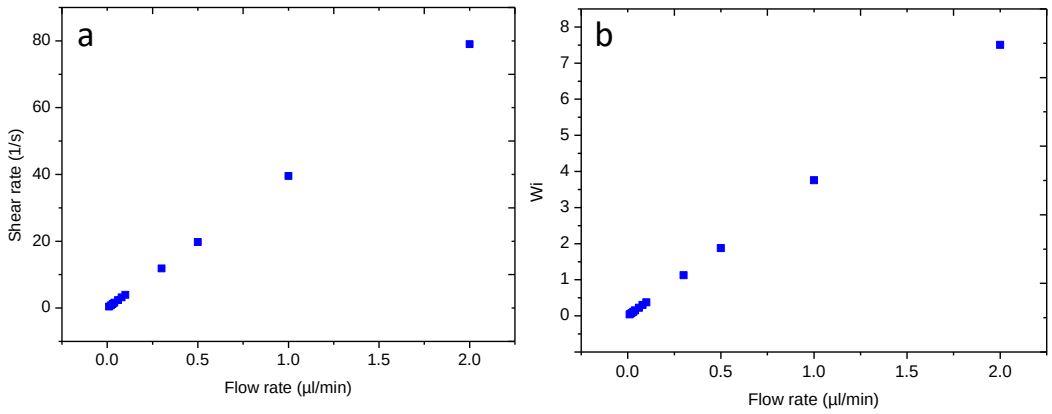

Figure 5.16 Shear rate and Wi versus flow rate varying between 0.02 µl/min and 2 µl/min (a and b, respectively).

In the light of these findings, the experimental shear rate and Wi was plotted versus flow rate in Figure 5.16. The longest relaxation time of λ-DNA is 0.095 s, the contour length is 21.2 µm when labelled with the dye and the gyration radius is 0.76 µm **(37, 44)**. Under these conditions, the extension is expected to occur at flow rates lower than 1 µl/min. In order to estimate the extension rate, single molecule image frames captured by the EMCCD camera was used and acquired in ImageJ. The distance between the one end of the molecule and the other end was calculated in pixels and converted to metric scale. Due to the high speed of the fluid over 0.3 µl/min, the measurements were only taken between 0.02 µl/min and 0.1 µl/min.

In Figure 5.17, the top panel shows a 3D surface plot of a single DNA molecule travelling in the microfluidic channel at a flow rate of 0.02 µl/min (Wi = 0.1). On the right hand side of the top panel, images are shown of DNA for repeat experiments using the same conditions. These images suggest that low flow rates used results in a relatively broad distribution in DNA conformation. The DNA end-to-end length is 7.3 µm in Figure 5.17a, while it is almost coiled up (measured length is 2.4 µm) in Figure 5.17b. Furthermore a partially stretched state with an extension length of 3.5 µm is shown in Figure 5.17c. When the flow rate was increased to 0.1 µl/min (Wi = 0.4), DNA is observed to reach an end-to-end length of 12.4 µm, as shown in Figure 5.17d. However, there has to be a correction factor added to these calculations because of

the fact that the smearing of the molecule is observed in consecutive frames (the end position of the molecule becomes the initial position in the next frame) when the flow rate is above 0.1 µl/min. The smearing artefact is likely a product of the limited temporal resolution of the camera

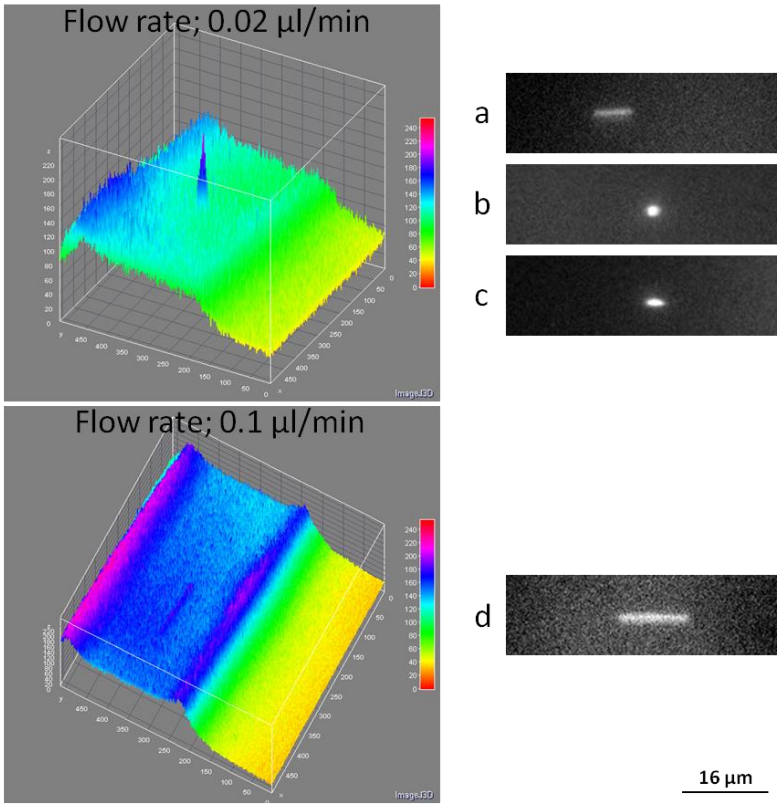

Figure 5.17 Fluorescence images of single λ-DNA molecules at different flow rates. Top left: 3D surface plot of a single DNA molecule at a flow rate of 0.02 µl/min. a. b. c. Examples of a partially stretched single DNA molecule (0.02 µl/min). Bottom left: 3D surface plot of a single DNA molecule at a flow rate of 0.1 µl/min. d. Example of a stretched single DNA molecule (0.1 µl/min). (15.5 pM DNA concentration in 1 M KCl, 10 mM Tris HCl and 1 mM EDTA).

used with respect to the DNA velocity. Ideally, shorter exposure times would be used. The correction factor is calculated from the distance that the fluid moves within the time period of the frame rate (30 ms) and subtracted from the measured DNA length. The mean fractional extension with the correction factor is plotted against flow rate in Figure 5.18. Mean fractional extension (MFE) is defined by;

$$MFE = \frac{\langle x \rangle}{L_c} \qquad \text{Equation 5.14}$$

where $\langle x \rangle$ is the mean extension and L_c is the DNA contour length. At a flow rate of 0.1 µl/min (Wi = 0.38), MFE reaches a value of 0.21 and 0.43 for 15.5 pM and 155 pM DNA concentration, respectively.

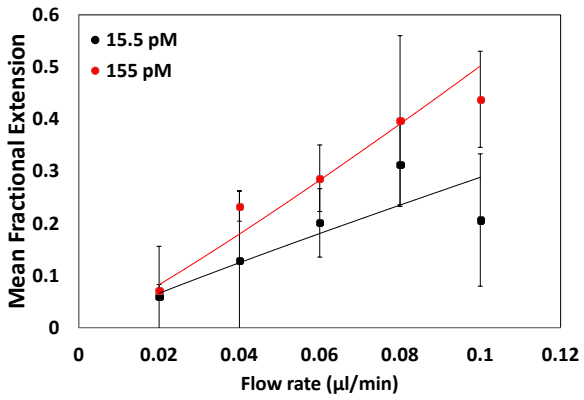

Figure 5.18 Mean fractional extension versus flow rate and Wi for 2 different DNA concentration (e.g. 15.5 pM and 155 pM DNA).

This is in contrast to the findings reported by Smith *et al*;~0.4 - 0.5 at Wi < 20, and slightly higher than the literature. The discrepancy might arise from the differences in the experimental conditions such as buffer concentration. It is also important to remember that the position of the focal plane might be slightly off-centred. This would eventually cause deviations from the expectations due to the differences in the local shear rate, and thus in the elongation rate.

5.6 Conclusion

In this chapter, flow velocity and DNA behaviour in flow was explored using optical techniques including wide-field FM and confocal FM. Velocity measurements resulted in good agreement with the expected flow velocity. Confocal FM studies co-operated with FCS revealed the determination of diffusion- and flow-limited regimes, which suggests that the system becomes flow-limited at a flow rate of 0.3 µl/min. In wide-field imaging experiments it was observed that DNA partially elongates to almost half of its counter length at a flow rate of 0.1 µl/min. However the elongation rate varies across the channel because it is a dependant variable on the velocity and the local shear rate, which differ across the channel. Therefore the elongation

rate is expected to be different near the wall, where the nanopore is positioned, as will be discussed in the next chapter. Another experimental observation was that slower flow rates (e.g. 0.1 μl/min) caused a backlash in some experiments; this is perhaps due to the limitations of the pump and the friction of the tubing. This may have been a source of the differences in extension observed for repeats at low flow rates.

References

1. Lichtman JW, Conchello JA. Fluorescence Microscopy. Nat Methods. 2005;2(12):910-9.

2. Lakowicz JR. Principles of Fluorescence Microscopy. Third ed. Baltimore, Maryland, USA: Springer; 2006.

3. Miles BN, Ivanov AP, Wilson KA, Dogan F, Japrung D, Edel JB. Single Molecule Sensing with Solid-State Nanopores: Novel Materials, Methods, and Applications. Chemical Society Reviews. 2012.

4. Coling D, Kachar B. Principles and Application of Fluorescence Microscopy. Current Protocols in Molecular Biology: John Wiley & Sons, Inc.; 2001.

5. Abramowitz M, Spring KR, Keller HE, Davidson MW. Basic Principles of Microscope Objectives. Biotechniques. 2002;33(4):772-781.

6. Jerome WGJ, Price RL, Jerome WG. Basic Confocal Microscopy2011. 1-302 p.

7. Dautet H, Deschamps P, Dion B, MacGregor AD, MacSween D, McIntyre RJ, et al. Photon Counting Techniques with Silicon Avalanche Photodiodes. Appl Opt. 1993;32(21):3894-900.

8. Burkhardt M, Schwille P. Electron Multiplying Ccd Based Detection for Spatially Resolved Fluorescence Correlation Spectroscopy. Opt Express. 2006;14(12):5013-20.

9. Zakharov Y, Dudenkova V, Bezrukov D, Legrand F, editors. Ultra Low Noise Emccd Camera Considered to Test a Novel Superresolution Microscopy Technique: The 3-B Technique2013: Optical Society of America.

10. Introduction to Confocal Laser Scanning Microscopy [Internet]. Leica.

11. Education MTsfM. Fluorescence Microscopy [30.11.2013]. Available from: http://www.microscopyu.com/articles/optics/.

12. Dahm R. Discovering DNA: Friedrich Miescher and the Early Years of Nucleic Acid Research. Hum Genet. 2008;122(6):565-81.

13. Watson JD, Crick FHC. Molecular Structure of Nucleic Acids: A Structure for Deoxyribose Nucleic Acid. Nature. 1953;171(4356):737-8.

14. Pray LA. Discovery of DNA Structure and Function: Watson and Crick. 2008.

15. **Salieb-Beugelaar GB, Dorfman KD, van den Berg A, Eijkel JCT**. Electrophoretic Separation of DNA in Gels and Nanostructures. Lab on a Chip. 2009;9(17):2508-23.

16. Manning GS. A Procedure for Extracting Persistence Lengths from Light-Scattering Data on Intermediate Molecular Weight DNA. Biopolymers. 1981;20(8):1751-5.

17. **Chen P, Gu J, Brandin E, Kim Y, Wang Q, Branton D**. Probing Single DNA Molecule Transport Using Fabricated Nanopores. Nano Letters. 2004;4(11):2293-8.

18. **Edelstein A, Amodaj N, Hoover K, Vale R, Stuurman N**. Computer Control of Microscopes Using μmanager. Current Protocols in Molecular Biology: John Wiley & Sons, Inc.; 2001.

19. Glazer AN, Rye HS. Stable Dye-DNA Intercalation Complexes as Reagents for High-Sensitivity Flurorescence Detection. Nature. 1992;359(6398):859-61.

20. Günther K, Mertig M, Seidel R. Mechanical and Structural Properties of Yoyo-1 Complexed DNA. Nucleic Acids Research. 2010.

21. Gurrieri S, Wells KS, Johnson ID, Bustamante C. Direct Visualization of Individual DNA Molecules by Fluorescence Microscopy: Characterization of the Factors Affecting Signal/Background and Optimization of Imaging Conditions Using Yoyo. Analytical Biochemistry. 1997;249(1):44-53.

22. Prasad AK. Particle Image Velocimetry. CURRENT SCIENCE-BANGALORE-. 2000;79(1):51-60.

23. Dovichi NJ, Martin JC, Jett JH, Trkula M, Keller RA. Laser-Induced Fluorescence of Flowing Samples as an Approach to Single-Molecule Detection in Liquids. Analytical Chemistry. 1984;56(3):348-54.

24. Van Orden A, Cai H, Goodwin PM, Keller RA. Efficient Detection of Single DNA Fragments in Flowing Sample Streams by Two-Photon Fluorescence Excitation. Analytical Chemistry. 1999;71(11):2108-16.

25. Edel JB, Hill EK, de Mello AJ. Velocity Measurement of Particulate Flow in Microfluidic Channels Using Single Point Confocal Fluorescence Detection. Analyst. 2001;126(11):1953-7.

26. Magde D, Elson E, Webb WW. Thermodynamic Fluctuations in a Reacting System—Measurement by Fluorescence Correlation Spectroscopy. Physical Review Letters. 1972;29(11):705-8.

27. **Koppel DE, Axelrod D, Schlessinger J, Elson EL, Webb WW**. Dynamics of Fluorescence Marker Concentration as a Probe of Mobility. Biophysical Journal. 1976;16(2):A216-A.

28. Magde D, Webb WW, Elson EL. Fluorescence Correlation Spectroscopy. Iii. Uniform Translation and Laminar Flow. Biopolymers. 1978;17(2):361-76.

29. Gösch M, Blom H, Holm J, Heino T, Rigler R. Hydrodynamic Flow Profiling in Microchannel Structures by Single Molecule Fluorescence Correlation Spectroscopy. Analytical Chemistry. 2000;72(14):3260-5.

30. **Cecchini MP, Stapountzi MA, McComb DW, Albrecht T, Edel JB**. Flow-Based Autocorrelation Studies for the Detection and Investigation of Single-Particle Surface-Enhanced Resonance Raman Spectroscopic Events. Analytical Chemistry. 2011;83(4):1418-24.

31. **Kuricheti KK, Buschmann V, Weston KD**. Application of Fluorescence Correlation Spectroscopy for Velocity Imaging in Microfluidic Devices. Applied Spectroscopy. 2004;58(10):1180-6.

32. Gell C, Brockwell D, Smith A. Handbook of Single Molecule Fluorescence Spectroscopy: Oxford University Press New York; 2006.

33. **Nie SM, Chiu DT, Zare RN**. Real-Time Detection of Single-Molecules in Solution by Confocal Fluorescence Microscopy. Analytical Chemistry. 1995;67(17):2849-57.

34. **Chowdhury SA, Lim M**. Characterization of the Surface Contribution to Fluorescence Correlation Spectroscopy Measurements. Bulletin of the Korean Chemical Society. 2011;32(2):583-9.

35. Smith DE, Perkins TT, Chu S. Self-Diffusion of an Entangled DNA Molecule by Reptation. Physical Review Letters. 1995;75(22):4146-9.

36. Edel JB. Development of Single Molecule and Particle Detection Techniques for Microfluidic Analysis. London: Imperial College London; 2003.

37. Perkins TT, Smith DE, Larson RG, Chu S. Stretching of a Single Tethered Polymer in a Uniform-Flow. Science. 1995;268(5207):83-7.

38. **Perkins TT, Smith DE, Chu S**. Single Polymer Dynamics in an Elongational Flow. Science. 1997;276(5321):2016-21.

39. Duggal R, Pasquali M. Visualization of Individual DNA Molecules in a Small-Scale Coating Flow. Journal of Rheology. 2004;48(4):745-64.

40. Agarwal US. Effect of Initial Conformation, Flow Strength, and Hydrodynamic Interaction on Polymer Molecules in Extensional Flows. Journal of Chemical Physics. 2000;113(8):3397-403.

41. **Larson RG**. The Unravelling of a Polymer-Chain in a Strong Extensional Flow. Rheologica Acta. 1990;29(5):371-84.

42. **Larson RG, Magda JJ**. Coil-Stretch Transitions in Mixed Shear and Extensional Flows of Dilute Polymer Solutions. Macromolecules. 1989;22(7):3004-10.

43. Gennes PGD. Coil-Stretch Transition of Dilute Flexible Polymers under Ultrahigh Velocity Gradients. The Journal of chemical physics. 1974;60(12):5030-42.

44. Chen YL, Graham MD, de Pablo JJ, Jo K, Schwartz DC. DNA Molecules in Microfluidic Oscillatory Flow. Macromolecules. 2005;38(15):6680-7.

45. Smith DE, Babcock HP, Chu S. Single-Polymer Dynamics in Steady Shear Flow. Science. 1999;283(5408):1724-7.

CHAPTER 6
Electrochemical Detection of DNA in Flow

This chapter deals with in-flow electrochemical detection of single DNA molecules using a single nanopore integrated into a microfluidic channel. After a short discussion on the effect of hydrodynamic flow on DNA capture, experimental results are shown, which consists of the investigation of the effect of flow to the nanopore conductance, noise, and DNA translocation in the absence and the presence of flow.

As discussed previously in CHAPTER 1, diffusion-limited and energy barrier-limited regimes are used to describe the process of DNA capture in the absence of hydrodynamic flow. In flow, the molecules are forced to conform to flow through the microfluidic channel and therefore there is a need to apply further parameters for accurate modelling. An accurate representation of the DNA capture process in flow requires further consideration of coupling of its diffusive, electrostatic and hydrodynamic velocity components (e.g the diffusion velocity, the drift velocity, and the fluid velocity profiles) in three dimensions.

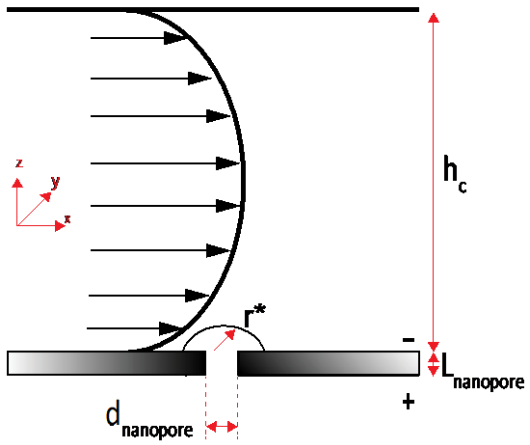

Figure 6.1 Schematic of the DNA capture through a nanopore embedded into a microfluidic channel in flow.

In the diffusion-limited regime, DNA capture is only affected by the diffusive flux in all directions and the fluid flow contribution in the x– direction. Whereas in the energy barrier-limited regime, convective forces are dominantly active, which themselves are influenced by the molecular transport in the z– direction due to electrophoretic forces, and the fluid flow in the x– direction. It is explicit that the capture can no longer be described by the aforementioned regimes with no consideration to flow but requires additional consideration of the superposition of the diffusion and convective fluxes in three dimensions. At low flow rates, the classic theory of capture rate can still be applied. However at high flow rates, the effect of the diffusive flux should be eliminated because molecular motion is streamlined by the increase in the convective forces in the x– direction. In addition, an intermediate level where interplay between diffusive and convective forces occurs is also feasible at medium flow rates. Furthermore, DNA loses its

relaxed state under certain degree of stress[43]. It is therefore considered that there is a need for physical description of the capture phenomena in flow covering all the velocity components, DNA conformational changes and time dependant variables such as relaxation time of the molecule; diffusion-limited regime, transitional regime from diffusion limited to flow limited regimes and flow-limited regime.

- ***Diffusion-limited regime;*** flow velocity is relatively small compared to drift velocity, meaning that the traditional nanopore capture concept **(1, 2)** is valid.
- ***Transitional regime;*** flow velocity becomes comparable to drift velocity. In this regime, the presumption is that a force balance between diffusive forces and convective forces governs DNA translocation. In terms of DNA conformation, flow starts to impose a hydrodynamic force on the molecule where DNA is not flexibly coiled up anymore and is partially coiled up. Degree of coiling and elongation can only be studied theoretically or using high-resolution optical instrumentation experimentally.
- ***Flow-limited regime;*** flow velocity is relatively large in comparison to drift velocity. This means that the molecule travels along the x- axis faster than its potential travel in the z- axis towards the nanopore. Perhaps there are two sub-regimes for flow-limited regime; one is that translocation still occurs, but translocation time and velocity is rather manipulated by the flow velocity and degree of DNA elongation and the other is where translocation stops due to high speed of the molecule in the x- direction.

As shown in CHAPTER 5, the flow-limited regime starts at 0.3 µl/min, however, in a planar nanopore-integrated microfluidic device like SiN/PDMS integration, the treatment of these regimes is not straight-forward due to the parabolic velocity profile of flow with no-slip boundary conditions. It is to say that the maximum fluid velocity is reached in the centre and lowers down to zero at the lateral sides of the channel with a velocity gradient of dV/dx due to the frictional forces **(3)**. In principle, the characteristics of the fluid flow through a long channel (e.g. axial velocity gradient (V(x, y)), pressure drop (ΔP) and the flow rate (Q)) are defined by the Hagen-

[43] See the text in CHAPTER 5.

Poiseuille equation. For the fluid flow through a rectangular channel, the equation can only be solved through the sum of a Fourier series. For example, in general, the velocity gradient across the channel can be expressed by Equation 6.1 **(4)**;

$$V(x,y) = \frac{\Delta P}{2\eta L_c}\left\{\left[\left(\frac{h_c}{2}\right)^2 - y^2\right] - \sum_{n=0}^{\infty} a_n \cos\left(\frac{\lambda_n y}{h_c/2}\right)\cosh\left(\frac{\lambda_n x}{h_c/2}\right)\right\} \quad \text{Equation 6.1}$$

where ΔP is the pressure difference, L_c and h_c are the length and the depth of microchannel, respectively, λ_n is expressed by Equation 6.2;

$$\lambda_n = \frac{(2n+1)\pi}{2} \quad \text{Equation 6.2}$$

and a_n is expressed by Equation 6.3 (no-slip boundary conditions and $x = \pm d_c/2$);

$$a_n = \frac{h_c^2(-1)^n}{(\lambda_n)^3 \cosh\left(\frac{\lambda_n d_c}{h_c}\right)} \quad \text{Equation 6.3}$$

where d_c is the width of the channel. The integration of the equation leads to the expression of the flow rate Q by Equation 6.4;

$$Q = \frac{w_c h_c^3 \Delta P}{2\eta L_C}\left[1 - 6\left(\frac{h_c}{w_c}\right)\sum_{n=0}^{\infty}(\lambda_n)^{-5}\tanh\left(\frac{\lambda_n w_c}{h_c}\right)\right] \quad \text{Equation 6.4}$$

A reasonable approximation can be made for different aspect ratios of the channel and produces less than 15% error for a channel of $h_c/w_c = 1$. A similar approach to solve the equation can also be found in reference **(5)**.

For simplicity, a simulation for a non-compressible, Newtonian, laminar[44] fluid flow was run using COMSOL Multiphysics®[45] so that the velocity gradient across the channel in our system (a 75 µm x 75 µm x 6 mm) could be visualised. Figure 6.2 illustrates the consequent flow profile at different flow rates ranging from 0.02 µl/min to 30 µm/min.

[44] In laminar flow, Reynolds number, which is the ratio of inertial forces to viscous forces, is less than 2000.
[45] The simulation was run by Benjamin Miles.

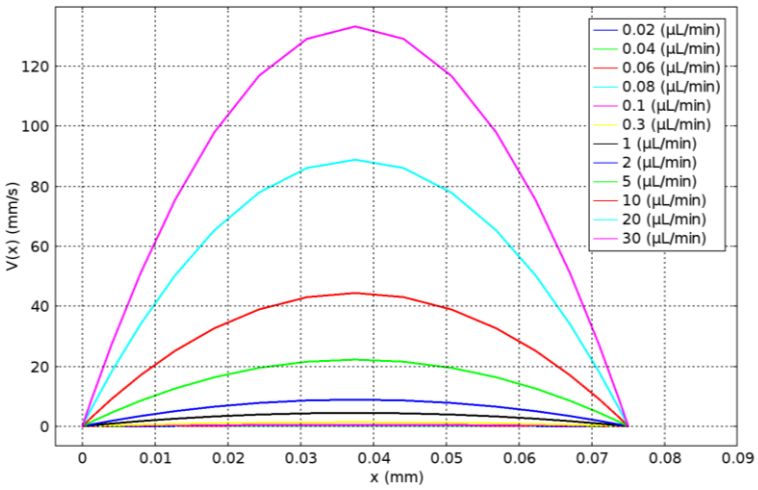

Figure 6.2 Flow velocity profile in a 75 µm x 75 µm x 6 mm microchannel, simulated using COMSOL Multiphysics®. Flow rates: 0.02, 0.04, 0.06, 0.08, 0.1, 0.3, 1, 2, 5, 10, 20, 30 µl/min.

Examining Figure 6.2, it can be seen that the flow develops a continuous fashion at flow rates higher than 0.3 µl/min. V(x) reaches a value of 3.5 mm/s and 133 mm/s at a flow rate of 30 µl/min at a distance of 500 nm away from the channel sides (namely nanopore capture zone) and at the centre of the channel, respectively, whereas it corresponds to a speed of less than 0.1 µm/s and approximately 1.5 µm/s at a flow rate of 0.3 µl/min, respectively. Nonetheless, Mala and Li **(6)** reported that flow profile deviates from the expectations at high Reynolds number, thus high flow rates (e.g. Re<500, corresponding to a fluid velocity of 83 mm/s). This means that the numbers given above might vary slightly for certain flow rates.

Recalling the effective nanopore capture distance and the drift velocity at the nanopore entrance (e.g. $\mu_{\lambda\text{-DNA}} = 3.73 \times 10^{-4}$ cm^2/Vs **(7)**, r* < 500 nm[46] and 94 mm/s[47] for 20 nm wide, 100 nm thick nanopore, respectively), the flow velocity around the capture zone clearly becomes negligible at low flow rates (e.g. 2 µl/min and less, V(x)<2 mm/s). Although it contradicts with the optical results stating that the flow-limited regime starts at 0.3 µl/min, where the measurements were taken at a focal plane away from the channel edge, the effect of the flow profile in our system cannot be underestimated. However, it should be emphasized that there would also be an effective flow gradient through the nanopore at high flow rates in spite of

[46] It changes with the channel dimensions and the electrophoretic mobility of the molecule, defined by Equation 1.6.
[47] It is calculated at the pore mouth and decreases with a distance away from the pore.

relatively low flow velocity near the wall. This would eventually alter the dynamics of the translocation process and thus the effect requires to be taken into account when working with such flow velocities.

The experiments shown in this chapter were carried out at low flow rates, which provide compatibility with flow rates that is used in complimentary on-chip technologies. The hypothesis is that the chosen flow rates correspond to either diffusion-limited regime or transitional regime, where the diffusive flux is not fully imposed by the fluid flux in x- direction and DNA is partially coiled up.

6.1 Electrochemical characterization

In this section, we first studied the effect of flow in G and $I_{o,}$ and the nanopore noise at a variety of flow rates ranging from 0.02 μl/min to 5 μl/min. Secondly, it was shown that the performance of the integrated chip is compatible with current nanopore devices both in the absence and presence of flow. Lastly, the effect of flow on DNA translocation statistics was discussed based on the experimental findings.

6.1.1 Investigating the effect of hydrodynamic flow on the nanopore conductance

In Figure 6.3a and Figure 6.3b, I-V curves obtained at the absence and presence of flow are plotted with respect to the experiment sequence in order to take into account any potential change over time. The order of experiments was chosen randomly so as to discard any time effects and is shown on the graphs accordingly. Comparison between the curves was made in terms of G_{exp} and d_{exp} calculated using Equation 2.5 and Equation 2.6, respectively. Between each experiment there was a waiting time of 10 min.

A drastic change in the conductance (48%) was observed when comparing the initial and final G while the change dropped down to 6% towards the end of the experiments. The direct interpretation of this result is that the system supposedly reached an equilibrium state over time. This can be better understood from d_{exp}, which enlarged from an initial diameter of 27 nm to 39 nm at the end. One hypothesis for this change is that the nanopore was initially partially blocked

due to insufficient wetting of the nanopore surface and applying voltage across the nanopore assisted improving the wetting properties **(8)**. Instability due to the surface properties of the nanopore modified by the ion beam irradiation is perhaps another reason.

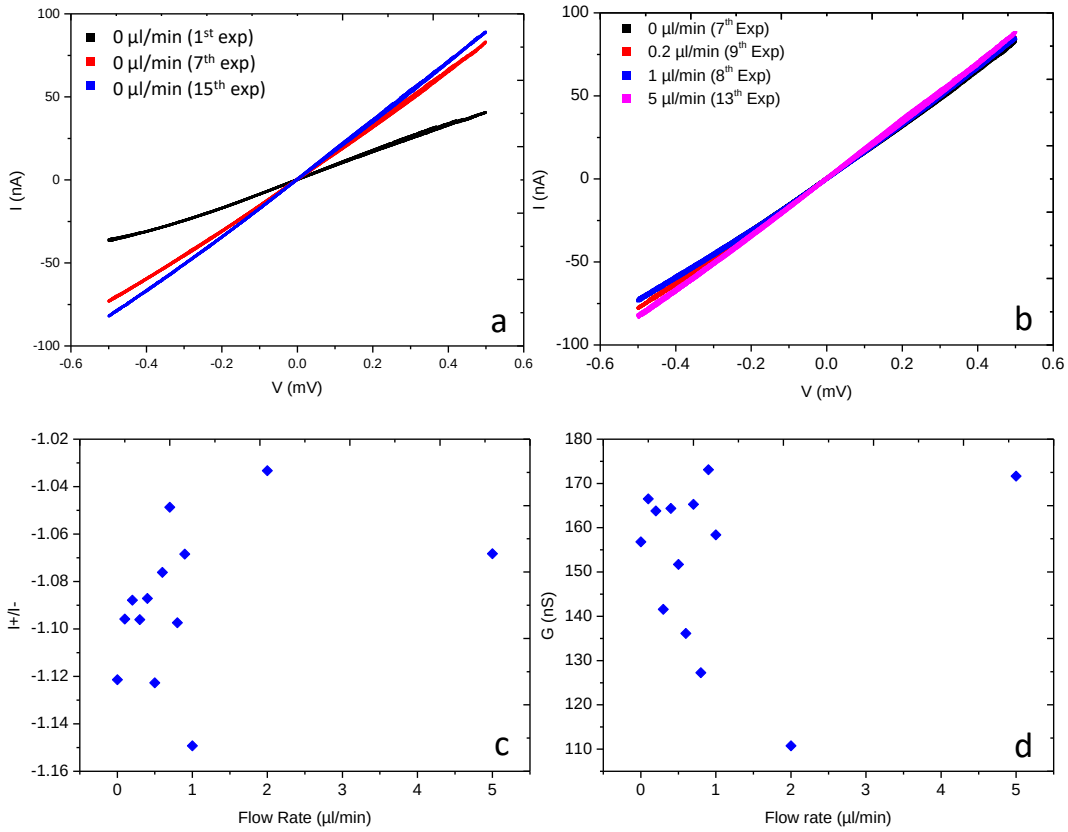

Figure 6.3 Electrochemical characterization of the integrated chip. a. I-V curves recorded at 0 flow rate at different recording times. b. I-V curve recorded at different flow rates; 0, 0.2, 1 and 5 µl/min (Experimental order; 7th, 9th, 8th, 13th, respectively). c. Current rectification extracted from each I-V curve recorded at different flow rates. d. Nanopore conductance extracted from each I-V curve recorded at different flow rates. (1 M KCl, 10 mM Tris.HCl and 1 mM EDTA).

Table 6.1 shows G_{exp} and d_{exp} with respect to the experiment sequence and the flow rate. The correspondent IV curves and a graph of G_{exp} versus flow rate are plotted in Figure 6.3b and Figure 6.3d, respectively. Figure 6.3b shows the selected IV curves recorded at different flow rates (e.g. 0, 0.2, 1 and 5 µl/min) after the stabilization of G_{exp} over time had been reached. The main striking observation is that the change in G_{exp} over time (8%) dominated the effect of flow in G_{exp}, as shown in Table 6.1. For example, in comparison of 0 flow rate (7th experiment) with

flow rate of 1 μl/min (8th experiment), G_{exp} increased; however when compared with the flow rate of 0.2 μl/min (9th experiment), further increase in G_{exp} was observed, although the flow rate was decreased. It means that the change in G_{exp} is related to the change in nanopore diameter over time. As a result, it can be concluded that the effect of flow to the ionic current is not of a significant magnitude.

Table 6.1 G_{exp} and d_{exp}, extracted from the IV curves illustrated in Figure 6.3b.

Experiment sequence	Flow Rate (μl/min)	Conductance (nS)	Nanopore diameter (nm)
7th	0	157	37.8
9th	0.2	164	38.6
8th	1	158	37.9
13th	5	171	39.5

The next step was to ascertain if there is any ionic current-rectification, which is, in general, a consequence of asymmetric ion transport due to surface charge discontinuities or asymmetric pore geometries **(9)**. In our experiments, this might be observable due to the flow stream on one side of the nanopore. To reveal the effect, the rectification ratio (ratio of the current with different polarities, $I_{+/-}$) was investigated. The results are shown in Figure 6.3c. It was observed that $I_{+/-}$ was equal to 1.12 in the absence of flow while $I_{+/-}$ at different flow rates varied between 1.02 and 1.16. This indicates that $I_{+/-}$ does not show any substantial trend, and can be interpreted that the flow through the nanopore is also negligible at the chosen flow rates.

6.1.2 Investigating the effect of hydrodynamic flow on the nanopore noise

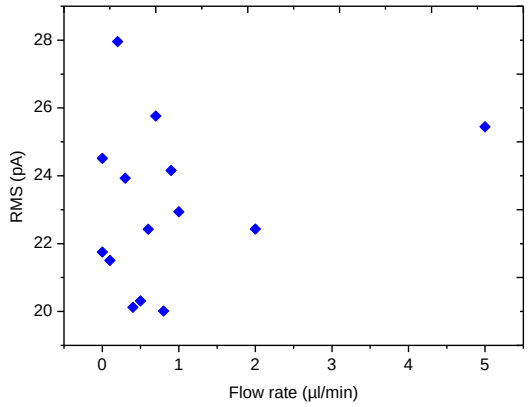

Figure 6.4 RMS noise plotted against different flow rates. (1 M KCl, 10 mM Tris.HCl and 1 mM EDTA).

The examination of RMS noise with respect to the flow rate aimed to understand the effect of flow to nanopore noise. Figure 6.4 presents the relationship between RMS noise and the flow rate, where the variation in RMS noise indicates a change in the order of less than 10 pA. The qualitative analysis of PSD resulted in the absence of any considerable difference in either high-frequency regime or low-frequency regime. This indicates that the nanopore noise is not affected by the chosen flow rates. The results agree with the electrochemical measurements, where it was concluded that there is no substantial trend with increased flow rate (between 0.02 µl/min to 5 µl/min).

6.2 Electrochemical detection of DNA translocation

In this section, the experimental results for the translocation of λ-DNA in the absence and the presence of continuous flow are discussed.

6.2.1 Translocation of λ-DNA in the absence of flow

In general, a stable open pore current was first established at different voltages before the addition of DNA. In the second step, DNA (1 or 10 µl of 500 ng/µl λ-DNA, corresponding to 15.5 nM or 155 nM, respectively) diluted in 1 M KCl, 10 mM Tris.HCl and 1 mM EDTA buffer,

was pumped into the microfluidic channel and each measurement was taken after at least 2 min of pumping in order to reach an equilibrium state between different flow rates.

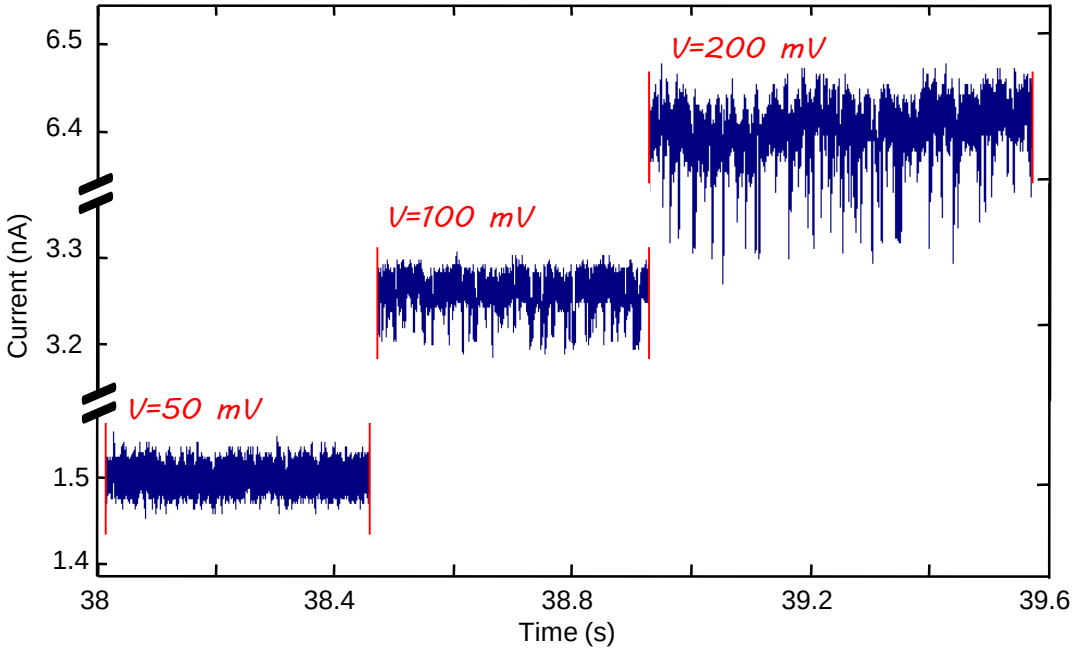

Figure 6.5 Examples of current-time traces at different voltages. Bottom left, middle and top right; 50 mV, 100 mV, 200 mV, respectively. (d_{exp} = 12-21 nm, L_{SiN} = 100 nm SiN. 15. 5 pM DNA in 1 M KCl, 10 mM Tris.HCl and 1 mM EDTA).

The most compelling evidence for a translocation event/current blockade in a current-time trace is that translocation type signals appear at high voltages and the amplitude of the current blockade enhances with the increase in voltage applied, as explained above using Equation 1.15. To confirm the compatibility of the device with commonly used nanopore devices, voltage dependency of the current blockades was examined. Figure 6.5 shows examples of current traces recorded at 50 mV, 100 mV, and 200 mV (bottom left, middle and top right, respectively, d_{pore} = 12-21 nm). At low voltages (i.e. 50 mV) there was no current blockade observed. When the voltage was increased to a higher level (i.e. 100 mV and above) there was a clear indication that the translocation type current blockades with an increase in SNR appeared, in a good agreement with the theory stated above. It was, therefore, assumed that these were the consequences of the DNA translocation. Further analysis was carried out to enable a quantitative interpretation of the data, where ΔI and t_d distributions were extracted from the current traces.

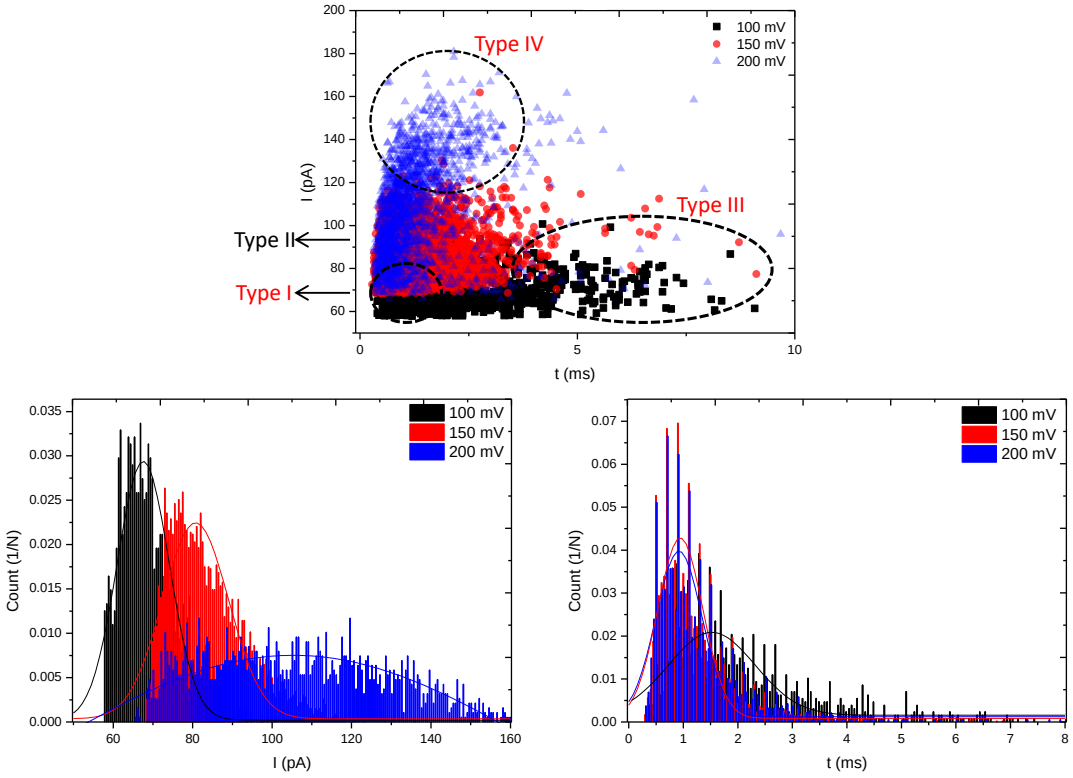

Figure 6.6 Top: Scatter plot of current blockades versus dwell time, Bottom left: Blockade current and Bottom right: Dwell time histograms at different voltages applied: blue; 100 mV, red; 150 mV and black; 200 mV.

ΔI and t_d distributions are illustrated in Figure 6.6 while Table 6.2 shows a summary of quantification of the events. The results shows that ΔI increased from 67.5±15.4 pA to 105.3±146.9 pA with increasing voltage (100 mV and 200 mV respectively) and t_d shortened with increasing voltage; 1.5±1.8 ms at 100 mV, 940±970 µs at 150 mV and 920±990 µs at 200 mV, corresponding to a velocity of 11 nucleotide/µs, 17 nucleotide/µs and 18 nucleotide/µs, respectively.

These findings are comparable to previous results reported involving large solid-state nanopores (larger than 10 nm). For example, Storm *et al* reported that λ-DNA translocates through a 10 nm SiO_2 nanopore within 1-2 ms at 120 mV **(10)**. Translocation velocity of 11 nucleotide/µs at 150 mV also agrees well with the findings of Chen *et al*, in which they stated a velocity of 27 nucleotide/µs for 10 kbp dsDNA through a 15 nm SiN pore coated with Al_2O_3

(11). The voltage dependency of the translocation velocity and time follows a linear relationship in small solid-state nanopores (e.g smaller than 5 nm) in marked contrast with a nonlinear dependence recorded with larger nanopores (e.g 10 and above) **(11-13)**. Although the DNA length differs from experiment to experiment, the results are still comparable when taking into account that Chen *et al* reported the same linear voltage relation for different DNA lengths (e.g 48.5 kbp, 10 kbp and 3 kbp) **(11)**. The nonlinear dependence of the translocation time on the voltage applied is explained to be a consequence of the increased DNA/pore interactions in small pores **(12)**.

Table 6.2 Summary of λ-DNA translocation events shown in Figure 6.6.

V (mV)	t_d(ms)	ΔI (pA)
100	1.52±1.87	67.56±15.42
150	0.94±0.97	80.75±19.57
200	0.92±0.99	105.32±146.94

Another remarkable observation is the variation in the current-time distributions for each population as seen in Figure 6.6. These variations can be associated with the unfolding and multi-level folding of the molecule while translocating through the nanopore as observed by many in the field **(10-12, 14-17)**. Since DNA is not like a stiff rod, it would rather re-orientate itself to pass through the nanopore within the limitations of persistence length and nanopore geometry (It should be kept in mind that many other physiological factors also play a crucial role). For smaller pores less than 2.5-4 nm, the ratio of molecule's folding drops significantly **(12, 17)** with strong effect on translocation statistics including the capture probability, because of the cross-section of DNA (2.2 nm for dsDNA) and thus higher energy barrier. On the other hand, DNA tends to fold back onto itself while transversing a nanopore as large as 8 nm and above. This produces current blockages larger in amplitude and shorter in the time scale. The degree of folding might differ depending on many factors including the voltage applied, nanopore geometry and surface charge

distribution. A final remark on the translocation statistics is the wide broadening of the distributions. Lu *et al* propose that the variations originate from the unravelling kinetics of the molecule outside the pore on account of having different conformational geometries during the translocation process which they name as '*conformation-induced velocity fluctuations*' **(16)**. Namely, the presumption is that the centre-of-mass for the unravelled part of the molecule would change as the molecule is pulled through the pore and results in the spread within the translocation statistics.

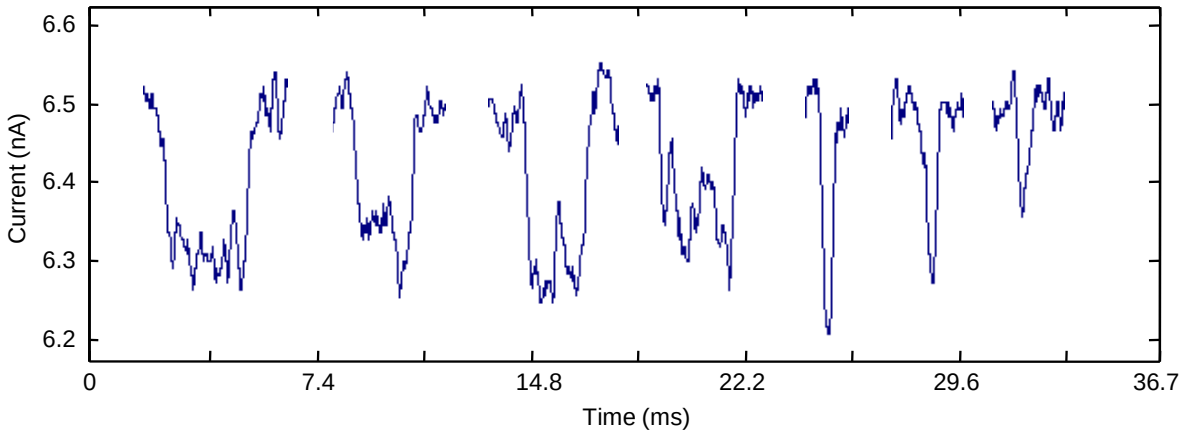

Figure 6.7 Representative individual translocation events at 200 mV.

In the result stated above, several types of current blockades were identified (some of the individual events are illustrated in Figure 6.7). The observed translocation events can be summarized as 4 types, as highlighted on the scatter plot of current–time distribution in Figure 6.6;

- ***Type I: Short and shallow events:*** Wanunu *et al* suggest that these correspond to random collisions of molecule with the pore mouth **(12)**.
- ***Type II: Deep blockage events:*** These are considered to be head-to-tail single translocation events.
- ***Type III: Long blockage events:*** These can either be interpreted as molecule being stuck inside the nanopore temporarily, as reported by Fologea *et al* **(18)** or simple translocation events as in type II **(10, 17)**. Van den Hout *et al* argues that these type of events can arise

from a molecule that blocks the nanopore entry partially but does not transverse to the trans side **(17)**. However, the authors conclude that it would not be possible due to more reasonable statistical evidences that imply them to be simple unfolded translocation events.

- ***Type IV: High current blockage events:*** Although their time distribution almost falls into the similar time scale as type II events, partial or complete folding of the molecule from its centre can be assigned to these events **(10, 14, 18)**. It is also worthwhile to mention that λ-DNA can bind to form circular DNA from its single strand 'sticky ends', and if that is the case, Storm *et al* states that the translocation signal would be identical to type IV events.

Different scenarios can further be written in order to explain the origins of the blockage signals, depending on the pore dimensions, DNA length and electrostatic interactions. An excellent overview of the subject can be found in reference **(19)**.

6.2.2 Translocation of λ-DNA in the presence of flow

As a proof-of-concept, the translocation of DNA in flow was studied using a nanopore with a diameter of 12-21 nm on a 100 nm thick SiN membrane. Figure 6.8 presents 1.5 seconds current–time trace recorded at a flow rate of 2 µl/min, while Figure 6.9 shows the relationship between the flow rate and the translocation statistics (translocation frequency, t_d and ΔI).

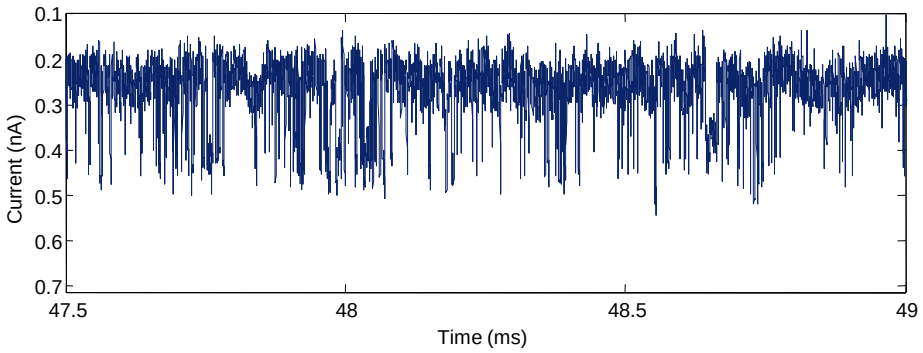

Figure 6.8 Example of 1.5 seconds current-time traces recorded at 250 mV at a flow rate of 2 µl/min. (d_{exp} = 12-21 nm, L_{SiN} = 100 nm. 15. 5 pM DNA in 1 M KCl, 10 mM Tris.HCl and 1 mM EDTA).

Translocation frequency, *f*, was extracted as a means of understanding the capture rate in flow. The initial findings yielded two different trends; increase in *f* from 1 event per second to almost 12 events per second and sharp decrease in *f* between 0.2 µl/min-1 µl/min, as shown in Figure 6.9a. The increase is probably a consequence of the altered motion of the molecule due to the increased pressure gradient through the nanopore created by the fluid flux. The latter case happened at the flow rates of 1 µl/min, 0.2 µl/min and 0.5 µl/min, which were recorded subsequently after the measurements taken in the absence of flow. It was considered that the translocation frequency dropped suddenly for a certain amount of time during these recordings, and could be neglected. The reason for the sudden change might arise from an unpredictable change in pore surface properties (e.g. nanobubble formation on the nanopore entrance) or another reason which is not clear to us yet. In another experimental study using 5 kbp dsDNA, it was also found that the translocation frequency increased when the flow rate was gradually increased to 15 µl/min and decreased to marginal values at higher flow rates[48].

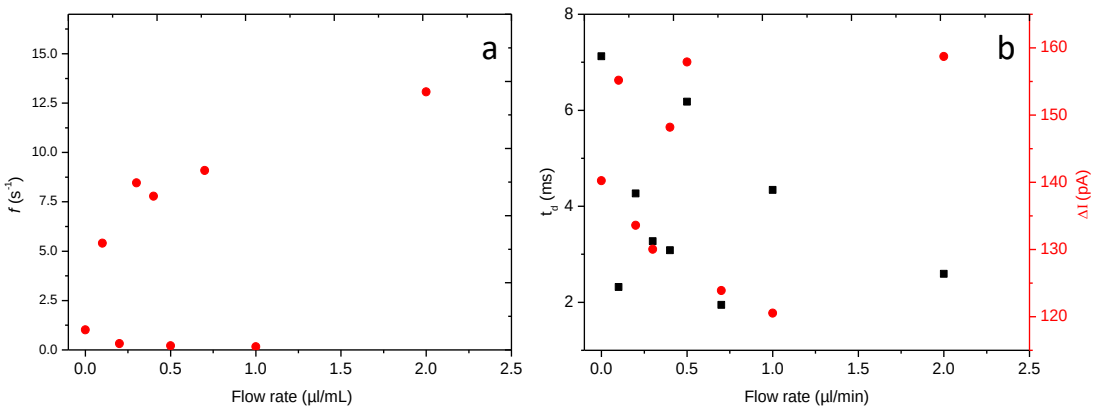

Figure 6.9 a. Flow rate versus translocation frequency. b. Flow rate versus translocation statistics (i.e. t_d and ΔI). (d_{exp} = 12-21 nm, L_{SiN} = 100 nm. 15.5 pM DNA in 1 M KCl, 10 mM Tris.HCl and 1 mM EDTA).

One may ask whether the flow affects the translocation statistics. Figure 6.9b shows the statistical analysis of the translocation events. The results do not indicate a notable trend in either

[48] The related graph can be found in the Appendix.

t_d or ΔI. However, when considering the change in t_d with respect to the experimental order, t_d reduced to almost 3 ms from an initial value of 7 ms over time.

Another experiment was carried out using a nanopore with a diameter of 16-27 nm drilled in thinned membranes (L_{SiN} =20 nm). Both long time scale blockade events and events with higher ΔI and shorter t_d (an an analogous of type III and type IV events, respectively) were observed. Compared to previously reported signal intensities, these events were greater in magnitude (presumably clogging of molecules at the pore mouth or impurities as reported by Lu *et al* **(16)**) and therefore neglected in data analysis. The extracted results are shown in Figure 6.10. At low flow rates, (e.g. lower than 0.3 µl/min), a random change in *f* was observed whereas it became slightly more controllable at higher flow rates. As for t_d and ΔI, t_d showed a decrease at slow flow rates and a relative increase at higher flow rates than 0.3 µl/min. It is nonetheless difficult to confirm that there was an obvious trend in either *f* or t_d and ΔI.

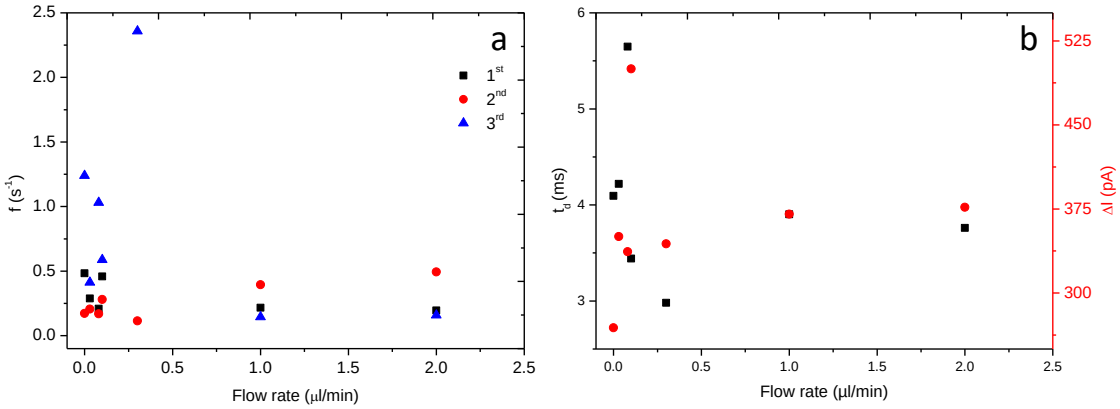

Figure 6.10 a. Flow rate versus translocation frequency (Different colours represent the repeats). b. Flow rate versus translocation statistics (i.e. t_d and ΔI). (d_{exp} = 16-27 nm, L_{SiN} = 20-25 nm. 155 pM DNA in 1 M KCl, 10 mM Tris.HCl and 1 mM EDTA.)

One possible explanation for the pore-to-pore variation might be the inconsistency in nanopore surface properties. Thick membranes were milled within 5-6 seconds whereas relatively shorter duration of the dwell time was used for the thinned membranes.

A potential consequence of this difference would be the change in charge distribution due to the difference in the rate of ion implantation into the nanopores. As far as the thinned membranes are concerned, the surface roughness is slightly different compared to the initial smoothness of SiN surface even though the homogenous etching of the membrane surface was reported previously, in CHAPTER 3. It is therefore reasonable to assume that DNA interaction with the nanopore surface and its surroundings would be different compared to that of an unprocessed membrane surface, leading to unpredictable behaviour of DNA entry to the pore.

Although each individual experimental finding can be interpreted from different angles, it is difficult to draw any conclusion at present, and therefore to determine the aforementioned capture regimes. However, the most prevailing outcome of the results would be that the DNA capture is still stochastic at the chosen flow rates on account of the random changes in the translocation statistics. To a first approximation, this leads us to presume that the flow-limited regime starts at flow rates above 10-15 μl/min for a SiN nanopore devices.

6.3 Conclusion

This chapter highlighted the concept of in-flow detection of DNA translocation through nanopores. Different capture regimes are first described as opposed to the classic nanopore capture theory; diffusion-limited regime, transitional regime, and flow-limited regime. Secondly electrochemical characterization of the integrated chip at different flow rates is shown, where the effect of flow to the nanopore conductance and noise was found to be of no substantial influence at the chosen flow rates. Third, DNA translocation is presented and the nature of different type of translocation signals is elaborated. As a proof-of-concept, the electrochemical detection of single DNA molecules under continuous flow is also presented at different flow rates. The fact that the flow effect on the DNA capture rate and translocation statistics could not be established refers the hypothesis that the translocation is still stochastic and hence diffusion-limited at the chosen flow rates.

In conclusion, one of the key figures of the work stated in this chapter is the introduction of in-flow electrochemical detection of single DNA molecules. Although it is still at a preliminary stage, the findings set the basics for the future microfluidic integrated nanopore applications (e.g. on-nanopore chip CE or on-nanopore chip PCR) and are therefore of great importance to the field. The flow rates chosen here are compatible with chip-based pre-analytical and biological processing techniques, where the flow rate is kept at a reasonable level. Awareness of the challenges and the working conditions of nanopores in flow would therefore provide a significant ease to the development of more sophisticated on-nanopore integrated devices.

References

1. Muthukumar M. Translocation of a Confined Polymer through a Hole. Physical Review Letters. 2001;86(14):3188-91.

2. Wanunu M, Morrison W, Rabin Y, Grosberg AY, Meller A. Electrostatic Focusing of Unlabelled DNA into Nanoscale Pores Using a Salt Gradient. Nat Nano. 2010;5(2):160-5.

3. Gösch M, Blom H, Holm J, Heino T, Rigler R. Hydrodynamic Flow Profiling in Microchannel Structures by Single Molecule Fluorescence Correlation Spectroscopy. Analytical Chemistry. 2000;72(14):3260-5.

4. Stone H. Introduction to Fluid Dynamics for Microfluidic Flows. In: Lee H, Westervelt R, Ham D, editors. Cmos Biotechnology. Series on Integrated Circuits and Systems: Springer US; 2007. p. 5-30.

5. Bruus H. Basic Flow Solutions. Theoritical Microfluidics. Oxford: Oxford University Press; 2008.

6. Mohiuddin Mala G, Li D. Flow Characteristics of Water in Microtubes. International Journal of Heat and Fluid Flow. 1999;20(2):142-8.

7. Stellwagen NC, Gelfi C, Righetti PG. The Free Solution Mobility of DNA. Biopolymers. 1997;42(6):687-703.

8. Beamish E, Kwok H, Tabard-Cossa V, Godin M. Precise Control of the Size and Noise of Solid-State Nanopores Using High Electric Fields. Nanotechnology. 2012;23(Copyright (C) 2013 U.S. National Library of Medicine.):405301.

9. Schoch RB, Han J, Renaud P. Transport Phenomena in Nanofluidics. Reviews of Modern Physics. 2008;80(3):839.

10. Storm AJ, Chen JH, Zandbergen HW, Dekker C. Translocation of Double-Strand DNA through a Silicon Oxide Nanopore. Phys Rev E. 2005;71(5).

11. Chen P, Gu J, Brandin E, Kim Y, Wang Q, Branton D. Probing Single DNA Molecule Transport Using Fabricated Nanopores. Nano Letters. 2004;4(11):2293-8.

12. Wanunu M, Sutin J, McNally B, Chow A, Meller A. DNA Translocation Governed by Interactions with Solid-State Nanopores. Biophysical Journal. 2008;95(10):4716-25.

13. Li JL, Talaga DS. The Distribution of DNA Translocation Times in Solid-State Nanopores. J Phys-Condes Matter. 2010;22(45).

14. Li J, Gershow M, Stein D, Brandin E, Golovchenko JA. DNA Molecules and Configurations in a Solid-State Nanopore Microscope. Nat Mater. 2003;2(9):611-5.

15. Storm AJ, Storm C, Chen J, Zandbergen H, Joanny J-F, Dekker C. Fast DNA Translocation through a Solid-State Nanopore. Nano Letters. 2005;5(7):1193-7.

16. Lu B, Albertorio F, Hoogerheide David P, Golovchenko Jene A. Origins and Consequences of Velocity Fluctuations During DNA Passage through a Nanopore. Biophysical Journal. 2011;101(1):70-9.

17. van den Hout M, Krudde V, Janssen XJA, Dekker NH. Distinguishable Populations Report on the Interactions of Single DNA Molecules with Solid-State Nanopores. Biophysical Journal. 2010;99(11):3840-8.

18. Fologea D, Gershow M, Ledden B, McNabb DS, Golovchenko JA, Li J. Detecting Single Stranded DNA with a Solid State Nanopore. Nano Letters. 2005;5(10):1905-9.

19. Muthukumar M. Polymer Translocation: CRC Press; 2011.

CHAPTER 7
Conclusion and Future Directions

This chapter illustrates the concluding remarks obtained from the experimental findings and ends with potential line of research that can be carried out to improve the experiments in the future.

"Say: Though the sea became ink for the Words of my Lord, verily the sea would be used up before the words of my Lord were exhausted, even though We brought the like thereof to help." Quran (18:108)

7.1 Conclusion

The work presented in this thesis aims to set out a roadmap for the development of a compact nanopore sensing device integrated into a microfluidic chip. The key importance of the research carried out is the illustration of the requirements and prerequisites for constructing such a device and its future applications. Most remarkably, the capability of in-flow single molecule detection based on electrochemical identification is shown, which can be a label-free alternative to optical based in-flow single molecule experiments.

Initial works were set out to investigate alternative ways to fabricate nanopores with minimal fabrication steps. For this purpose, a commercially available ultra thin polymer membrane was examined. The membrane is an approximately 150 nm thick free-standing PI membrane that does not require any pre-fabrication steps such as those of traditional solid-state nanopore devices fabricated using semiconductor technologies, and thus could be used for nanopore fabrication directly. Nanopores of several tens of nanometers in diameter could be fabricated successfully using a focused ion beam within a dual beam system that combines SEM and FIB. Although nanopore fabrication and sensing for the translocation of λ-DNA was achieved, the use of the polymer membrane device was found to be challenging for the construction of a monolithic nanopore-microfluidic device. Another discouraging finding was that the multiple uses of PI membranes resulted in the deterioration of the signal quality (e.g. current fluctuations) and therefore the membranes are for single use. If further studies are to be conducted to improve its storage and post-cleaning steps, the life-time of the device can be increased and the membrane can potentially be utilized in a dualithic integrated system.

Although it is considerably more demanding and time-consuming, fabrication of SiN membranes is well established in literature, which involves photolithography and RIE followed by KOH etch. The process results in the production of more than 50 individual chips out of a single wafer and was considered to be more cost-effective. Therefore, the integration experiments were carried out using SiN chips. Additional works were carried out to improve its performance by thinning the membranes locally based on several steps of photolithography and RIE since

signal quality highly depends on the nanopore dimensions; the thinner the membrane is the higher the SNR. The optimization steps led to the conclusion that RIE requires several pre-cleaning steps and pre-test experiments prior to each individual experiment. Moreover, pre-cleaning steps provide the improved etch quality while the test experiments enhances the predictability on the etch rate.

Integration is straight-forward and reproducible, after which both devices are fabricated using traditional fabrication techniques. As the integrated device provides a planar interface between SiN and PDMS chip, one can design any sort of channel networks and integrate it onto SiN chip by literally changing SiN chip dimensions to provide complete sealing for a monolithic device.

Optical experiments provided an understanding of the experimental velocity components such as diffusion and flow velocity. Further to this, diffusion- and flow-limited regimes were identified; the flow-limited regime starts at a flow rate of 0.3 μl/min and the transitional regime falls into 0.02-0.3 μl/min flow rates. To the best of our knowledge, this is the first experiment that has been carried out to examine the ranges of such regimes using FCS although there are a few examples for the detection of DNA and different fragments in flow **(1)**. It is therefore believed to provide valuable insights into the subject. Consideration of DNA elongation in flow is also crucial as nanopore sensing in fact entails the linearization of the molecule while translocating.

Last, the concept of nanopore sensing in-flow was investigated. Brief discussion on the velocity components of diffusion, electrophoretic motion and hydrodynamic flux of DNA drew a tentative hypothesis that the classic theory for the definition of nanopore capture zones should be extended to include flow velocity in three dimensions and the rheological properties of DNA (diffusion-limited regime, transitional regime and flow-limited regime). Unfortunately, the results obtained from the optical experiments could not be applied directly to the aforementioned capture zones. It is because of the fact that it is a planar device and the velocity gradient was realized to be different at the nanopore mouth-microfluidic channel edge; flow velocity is relatively slower at the edges of the microfluidic channel than the centre where the focal plane might be positioned

in optical experiments. Although the dependency of nanopore capture on flow rate is inconclusive experimentally, the results hypothetically indicate that the chosen flow rates fall into a diffusion-limited regime due to the evidences that the detection is still stochastic. On a different note, electrochemical characterization of the integrated chip in flow resulted in no considerable effect to the nanopore conductance and noise at the chosen flow rates.

7.2 Future directions

There are several future directions in which the research can potentially be extended and improved further.

One such direction to the subject discussed in CHAPTER 3 would be the introduction of an additional layer of semiconducting or insulating material in-between Si support and SiN with certain etching selectivity and the subsequent local removal of SiN. Addition of very thin SiO_2 layer is a nice example; SiN is completely removed from the top locally and a small section of an ultra-thin free-standing SiO_2 window is created. This can be achieved by the addition of O_2/N_2 discharge to CF_4 gas flow yielding high selectivity towards Si_3N_4 over Si and SiO_2 **(2)**.

Secondly, building upon the idea of integration, the development of an on-nanopore CE chip or on-nanopore PCR chip would be a potential direction to pursue. However, integration can only bring success provided that working principles of both nanopore and CE sensing or PCR amplification are made compatible with each other (e.g. voltage range used). One of the challenges for such integration is the fact that large SiN chips tend to break easily and require handling with care. Others include increased cost due to reduced number of chips that can be produced from a single wafer and the nanopore noise that might arise from the additional necessary electrical or thermal components of the complimentary platform. Another possibility would be the microfluidic integration of nanopore devices into MEMS devices such as nanopore integrated metal-oxide-semiconductor (CMOS) potenstiostat chip, as shown recently in a preliminary work by several groups **(3, 4)**. However, the requirement for high sensitivity and minimal noise contribution to signal might create several challenges when additional electrical contacts are made to the system. Nonetheless, noise can either be avoided at the very beginning

of the analysis by shielding, using noise rejecting components (e.g. filters, amplifiers), digital filters, and so on or by several post-signal processing techniques.

A third alternative approach to further microfluidic integration of nanopores would be to utilize glass-capillaries, as recently presented by Gong *et al* **(5)**. The advantage of glass-capillaries over SiN devices has been realized to be numerous on account of their relatively cheaper and easier production. They also provide robust tip opening which is not subject to changes over time. Therefore, glass-capillary integrated microfluidic systems might lead to faster production and increase the reproducibility. Recalling the pore-to-pore variations in flow experiments due to instability of FIB-drilled nanopores and day-to-day differences in nanopore fabrication, the effect of flow rate on nanopore capture and thus the determination of the related regimes might better be investigated using glass-capillaries. Moreover, the optical results presented in this work would be applied to in-flow experiments using glass-capillary integrated chip more realistically, providing that the capillary is aligned at the centre of the channel.

With regards to the flow experiments, it would be of interest to investigate the flow effects on capture using TEM drilled pores if one is to use SiN nanopores, because it is well-known fact that signal quality of TEM nanopores is better, and the life-time of the device is longer. However it would be more reasonable to extend the investigation further based on more rigorous theoretical studies and simulations. Predictions would then provide an exclusive insight into the subject and therefore the complexity of the system could be simplified.

In-flow translocation experiments can potentially be applied to droplet-based flow systems, where single molecules are encapsulated inside single droplets in the microfluidic channel and detected by nanopores. Another interesting research direction would be the application of hydrodynamic flow focusing inside the microfluidic channel where the intensified flow motion is positioned at the top of a nanopore, so that the benefit of mixing and electrochemical analysis at single molecule level would be coupled. With the same idea in mind, electrokinetic traps can be utilized for single molecule detection based on nanopore sensing. As a final thought, nanopore arrays can be coupled into microfluidic channels in conjunction with optical techniques for high throughput, where multiple events occurring in flow are monitored at single molecule level.

7.3 Summary

The advantages of marrying nanopores and microfluidic chips are numerous and the concept of in-flow electrochemical detection of single molecules is significantly important in the field of single molecule biosensing. The concluding remark is therefore that the future of nanopore-integrated chips is promising, although it is still an emergent research field at an early stage of development.

References

1. Van Orden A, Cai H, Goodwin PM, Keller RA. Efficient Detection of Single DNA Fragments in Flowing Sample Streams by Two-Photon Fluorescence Excitation. Analytical Chemistry. 1999;71(11):2108-16.

2. Kastenmeier BEE, Matsuo PJ, Oehrlein GS. Highly Selective Etching of Silicon Nitride over Silicon and Silicon Dioxide. Journal of Vacuum Science & Technology a-Vacuum Surfaces and Films. 1999;17(6):3179-84.

3. Uddin AY, S. Chen, C-H. Corigliano, E. Milaninia, K. Theogarajan, L. . Integration of Solid-State Nanopores in a 0.5 μm Cmos Foundry Process. Nanotechnology. 2013;24(15):155501.

4. Rosenstein JK, Wanunu M, Merchant CA, Drndic M, Shepard KL. Integrated Nanopore Sensing Platform with Sub-Microsecond Temporal Resolution. Nat Meth. 2012;9(5):487-92.

5. Gong X, Patil AV, Ivanov AP, Kong Q, Gibb T, Dogan F, et al. Label-Free in-Flow Detection of Single DNA Molecules Using Glass Nanopipettes. Analytical Chemistry. 2013;86(1):835-41.

Appendix

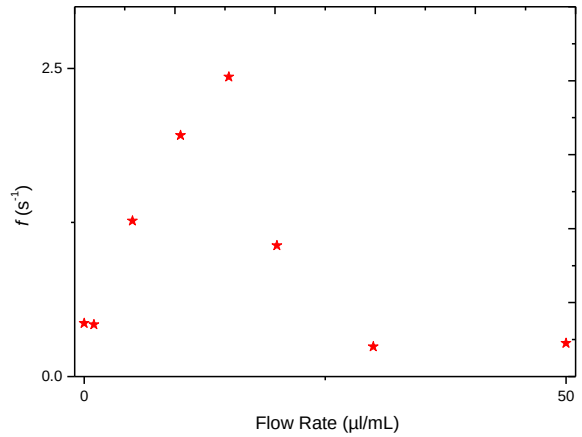

Figure A Translocation of 5 kbp dsDNA. Translocation frequency is plotted against the flow rates.